USING TWO-DIMENSIONAL IMPEDANCE MAPS TO STUDY ACOUSTIC PROPERTIES OF TISSUE MICROSTRUCTURE

BY

ADAM C. LUCHIES

DISSERTATION

Submitted in partial fulfillment of the requirements
for the degree of Doctor of Philosophy in Electrical and Computer Engineering
in the Graduate College of the
University of Illinois at Urbana-Champaign, 2016

Urbana, Illinois

Doctoral Committee:

Associate Professor Michael L. Oelze, Chair
Professor William D. O'Brien, Jr.
Professor Michael F. Insana
Professor Minh N. Do

ABSTRACT

Quantitative ultrasound (QUS) imaging represents a set of techniques for estimating acoustic properties of tissue microstructure that have confirmed potential for identifying disease and monitoring therapy. In one approach to QUS, the backscatter coefficient (BSC) from a tissue is utilized to quantify and classify tissue state. The BSC is a fundamental property of a tissue based on the frequency power spectrum estimated from the RF signals corresponding to ultrasonic backscatter. From the BSC, parametric models can be constructed to relate the frequency-dependent BSC to geometrical properties of the underlying tissue. However, most of these parametric models are based on analytic expressions (e.g., Gaussian function) and not on actual tissue morphology.

The three-dimensional impedance map (3DZM) is a computational tool to create tissue specific form factor models directly from tissue histology. 3DZMs are constructed from a series of adjacent histological tissue slides that have been stained to emphasize acoustic impedance structures. The power spectrum of a 3DZM can be related to the BSC. Therefore, ZMs can be used to create tissue specific form factors. However, the process of constructing a 3DZM is expensive in terms of slide preparation time, computational time, and financial cost. In addition, there are multiple opportunities for large distortions to be introduced when constructing 3DZMs. A method based on analyzing two-dimensional impedance maps (2DZMs) would avoid many of the shortcomings of the 3DZM method. The proposed 2DZM method exploits the properties of isotropic media to estimate the correlation coefficient from slices before estimating the 3D volume power spectrum.

Simulations were used to verify that 2DZMs could be used to estimate correlation coefficients and 3D power spectra having low error. The studied media had known correlation coefficients and power spectra so it was possible to verify that estimation of the correlation coefficient and power spectrum

was possible. First, collections of sparse scatterers (e.g., spheres and ellipsoids) were studied. These studies indicated that correlation coefficients with RMSE less than 1% resulted when the 2DZMs contained 15 object cross sections. Second, media having a spherical Gaussian correlation coefficient and power spectrum were studied. This study indicated that correlation coefficients with RMSE less than 3% and power spectra with RMSE less than 11% resulted when using a single 2DZM having a size that was 50 times the scatterer size. Third, collections of dense spheres were studied. This study indicated that correlation coefficients with RMSE 1.5% resulted when using a single 2DZM having a size that was 25 times the scatterer size. Power spectra with RMSE 25% resulted when using 20 2DZMs having size that was 25 times the scatterer size.

ZMs created from healthy rabbit livers were studied. An analysis of bias was carried out to determine the smallest size 2DZM that could be used without biasing the correlation coefficient and power spectral estimates. The results of this study indicated that correlation coefficients with RMSE 0.9% and power spectra with RMSE 1.4% resulted when using 2DZMs with side length 150 μm. An analysis of variance was carried out to determine the number of 2DZMs that needed to be used to reduce variance in the correlation coefficient and power spectral estimates. The results of this study indicated that correlation coefficients with RMSE 0.9% and power spectra with RMSE 1.4% resulted when estimating the correlation coefficient using 10 2DZMs.

The 2DZM approach was tested on simulated media having known correlation coefficients and power spectra. The simulation results demonstrated that the 2DZM method was able to capture information about the size, shape, and 3D spatial locations of the scatterers. The rabbit liver results demonstrated the 2DZM method working with actual histology. These findings demonstrate that 2DZMs can be used to model ultrasonic scattering.

ACKNOWLEDGMENTS

Numerous people deserve acknowledgement for helping me to complete this dissertation. I want to recognize my advisor Professor Michael L. Oelze for teaching me how to do research and for providing interesting problems to work on, Professor William D. O'Brien, Jr. for asking difficult and challenging questions about the projects that I have worked on during graduate school, and my entire doctoral committee for their insights and feedback about my dissertation topic.

Thanks to all members of the Bioacoustics Research Laboratory who were active during my time at the University of Illinois for being helpful and supportive. In particular, Sue Clay and Julie Ten Have helped with logistical issues related to doing research, and fellow students Jeremy Kemmerer, Trong Nguyen, and Scott Leithem shared many research and non-research related conversations with me. I recognize Jonathan Mamou for offering me the opportunity to complete an internship related to my dissertation topic at Riverside Research and for providing several useful insights for this project. I acknowledge Alex Pawlicki for providing the rabbit liver 3DZMs used in this thesis.

All of the instructors I have taken courses from at the University of Illinois deserve acknowledgment.

I acknowledge the many roommates that I had during my time in graduate school. Centennial House was a great place to live for six years; I am grateful for the positive impact that that community had on my life, and I hope that it will continue to exist into the future. I appreciate the support and encouragement provided by the InterVarsity Graduate Christian Fellowship. Finally, I must thank my family for their loving support and care throughout my entire life.

TABLE OF CONTENTS

CHAPTER 1

INTRODUCTION

1.1 Ultrasound imaging

Ultrasound imaging has achieved widespread use for internal imaging of the human body over the past several decades. The following characteristics of the ultrasound imaging modality have contributed to its success: ultrasound images can be formed in real-time, ultrasound machines are inexpensive and can be made to be portable, and ultrasound uses non-ionizing radiation. Future technological development of ultrasound image processing techniques will continue to expand its use in diagnostic and therapy monitoring applications.

The most common ultrasound imaging mode is the B-mode image, which is formed from a collection of adjacent envelope detected radio frequency (RF) voltage traces, called A-lines. Ultrasound signals are created when an ultrasound system causes a pressure wave to propagate through a medium. Inhomogeneities in the medium cause the ultrasonic energy to scatter in different directions, including back to the ultrasound transducer where it is detected and used to create A-lines. The contrast mechanism in these images is the change in acoustic properties (compressibility and density) encountered by the propagating ultrasonic waves. In soft tissues of the human body, these changes in acoustic properties often occur at the interfaces between different organs and small inhomogeneities inside organs.

B-mode images are useful in some applications for characterizing disease [1]. B-mode images are highly dependent on machine settings, so different users with different systems may produce vastly different images for the same scan target. B-mode images are mostly qualitative in nature, restricting the ability to perform quantitative analysis that is hypothesized to markedly improve disease detection. Finally, B-mode images are devoid of the frequency-

dependent information originally contained in the raw (unprocessed) RF data that is lost during envelope detection. Several quantitative ultrasound imaging methods have been developed to overcome some of these limitations and to mine the discarded ultrasound RF signal frequency content for diagnostic purposes.

1.2 Quantitative ultrasound imaging

Quantitative ultrasound (QUS) imaging is a set of techniques for estimating acoustic properties of tissue microstructure that have confirmed potential for identifying disease and monitoring therapy. For example, QUS methods based on estimating the backscatter coefficient (BSC) have been used in the eye [2], prostate [3], heart[4], kidney [5], liver [6], breast [7], cancerous lymph nodes [8], monitoring cell death [9], and evaluating disease treatment [10]. The BSC is a fundamental property of a tissue akin to the sound speed and attenuation. The BSC is based on the frequency power spectrum estimated from the RF signals corresponding to ultrasonic backscatter. From the BSC, form factor models can be constructed to relate the frequency-dependent BSC to geometrical properties of the underlying tissue. Feature extraction is performed on the form factor using parametric models and the estimated parameters used in a classification task for the case of disease diagnosis or in a regression task for the case of therapy monitoring.

The BSC modeling problem is fundamentally ill-posed because an infinite number of models could be designed to capture the frequency-dependent behavior of the BSC (e.g., splines). Therefore, the model space is usually constrained to parametric models derived from scatterer geometries such as the fluid-filled sphere [11], spherical shell [12], two concentric spheres [13], etc. Using these models, acoustic properties related to tissue microstructure such as the effective scatterer diameter (ESD) and the effective acoustic concentration (EAC) can be estimated.

When examining complex biological tissues, constraining the model space in the described manner can be a major deficiency. Failure modes include the existence of large errors between the actual and modeled BSC or histological observation that does not agree with the estimated ESD and EAC. In

addition, the BSC is usually estimated for a finite frequency range, so different parametric models may fit the BSC equally well while providing different parameter estimates. It is clear that improved methods are needed for feature extraction that agree with histological observation and that reduce error between actual and modeled BSC.

1.3 Impedance maps

A promising approach to the described problems is to correlate directly histological observation with ultrasonic measurement. In early work, Fields correlated B-mode image characteristics with histological analysis in breast tumors [14]. In later work, Waag et al. proposed estimating the volume power spectra from the two-dimensional (2D) power spectra of optically rendered planar tissue sections for the purpose of predicting ultrasound scattering from tissues. However, in that study, the analyzed optical images were not compared to acoustic scattering predicted by theory or ultrasound measurement [15]. Insana et al. used histological analysis of the kidney in order to select a correlation function for modeling ultrasound backscatter measurements [5]. Czarnota et al. observed changes in ultrasound backscatter due to cell death and correlated these changes to histological observations [9]. Mamou et al. constructed three-dimensional (3D) impedance maps (ZMs) from planar histology sections and compared BSC estimates predicted from the 3DZMs with BSC estimates from ultrasound measurements in animal models for breast cancer [16–18]. Similarly, Gyöngy et al. simulated ultrasound B-mode images for canine mastocytoma tumors based on histology and compared the results to actual ultrasound B-mode images [19].

Of the described methods, ZM analysis has the advantage of quantitatively and directly connecting optically based histology with ultrasound measurement. Using ZM analysis, the structure observed in histology can be quantitatively related to the structure observed using ultrasound [16–18, 20]. In addition, the ZM provides estimates of the correlation coefficient for the medium, a quantity that is not accessible from the BSC measured over a finite frequency range using ultrasound. Different parametric models can produce the same BSC over a finite frequency range, which is a problem that does not affect the correlation coefficient. For a particular tissue, once

the relationship between histology and ultrasound observation has been established, more complex model-based feature extraction techniques may be designed by incorporating additional information about the medium into the models (e.g., assume a distribution for scatterer sizes or a structure factor for the spatial distribution of the scatterers) [21–23].

Assuming weak scattering, the three-dimensional (3D) volume power spectrum of a 3DZM can be related to the BSC estimated from the received RF ultrasound backscatter signal [24]. Currently, 3DZMs are created from a series of adjacent histological tissue slides that have been stained to emphasize acoustic impedance structures. The slides are digitized using a camera, a realignment process is applied to the series of images, and each pixel is assigned an impedance value based on color. The impedance value images are stacked on top of each other to form a 3D computational model of acoustic impedance. In the case of an isotropic medium, the 3D power spectrum of the 3DZM can be radially averaged and related to the power spectrum of the ultrasound backscatter signal. In the case of an anisotropic medium, the ultrasound propagation direction must be known relative to the orientation of the 3DZM. The k-space line of the 3DZM power spectrum that is parallel to the ultrasound propagation direction can be extracted and related to the power spectrum of the ultrasound backscatter signal.

The process of constructing a 3DZM is expensive in terms of slide preparation time, computational time, and financial cost. The weaknesses of the 3DZM method are manifold. A large set of histological slides need to be meticulously stained, optically scanned, and digitized. After loading the optical images to a computer, adjacent slides must be registered and aligned using a computationally intensive search over a large transformation set (i.e., rotations, translations, etc.). If the actual physical transformations experienced by the slides during ZM preparation are not included in this set, it is impossible to correctly align the slides. Sometimes slides are lost during the ZM preparation process and these missing sections must be interpolated. The histology sections may take up different amounts of the applied stain, so the image colors need to be adjusted and contrast equalized. Large discontinuities can be introduced at multiple stages in the 3DZM processing pipeline and these discontinuities can lead to distortions in the estimated power spectrum. Furthermore, there is a sampling issue with the 3DZMs. A

single 3DZM typically represents a resolution cell size or smaller of a medical ultrasonic imaging system. Therefore, large numbers of 3DZMs need to be constructed to accurately represent backscattered signals representing tissue volumes, such as a tumor.

1.4 Dissertation goals and proposed research

The primary goal of ZM analysis is to discover the anatomical structures in a biological medium that are responsible for ultrasonic scattering and to model the contribution from the scattering structures. The identification of the underlying mechanisms that cause ultrasonic scattering in biological tissues will aid in the design of new scattering models for analyzing BSCs. Improved BSC modeling will improve feature extraction and ultimately the diagnostic utility of BSCs.

The weaknesses of the 3DZM method as described above motivate the development of improved ZM analysis methods. A method based on analyzing 2DZMs would avoid many of the described shortcomings of the 3DZM method. For example, registration of adjacent slides is not necessary when using 2DZMs, which reduces computational cost, avoids introducing errors to the ZM spectral estimate if the transformation introduced by slicing cannot be undone, and avoids the problem of missing slices. In addition, 2DZMs can be constructed from many slices and used for averaging results from many independent samples. The potential to overcome the shortcomings of the 3DZM motivates the development of the 2DZM method.

The goals of the proposed research were:

1. To identify and/or develop methods for conducting ZM analysis using planar sections. Normally planar sections are insufficient for characterizing volumetric structure; however, properties related to volumetric structure may be estimated using planar sections in the setting of an isotropic medium.

2. To demonstrate the 2DZM method using simulations. The simulation studies were designed to study practical issues related to ZM analysis such as planar section size, spacing, and thickness. The simula-

tions consisted of collections of discrete objects (e.g., spheres, ellipsoids, cylinders) or continuous media (spherical Gaussian impedance distribution) such that the simulated medium had a known correlation coefficient and power spectrum.

3. To demonstrate the 2DZM method using ZMs created using optical microscopy. ZM analysis was conducted using 3DZMs, repeated using 2DZMs, and the results of the two analyses were compared. ZMs created from rabbit livers were examined.

1.5 Scientific contributions

The scientific contributions in this work can be summarized as follows:

1. Existing methods for estimating volume scattering from planar scattering were reviewed.

2. A new method for estimating volume scattering from planar scattering was developed.

3. Simulations were used to demonstrate that 2DZMs can replace 3DZMs for sparse and dense collections of objects and for continuous media. The simulations were designed to address practical issues related to ZM analysis. These issues included:

   (a) Determining the effects of 3D windowing on ZM analysis. A ZM is a finite section of a random process and the effects of applying a container to this random process before computing the power spectrum were examined. Two characteristics of the 3D window were examined including size and shape.

   (b) Sections of the tissue are cut in a sequential manner and mounted on histology slides. The effects of using regularly spaced slices with spacing less than the correlation length of the medium was studied.

   (c) The sections of the tissue cut for histology are not infinitesimally thick and if this thickness is large relative to the correlation length

of the medium it can lead to distorting effects on the estimated correlation coefficients and power spectra. These effects were studied and quantified.

4. A method for estimating volume scattering from planer scattering was developed for transverse isotropic media. A transverse isotropic medium is isotropic in only two dimensions. If such a medium is sliced parallel to the plane that exhibits isotropy, then 2DZMs are a natural choice for studying volume scattering.

5. Simulations were used to demonstrate that for some anisotropic media, 2DZMs were successful at estimating correct correlation coefficients and power spectra.

6. ZMs provide access to the correlation coefficient of a tissue. The BSC estimated using ultrasound is band limited and therefore it is not possible to study the tissue correlation coefficient. However, this problem does not affect ZM analysis as the correlation coefficient and power spectrum can be studied and modeled. These two methods of ZM analysis were compared and contrasted.

7. A structure function model that includes the effects of a container was developed. Several applications exist where container effects may be important, including ZMs, estimating BSCs using ultrasound (focal region is the container), and hierarchical structure function modeling involving clustering of scatterers (e.g., red blood cell aggregates).

1.6 Organization

The remaining chapters of this dissertation are organized as follows. Chapter 2 reviews the theory of weak acoustic scattering of plane waves, modeling BSCs and correlation coefficients and structure functions, and it introduces the structure function with container effects. Chapter 3 reviews the construction and analysis of ZMs, builds intuition for 2DZM analysis, presents the equations that make 2DZM analysis possible, and discusses methods for estimating volume power spectra from 2DZMs. In Chapter 4, simulations

are used to validate the structure function with container effects, and practical issues related to using 2DZMs to estimate volume power spectra are studied. In Chapter 5, ZMs created from actual histology are used to show that 2DZMs can significantly reduce the number of slices necessary to estimate form factors. Chapter 6 summarizes the contributions of this work and outlines the results and future work.

CHAPTER 2

ACOUSTIC SCATTERING THEORY

The primary goal of ZM analysis is to use maps of acoustic properties created using optical or scanning acoustic microscopy to study the BSC, a quantity that is estimated from ultrasound backscatter and is a fundamental property of tissue microstructure [12, 25–27]. ZM analysis relies on the theory of weak acoustic scattering by plane waves. The theory of weak scattering by plane waves is now reviewed briefly and the reader is referred to the textbook by Morse and Ingard [24], the paper by Insana et al. [12], and the book chapter by Insana and Brown [28] for a more complete treatment of this subject. The material in these sources forms the foundation for the 3DZM method developed by Mamou et al. [16] and for the 2DZM method proposed in this thesis.

2.1 Weak scattering of plane waves

Consider an infinite homogeneous medium having compressibility κ_0 and density ρ_0. In this medium, inhomogeneities exist having compressibility and density values that vary from the infinite medium and are given by $\kappa(\mathbf{r}')$ and $\rho(\mathbf{r}')$, where $\mathbf{r}'$ is used to denote a point inside an inhomogeneity. Let the smallest sphere that can be drawn to contain this inhomogeneity be labeled as V and have a radius a. The inhomogeneity could be a single particle (e.g., a sphere), a collection of particles, or a region with continuously varying compressibility and density. Assume an acoustic plane wave with unit amplitude is incident on the inhomogeneity as shown in Fig. 2.1. Scattering of the incident plane wave arises due to variations in compressibility and density, and the scattered pressure due to the inhomogeneity and at a position $\mathbf{r}$ that is far from the inhomogeneity behaves like a spherical wave and is given by [24]

$$p_s(\mathbf{r}) = \frac{e^{jkR}}{R}\Phi(\mathbf{K}) \tag{2.1}$$

where $\Phi(\mathbf{K})$ is called the complex scattering amplitude, k is the wavenumber, and the magnitude of the position vector is $R = |\mathbf{r}|$. The vectors $\hat{\mathbf{i}}$ and $\hat{\mathbf{o}}$ are called the incident and observer vectors, respectively. The scattering amplitude describes the spatial frequency dependence of the scatterer and depends on the scattering vector $\mathbf{K} = \hat{\mathbf{i}} - \hat{\mathbf{o}}$. The magnitude of the scattering vector is $|\mathbf{K}| = 2k\sin(\theta/2)$ and in the case of backscatter becomes $\mathbf{K} = 2k\hat{\mathbf{i}}$.

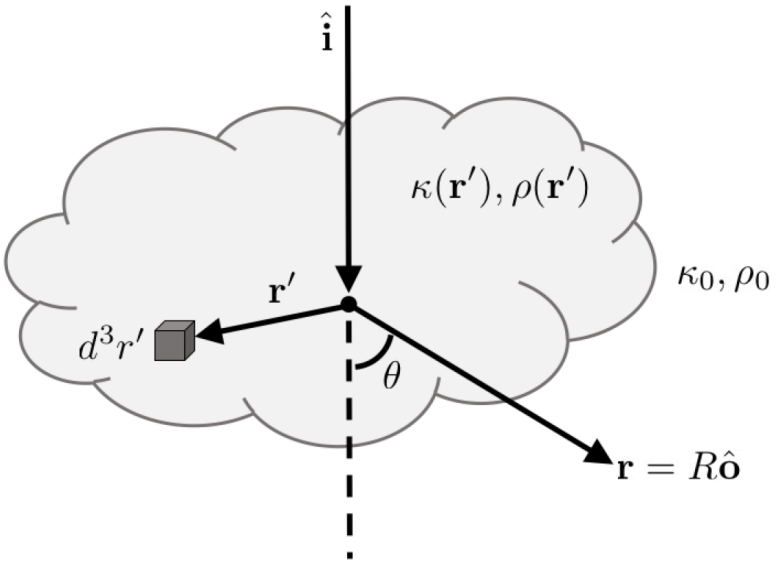

Figure 2.1: Scattering geometry for an inhomogeneity.

Define the relative compressibility and density of the inhomogeneity as

$$\gamma_\kappa(\mathbf{r}') = \frac{\kappa(\mathbf{r}') - \kappa_0}{\kappa_0} \tag{2.2}$$

and

$$\gamma_\rho(\mathbf{r}') = \frac{\rho(\mathbf{r}') - \rho_0}{\rho(\mathbf{r}')} \tag{2.3}$$

and finally

$$\gamma(\mathbf{r}') = \gamma_\kappa(\mathbf{r}') + \gamma_\rho(\mathbf{r}')\cos(\theta) \tag{2.4}$$

where θ is the angle between the incident and observer vectors as indicated

in Fig. 2.1. If the medium is weakly scattering and the size of the structures is much smaller than the wavelength, the Born approximation applies and the scattering amplitude can be approximated by [28]

$$\Phi(\mathbf{K}) \approx \frac{k^2}{4\pi} \int_V \gamma(\mathbf{r}') e^{j\mathbf{K}\cdot\mathbf{r}'} d^3 r'. \tag{2.5}$$

In addition, the assumption of small density and compressibility fluctuations allows $\gamma(\mathbf{r}')$ to be approximated as

$$\gamma(\mathbf{r}') \approx -2\frac{z(\mathbf{r}') - z_0}{z_0} \tag{2.6}$$

where $z(\mathbf{r}') = \rho(\mathbf{r}')c(\mathbf{r}') = \sqrt{\rho(\mathbf{r}')/\kappa(\mathbf{r}')}$ is the plane wave acoustic impedance. The differential scattering cross section for the inhomogeneity is

$$\sigma_{ds} = |\Phi(\mathbf{K})|^2 = \Phi(\mathbf{K})\Phi^*(\mathbf{K}). \tag{2.7}$$

The development so far is for a deterministic medium with a known compressibility and density map specified by $\gamma(\mathbf{r}')$. Practically, the goal is not to determine the BSC for a specific realization of $\gamma(\mathbf{r}')$, but to determine it for a class of biological tissue (i.e., an organ in the body such as the liver). Therefore, the single realization $\gamma(\mathbf{r}')$ must be replaced with a spatial random process $\{\gamma(\mathbf{r}')\}$ that describes an ensemble collection of possible compressibility and density maps for the examined biological tissue. In addition, when characterizing this random process using the BSC estimated using ultrasound or using ZMs, a spatially confined section of the random process $\{\gamma(\mathbf{r}')\}$ is examined. Therefore, the differential scattering cross section is replaced with the differential scattering cross section per unit volume which can be written in terms of an ensemble average for the random process $\{\gamma(\mathbf{r}')\}$ as

$$\sigma_d = \frac{1}{V}\langle \Phi(\mathbf{K})\Phi^*(\mathbf{K})\rangle \tag{2.8}$$

where $\langle\cdot\rangle$ indicates an ensemble average with respect to $\{\gamma(\mathbf{r}')\}$. The differential backscattering cross-section per unit volume, or the BSC, is

$$\sigma_b = \frac{1}{V}\langle \Phi(2k\hat{\mathbf{i}})\Phi^*(2k\hat{\mathbf{i}})\rangle. \tag{2.9}$$

Assuming that $\{\gamma(\mathbf{r}')\}$ is weakly stationary and zero mean, i.e., $\langle\{\gamma(\mathbf{r}')\}\rangle = 0$,

the BSC can be related to the 3D correlation coefficient, $b_\gamma(\mathbf{\Delta r})$, for the random process $\{\gamma(\mathbf{r}')\}$. The correlation coefficient for a random process is a statistical quantity that describes the spatial fluctuations in acoustic properties that can be estimated using ZMs. The BSC in terms of this correlation coefficient is [28]

$$\sigma_b = \frac{k^4}{16\pi^2}\left[\gamma_0^2 \int_{-\infty}^{\infty} b_\gamma(\mathbf{\Delta r}) e^{-j2k\hat{\mathbf{o}}\cdot\mathbf{\Delta r}} \mathrm{d}^3\Delta r\right] \tag{2.10}$$

where γ_0^2 are the mean-square fluctuations in tissue properties and the dependence on the incident vector $\hat{\mathbf{i}}$ is given by $\hat{\mathbf{o}} = -\hat{\mathbf{i}}$ for the case of backscatter. Equation 2.10 shows that the BSC is a frequency-dependent term multiplied by a k-space line from the 3D Fourier transform of the 3D correlation coefficient for the random process $\{\gamma(\mathbf{r}')\}$. The term inside the brackets of Eq. 2.10 is called the power spectrum of the random process $\{\gamma(\mathbf{r}')\}$ and is denoted by S. The BSC can be written in terms of this power spectrum as

$$\sigma_b = \frac{k^4}{16\pi^2} S(2k\hat{\mathbf{i}}) \tag{2.11}$$

where the dependence on the incident vector has been included to indicate that the BSC depends on the plane wave angle of incidence in an anisotropic medium. The BSC can be found for different angles of incidence by extracting the correct line from the 3D power spectrum of the random process $\{\gamma(\mathbf{r}')\}$.

If the random process $\{\gamma(\mathbf{r}')\}$ is anisotropic and the correlation coefficient varies as the spherical coordinate angles vary, Eq. 2.10 serves as the basis for ZM analysis. In this case, knowledge of the incident/observer wave direction relative to the analyzed random process (e.g., the examined ZM) is required to use a ZM to estimate $S(2k\hat{\mathbf{i}})$.

If the random process $\{\gamma(\mathbf{r}')\}$ is isotropic, the correlation coefficient is rotationally symmetric, i.e., $b_\gamma(\mathbf{\Delta r}) = b_\gamma(\Delta r)$, and the BSC can be written as [28]

$$\sigma_b = \frac{k^4}{16\pi^2}\left[\gamma_0^2 \frac{4\pi}{k} \int_0^{\infty} b_\gamma(\Delta r) \sin(2k\Delta r)\ \Delta r\ \mathrm{d}\Delta r\right] \tag{2.12}$$

and in terms of the power spectrum as

$$\sigma_b = \frac{k^4}{16\pi^2} S(2k). \tag{2.13}$$

In this case, the power spectrum does not depend on the incident direction of the plane wave relative to the random process $\{\gamma(\mathbf{r}')\}$. The rotational symmetry of the correlation coefficient and power spectrum in the case of an isotropic medium suggests that radial averaging may be used to reduce the 3D correlation coefficient and power spectrum estimates from a ZM to 1D functions.

If the random process $\{\gamma(\mathbf{r}')\}$ is transverse isotropic, the correlation coefficient and power spectrum exhibit cylindrical symmetry. The axis of symmetry is given by $\hat{\mathbf{t}}$ and aligning the axis of symmetry with the r_1-axis as shown in Fig. 2.2, the correlation coefficient is separable into two functions, i.e., $b_\gamma(\mathbf{\Delta r}) = b_{\gamma,1}(\Delta r_1) b_{\gamma,2}(\tau)$ with τ defined as $\tau^2 = \Delta r_2^2 + \Delta r_3^2$. In this case, the correlation coefficient is isotropic in the Δr_2-Δr_3 plane. Let the angle between the scanning axis and the axis of symmetry be defined as $\cos(\phi) = \hat{\mathbf{t}} \cdot \hat{\mathbf{o}}$; then the BSC can be written as [5, 29]

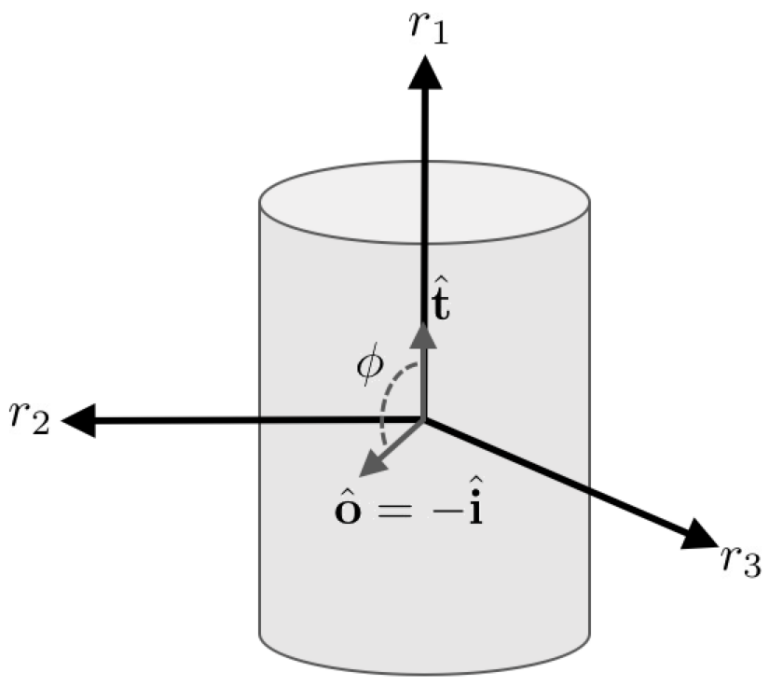

Figure 2.2: Scattering geometry for transverse isotropic medium.

$$\sigma_b = \frac{k^4\gamma_0^2}{8\pi}\left[\int_{-\infty}^{\infty} b_{\gamma,1}(\Delta r_1)e^{-j2k\Delta r_1\cos\phi}\,\mathrm{d}\Delta r_1\right]\left[\int_0^{\infty} b_{\gamma,2}(\tau)J_0(2k\tau\sin\phi)\tau\,\mathrm{d}\tau\right] \tag{2.14}$$

where $J_0(x)$ is the zero order cylindrical Bessel function of the first kind and the Fourier transform relationship for a 2D rotationally symmetric function has been used. In terms of power spectra, the BSC is given as

$$\sigma_b = \frac{k^4\gamma_0^2}{8\pi}\left[S'_{\gamma,1}(2k\cos\phi)\right]\left[S'_{\gamma,2}(2k\sin\phi)\right] \tag{2.15}$$

where $S'_{\gamma,1}(2k\cos\phi)$ and $S'_{\gamma,2}(2k\sin\phi)$ are called normalized power spectra. In this case, assuming that the incident direction is perpendicular to the axis of symmetry, i.e., $\phi = 90°$, 2DZMs created from the r_2-r_3 plane can be used to estimate $S'_{\gamma,2}(2k)$.

Equations 2.10, 2.12, and 2.14 form the basis for ZM analysis using varying assumptions about the correlation coefficient. The key observation from this section is that the BSC is related to the Fourier transform of the correlation coefficient for the random process $\{\gamma(\mathbf{r}')\}$, which is also called the power spectrum for this random process. Therefore, the goal of ZM analysis is to estimate the correlation coefficient and/or the power spectrum of the random process $\{\gamma(\mathbf{r}')\}$ using maps of acoustic tissue properties created using optical or scanning acoustic microscopy. Practical issues related to the estimation of the correlation coefficient and the power spectrum from real 2D slides are discussed in Ch. 3.

2.2 Modeling correlation coefficients and power spectra

Once the correlation coefficient and power spectrum have been estimated for the random process $\{\gamma(\mathbf{r}')\}$ using ZMs, they are usually modeled using simple scattering models, such as the fluid-filled sphere, spherical Gaussian, or exponential models. These models assume that a medium is filled with a single type of scatterer having spatial description given by its 3D spatial correlation coefficient. The Fourier transform of this correlation coefficient is

called the form factor for the model. For a random medium filled with a collection of inhomogeneities, where each individual inhomogeneity is described by the same isotropic model correlation coefficient, the BSC for the medium can be given in terms of the form factor as

$$\sigma_b = \sigma_0 FF(2k) \tag{2.16}$$

where σ_0 is the BSC in the Rayleigh limit and given as [12]

$$\sigma_0 = \frac{k^4 V_s^2 \bar{n} \gamma_0^2}{16\pi^2} \tag{2.17}$$

where V_s is the volume for one scatterer which can be written in terms of a_{eff} and $\bar{n}$ is the number density of the scatterers.

Several isotropic models for simple scatterers exist, e.g., fluid sphere, spherical Gaussian and exponential models. These models have correlation coefficients that are rotationally symmetric, so there is no dependence on the incident vector. The correlation coefficients and form factors for each of these models are shown in Fig. 2.3

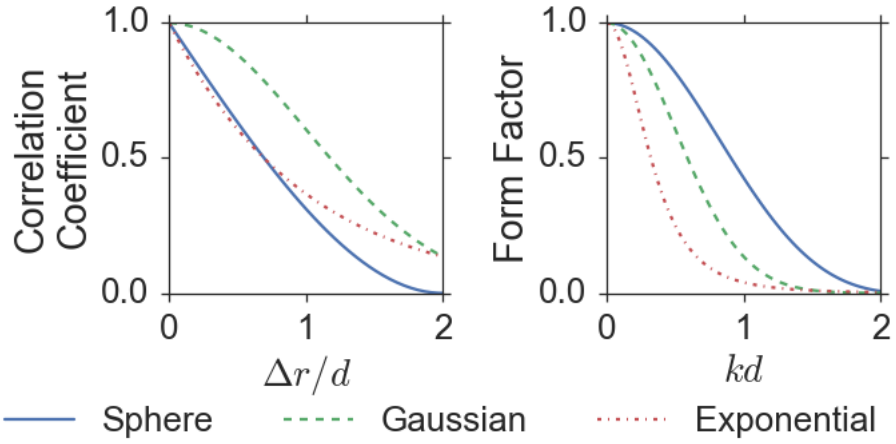

Figure 2.3: Example correlation coefficients and form factors for fluid-filled sphere, Gaussian, and exponential models.

The fluid-filled sphere model has correlation coefficient given by [28]

$$b(\Delta r) = \begin{cases} 1 - \frac{3\Delta r}{4a} + \frac{(\Delta r)^3}{16a^3}, & 0 \leq \Delta r \leq 2a \\ 0, & \Delta r > 2a \end{cases} \tag{2.18}$$

where a is the radius of the modeled sphere and the corresponding form factor is

$$FF(2k) = \left(\frac{3}{2ka} j_1(2ka)\right)^2 \tag{2.19}$$

where $j_1(x)$ is the first order spherical Bessel function of the first kind.

The spherical Gaussian model consists of a particle of infinite support with impedance variation governed by a 3D Gaussian function. Because of its infinite support, this model is not physically realizable; however, this model is used frequently to estimate parameters related to tissue properties [7]. The correlation coefficient for this model is given by [28]

$$b(\Delta r) = e^{-\Delta r^2/2d^2} \tag{2.20}$$

and the corresponding form factor is

$$FF(2k) = e^{-2k^2d^2}. \tag{2.21}$$

The correlation length of the Gaussian function is given by d. The scatterer volume for a model is $V_s = \int_{-\infty}^{\infty} b(\Delta r) dv_\Delta$. An effective scatterer radius can be found by setting this volume equal to the volume of a sphere with radius a_{eff}

$$V_s = \int_{-\infty}^{\infty} b(\Delta r) dv_\Delta = \frac{4}{3}\pi a_{eff}^3 \tag{2.22}$$

and solving for a_{eff}. The effective scatterer radius for the spherical Gaussian model is $a_{eff} = d/(3\sqrt{\pi/2})^{1/3}$.

The exponential model is also not a physical model because it has infinite support. The correlation coefficient for the exponential model is [28]

$$b(\Delta r) = e^{-\Delta r/d} \tag{2.23}$$

and the corresponding form factor is

$$FF(2k) = \frac{1}{(1 + 4k^2d^2)^2}. \tag{2.24}$$

The correlation length of the exponential function is given by d and the

effective scatterer radius for this model is $a_{eff} = d\sqrt[3]{48}/2$.

The most common estimator used for fitting the discussed model functions is the minimum average squared deviation (MASD) [12]

$$\hat{\theta} = \underset{\theta}{\operatorname{argmin}} \int_{s_{\min}}^{s_{\max}} (X(s,\theta) - \bar{X})^2 ds, \tag{2.25}$$

$$X(s,\theta) = 10 \log_{10}(f(s)/f_{model}(s,\theta)) \tag{2.26}$$

where f is the modeled correlation coefficient or form factor, f_{model} is the model that depends on θ which is the size parameter for the model (e.g., a for the fluid sphere model or d for the spherical Gaussian or exponential models), $\bar{X}$ is the mean value of X in the analysis range $[s_{min}, s_{max}]$, $s = \Delta r$ in the case of correlation coefficients and $s = k$ in the case of form factors.

The same type of modeling is possible when estimating the BSC using ultrasound, so parameters using ZMs and ultrasound can be compared. When performing modeling as described in this section, it is necessary to assume that the positions of the inhomogeneities are uncorrelated; otherwise a structure factor will distort the shape of the estimated correlation coefficient and power spectrum using ZMs and the shape of the BSC estimated using ultrasound, leading to errors in the scatterer size estimates.

In conclusion, this section reviews parametric methods for modeling correlation coefficients and power spectra. Parametric modeling in this manner accomplishes two tasks, including dimensionality reduction and interpretation. Correlation coefficients and power spectra live in a high-dimensional space and parametric modeling can be used to project that data onto a lower dimensional space. In addition, parametric models can be interpreted to infer physical properties of the scatterers in the medium such as effective scatterer size.

2.3 Structure function

The development so far has assumed that the scatterer positions are independent. When this assumption fails, a structure function must be added to the BSC to account for the correlations between scatterer positions. Struc-

ture functions have been used previously in modeling backscatter from red blood cells [30–32] and biophantoms [23]. For a collection of monodisperse scatterers, the structure function is defined as

$$S(\mathbf{k}) = 1 + \bar{n} \int_{-\infty}^{\infty} (g(\mathbf{\Delta r}) - 1) e^{-j\mathbf{k}\cdot\mathbf{\Delta r}} d^3\Delta r \tag{2.27}$$

where $\bar{n}$ is the number density of scatterers and $g(\mathbf{\Delta r})$ is the pair correlation function governing the spatial distribution of the scatterers. The pair correlation function is a statistical quantity that is proportional to the probability of finding a second scatterer at a position $\mathbf{\Delta r}$ relative to a first scatterer. The independent positions (IP) pair correlation function is given by

$$g_{IP}(\Delta r) = 1. \tag{2.28}$$

The hole-correction (HC) approximation is a better model for non-overlapping scatterers that enforces a minimal separation between the scatterers

$$g_{HC}(\Delta r) = \begin{cases} 0, & \Delta r \leq 2a \\ 1, & \Delta r > 2a \end{cases} \tag{2.29}$$

where a is the radius of the scatterer. The HC approximation gives a reasonable description of sparsely packed scatterers, but breaks down for dense packings. For a collection of nonoverlapping monodisperse spheres, the Percus-Yevick (PY) approximation is frequently used to solve the Ornstein-Zernike (OZ) equation for the PY pair correlation function $g_{PY}(\Delta r)$. Examples of pair correlation functions are in Fig. 2.4.

The analytic form for the structure function using the PY approximation is [33]

$$S(k) = \frac{1}{1 - \bar{n}C(k)} \tag{2.30}$$

where $C(k)$ is the Fourier transform of the direct correlation function. The direct correlation function is

$$c(x) = \begin{cases} \alpha + \beta x + \delta x^3, & x < 1 \\ 0, & x > 1 \end{cases} \tag{2.31}$$

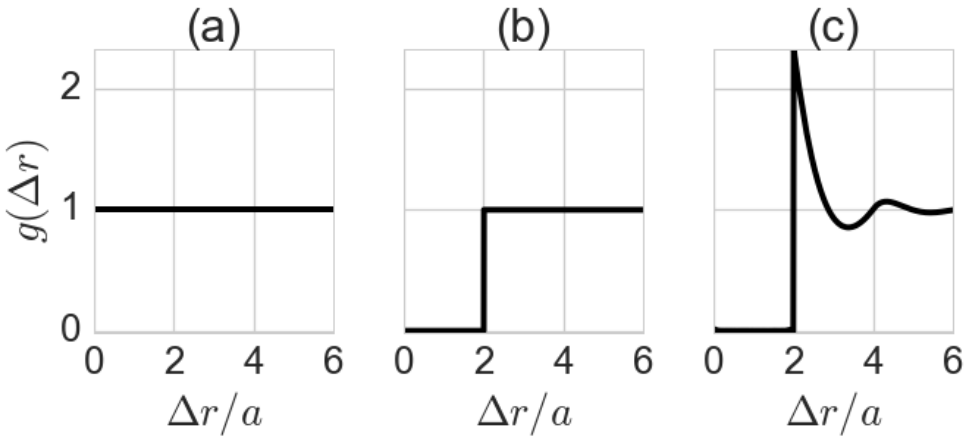

Figure 2.4: Pair correlation function assuming (a) IP, (b) hole-correction approximation, and (c) PY approximation.

where $x = r/2a$, the sphere radius is a, and the constants are

$$\alpha = \frac{(1+2f)^2}{(1-f)^4} \tag{2.32}$$

$$\beta = -6f\frac{(1+f/2)^2}{(1-f)^4} \tag{2.33}$$

$$\delta = \frac{f(1+2f)^2}{2(1-f)^4} \tag{2.34}$$

$$f = \frac{n_o\pi(2a)^3}{6} \tag{2.35}$$

and f is the volume fraction of the spherical scatterers.

To account for the structure function, the BSC in Eq. 2.16 can be modified and written as

$$\sigma_b = \sigma_0 FF(2k)S(2k). \tag{2.36}$$

Examples of the fluid sphere model form factor multiplied by the PY structure function are in Fig. 2.5. These examples show the significant effect that the structure function can have on the shape of the scattering amplitude. These shape changes produce errors in size estimates when modeling power spectra from ZMs or BSCs estimated using ultrasound.

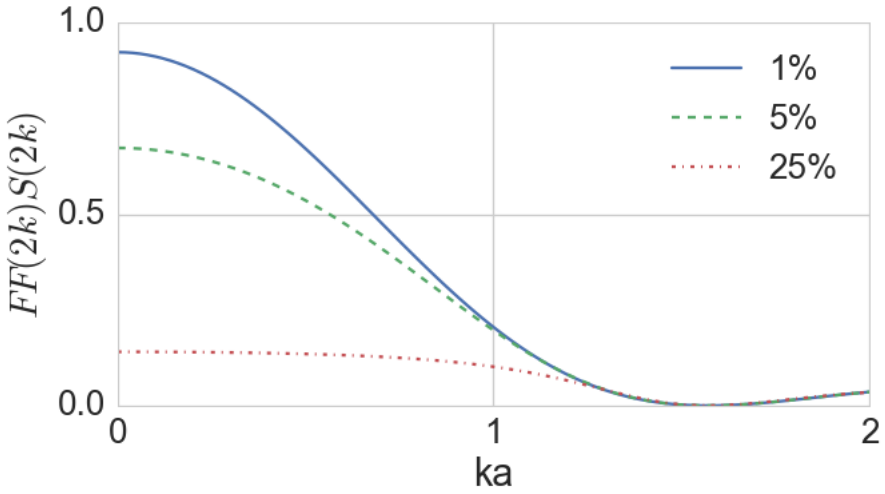

Figure 2.5: Examples of the fluid sphere form factor multiplied by the PY structure function (blue) 1%, (green) 5%, and (red) 25% volume fractions.

In conclusion, this section reviews the structure function. When scatterer spatial positions are independent, the structure function is equal to one and does not affect the estimated BSC. When scatterer spatial positions are not independent, the structure function affects the shape of the BSC. When modeling BSCs, it is necessary to account for this structure function; otherwise, errors will result in the parameter estimates.

2.4 Structure function with container

ZMs are confined to a finite volume called a container. This container will primarily affect the estimated power spectrum and parameters estimated using the power spectrum. Therefore, it is important to predict the effects that the container will have on estimation procedures.

Associated with a container are its shape (e.g., cube, sphere, cylinder, etc.) and its size (characteristic dimension of the container such as side length or diameter). The probability distribution for the scatterer positions is affected by the size and shape of a container. Therefore, a structure function was developed that included the effects of the container and a specified pair correlation function.

A finite collection of monodisperse scatterers in n-dimensions may be de-

scribed mathematically in the following way. A single scatterer centered at the origin is denoted by $h(\mathbf{r})$. For example, a sphere is

$$h(r) = \begin{cases} 1, r \leq a \\ 0, r > a \end{cases} \tag{2.37}$$

where a is the spherical radius and $r = |\mathbf{r}|$. The spatial positions of each scatterer are given by

$$s(\mathbf{r}) = \frac{1}{N} \sum_{n=1}^{N} \delta(\mathbf{r} - \mathbf{r}_i) \tag{2.38}$$

where δ is the Dirac delta function, N is the total number of scatterers in the collection, and $\mathbf{r}_i$ records the position of the ith scatterer. The collection of scatterers is written as

$$f(\mathbf{r}) = N \cdot [h * s] \tag{2.39}$$

where * indicates spatial convolution. The volume power spectrum for the collection of scatterers is given by

$$F(\mathbf{k}) = N \left[H(\mathbf{k}) S(\mathbf{k}) \right] \tag{2.40}$$

where $\mathbf{k}$ is the wavenumber vector, $S(\mathbf{k})$ is the power spectrum of $s(\mathbf{r})$, and $H(\mathbf{k})$ is the power spectrum of $h(\mathbf{r})$. If the scatterer is a sphere, $H(\mathbf{k})$ is

$$H(\mathbf{k}) = \left[3 \frac{j_1(ka)}{ka} \right]^2. \tag{2.41}$$

$S(\mathbf{k})$ is the structure function

$$S(\mathbf{k}) = \frac{1}{N} \left| \sum_{m=1}^{N} e^{-j\mathbf{k} \cdot \mathbf{r}_m} \right|^2 = 1 + \frac{1}{N} \sum_{m \neq n} \cos(\mathbf{k} \cdot \boldsymbol{\Delta}\mathbf{r}_{m,n}) \tag{2.42}$$

where $\boldsymbol{\Delta}\mathbf{r}_{m,n} = \mathbf{r}_n - \mathbf{r}_m$ is the spacing vector between the mth and nth scatterers. The first addend in Eqn. 2.42 is called the incoherent component because it does not depend on $\boldsymbol{\Delta}\mathbf{r}_{m,n}$. The second addend in Eqn. 2.42 is called the coherent component because it is does depend on $\boldsymbol{\Delta}\mathbf{r}_{m,n}$; i.e.,

the spatial positions of the scatterers relative to each other determine the magnitude of this term.

If the scatterer positions are known, the structure function can be computed directly from Eq. 2.42. If the scatterer positions are unknown, the expected value for the structure function can be found from the probability distribution of the scatterer spacings, assuming a random spatial distribution. The expected value of the structure function is given as

$$E\left[S(\mathbf{k})\right] = 1 + \frac{1}{N}\sum_{m\neq n} E\left[\cos(\mathbf{k}\cdot\boldsymbol{\Delta}\mathbf{r}_{m,n})\right]. \tag{2.43}$$

This expected value can be evaluated assuming that only two scatterers are located in the collection

$$E\left[S(\mathbf{k})\right] = 1 + (N-1)E\left[\cos(\mathbf{k}\cdot\boldsymbol{\Delta}\mathbf{r})\right] \tag{2.44}$$

where the expectation is taken with respect to $\boldsymbol{\Delta}\mathbf{r}$ which is governed by the probability distribution $p(\boldsymbol{\Delta}\mathbf{r})$. Then the structure function can be written as

$$E\left[S(\mathbf{k})\right] = 1 + (N-1)\int_{-\infty}^{\infty} p(\boldsymbol{\Delta}\mathbf{r})\cos(\mathbf{k}\cdot\boldsymbol{\Delta}\mathbf{r})d^n\Delta r \tag{2.45}$$

where the integral is over an n-dimensional space. Equation 2.45 is observed to be similar in form to Eq. 2.27 by noting that $g(\boldsymbol{\Delta}\mathbf{r})$ is an even function. Therefore, the exponential kernel in Eq. 2.27 turns into a cosine kernel. The result in Eq. 2.45 suggests that the term $g(\boldsymbol{\Delta}\mathbf{r}) - 1$ in Eq. 2.27 can be interpreted as a probability distribution for the scatterer spacings.

For independent scatterer positions confined to a container, smaller spacings are more likely to occur than large spacings. Therefore, in 3D for a cube container, it is reasonable to assume that the scatterer spacings will follow a triangle distribution along one dimension. It should be noted that a triangle function results when a rectangular function is convolved with itself.

Let an n-dimensional container be specified by $w(\mathbf{r})$. For example, a cube container in 3D with sidelength L and centered at the origin can be written as

$$w_{cube}(\mathbf{r}) = \text{rect}\left(\frac{x}{L}\right)\text{rect}\left(\frac{y}{L}\right)\text{rect}\left(\frac{z}{L}\right) \tag{2.46}$$

where $\text{rect}(x/\tau)$ is a rectangular function centered the origin and having a width of τ. A sphere in 3D with diameter L and centered at the origin can be written as

$$w_{sphere}(r) = \text{sphere}(r/L) = \begin{cases} 1, & r \leq L/2 \\ 0, & r > L/2 \end{cases} \tag{2.47}$$

The spatial autocorrelation function of a container $w(\mathbf{r})$ is defined as $W(\mathbf{\Delta r}) = w(\mathbf{r}) * w(-\mathbf{r})$. For the cube container

$$W_{cube}(\mathbf{\Delta r}) = \text{tri}\left(\frac{\Delta x}{L}\right) \text{tri}\left(\frac{\Delta y}{L}\right) \text{tri}\left(\frac{\Delta z}{L}\right) \tag{2.48}$$

where $\text{tri}(\Delta/\tau)$ is a triangle function centered at the origin and with base length τ. For the sphere container the autocorrelation function is

$$W_{sphere}(\Delta r) = 1 - \frac{3\Delta r}{4(L/2)} + \frac{\Delta r^3}{16(L/2)^3}, \quad 0 \leq \Delta r \leq L. \tag{2.49}$$

The proposed model for the scatterer spacing probability distribution assuming a container with autocorrelation function $W(\mathbf{\Delta r})$ and pair correlation function $g(\mathbf{\Delta r})$ is defined as

$$p(\mathbf{\Delta r}) = \frac{g(\mathbf{\Delta r})W(\mathbf{\Delta r})}{\int g(\mathbf{\Delta r})W(\mathbf{\Delta r})d^n\Delta r}. \tag{2.50}$$

This function satisfies the properties required for a probability distribution and incorporates the pair correlation function of the scatterers and the size and shape the container. Examples of cross sections from 3D scatterer spacing probability distributions are in Fig. 2.6 for different containers and different pair correlation functions.

In the case of IP, analytic forms of the structure function for the cube and sphere containers can be found. For the cube container with sidelength L, the structure function takes the form

$$S(\mathbf{k}) = 1 + (N-1)\left[\text{sinc}^2\left(\frac{k_x L}{2}\right)\ \text{sinc}^2\left(\frac{k_y L}{2}\right)\ \text{sinc}^2\left(\frac{k_z L}{2}\right)\right] \tag{2.51}$$

where $\text{sinc}(x) = \sin(x)/x$. For the sphere container with diameter L, the structure function takes the form

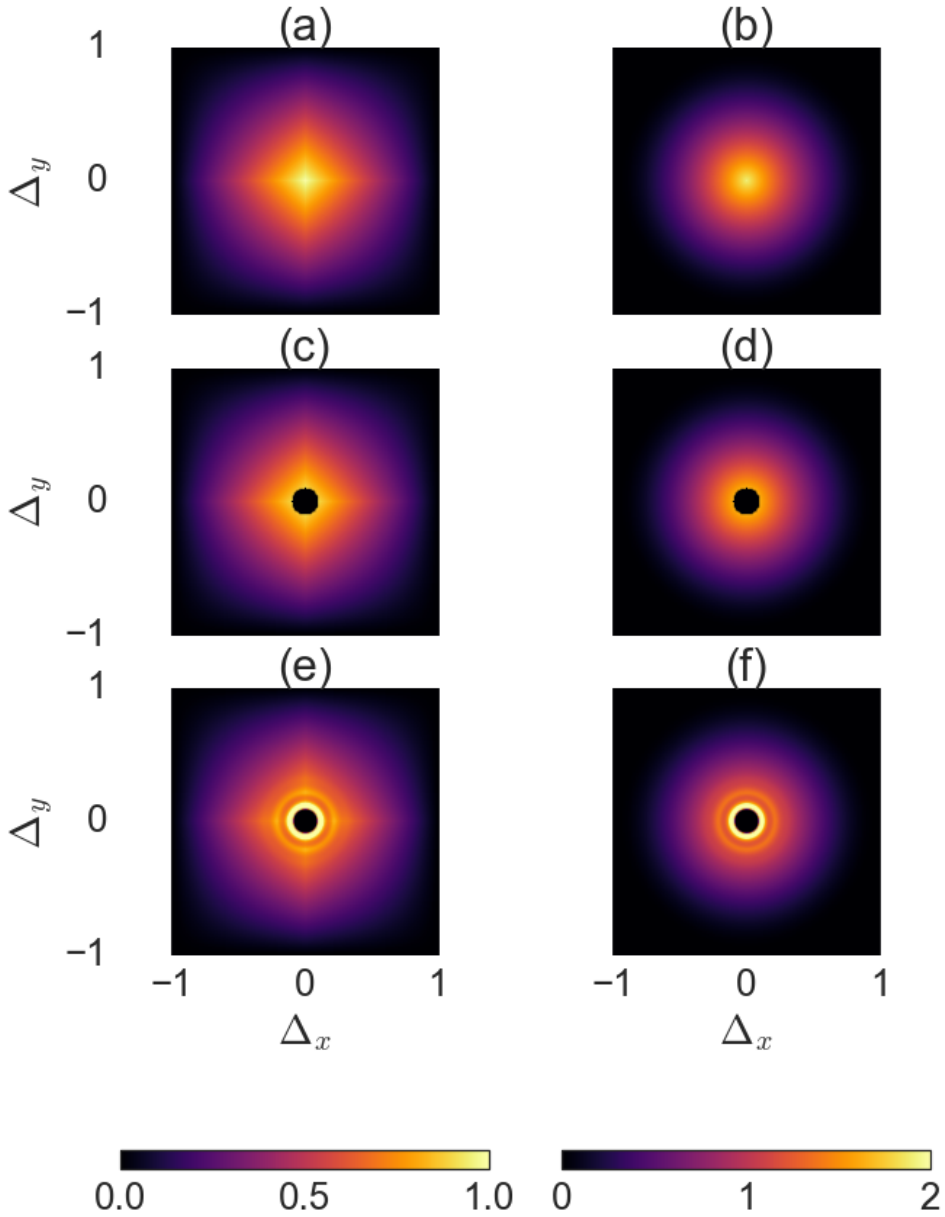

Figure 2.6: Example cross sections from scatterer spacing probability distribution $p(\mathbf{\Delta r})$. Assuming (a, c, e) cube container and (b, d, f) sphere container. Assuming (a, b) IP, (c, d) HC approximation, and (e, f) PY pair approximation. The container length was equal to 1.0 and the spheres had radius 0.05.

$$S(k) = 1 + (N-1)\left[3\frac{j_1(\frac{kL}{2})}{\frac{kL}{2}}\right]^2. \tag{2.52}$$

Radial lines from the IP structure function for a cube container are in Fig.

2.7. This structure function displays a large peak centered at $ka = 0$. This peak results because the cosine function approaches one as ka goes to zero, causing the structure function to approach N. The width of this large peak is controlled by the ratio of the scatter sizes relative to the container size. The width of the peak increases for smaller containers and smaller for larger containers. To avoid having this peak affect the structure function significantly in the ka region of interest, the container dimension must be made large enough relative to the scatterer size.

This structure function for the cube container is not radially symmetric. An on-axis radial line from this structure function displays large amplitude ringing, while an off-axis radial line from this structure function displays much lower amplitude ringing. This result shows that using a cube container introduces anisotropic effects even though the underlying random process (randomly located scatterers) is isotropic. In this case, radial averaging is not appropriate and a different container should be used or off-axis radial lines should be analyzed.

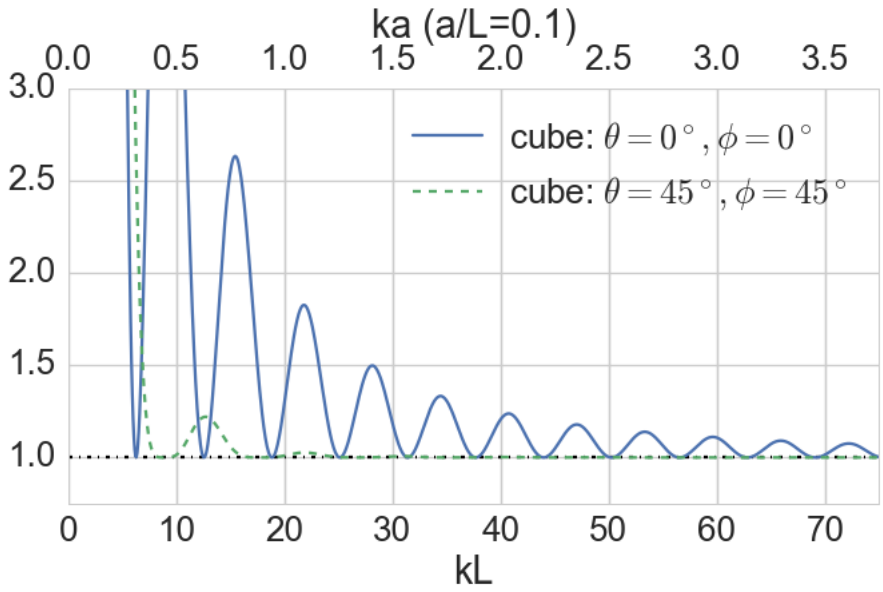

Figure 2.7: Example structure functions assuming IP and a cube container. A total of 100 scatterers were in the container and the ratio of the scatterer radius to the container dimension was $a/L = 0.1$. Two polar/azimuthal angle combinations are shown.

The structure function assuming IP and a sphere container is in Fig. 2.8.

In contrast to the cube container, the sphere container structure function is radially symmetric and radial averaging is acceptable in this case. For the sphere container, the large peak centered at $ka = 0$ is slightly wider than for the cube container. In addition, the sphere container exhibits ringing similar to the cube container. The ringing for the sphere container is significantly less than the observed on-axis ringing in the cube container, but slightly larger than the observed off-axis ringing in the cube container.

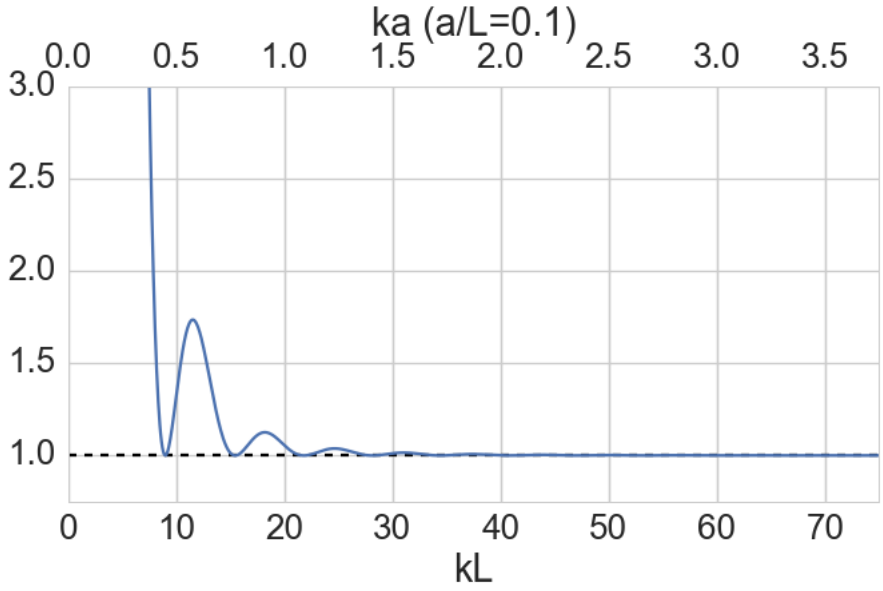

Figure 2.8: Example structure function assuming IP and a spherical container. A total of 100 scatterers were in the container and the ratio of the scatterer radius to the container dimension was $a/L = 0.1$. The function is radially symmetric.

Examples of structure functions for a spherical container and assuming the PY pair correlation function are in Fig. 2.9; i.e., the spacing probability distribution shown in Fig. 2.6 (f) was used. As the container becomes large compared to the scatterer size, the expected behavior was that the structure function with container effects would converge to the PY structure function. The results in Fig. 2.9 show that the structure function model with container followed this behavior.

The largest deviations between the PY structure function and structure function with container were observed for the largest volume fraction. In particular, when the ratio between the scatterer size and container dimension

was 0.3 and the volume fraction was 50%, i.e., the blue curve in Fig. 2.9 (c), significant discrepancies were observed between the PY structure function and the structure function with container effects. For this volume fraction, the PY structure function displayed a large peak in the range $1.5 \leq ka \leq 2$. In contrast, the PY structure function with a container reduced the magnitude of this peak as this structure function was approaching one, i.e., the IP structure function. This behavior can be explained because the container has the effect of filtering the PY pair correlation function shown in Fig. 2.4 (c). When a container is introduced, the large r content in the PY pair correlation function is reduced in magnitude or eliminated, thus reducing is effect on the structure function and causing the structure function with container to not display large peaks similar to the PY structure function.

Similar to the IP structure function for a sphere container, the PY structure function with container displayed a large peak centered at $ka = 0$. The width of this peak was controlled by the size of the container. As the container was made larger, the width of this peak decreased and as the container was made smaller, the width of this peak increased. Making the container large enough so that this large peak does not affect the ka range of interest is an important consideration when determining container size relative to the scatterer size. Based on Fig. 2.9, the ratio between scatterer radius and container length (a/L) should be less than 0.1 to prevent this main peak from affecting the range $ka > 0.5$.

Based on the above observation, a tradeoff exists for the container size. To reduce the effect of the structure function the container should be made as small as possible relative to the scatterer size. The container had the effect of reducing the magnitude of the PY structure function as the size of the container decreased relative to the size of the scatterer. In some cases, it may be desirable to preserve the structure function without container effects and so the container should be made as large as possible. In other cases, it may be desirable to suppress the structure function, so the container should be made as small as possible without having the peak centered at $ka = 0$ affecting the ka range of interest.

Several applications exist for the structure function with container effects. The model was developed to determine the effect of a container on ZM analysis. ZMs are usually confined to a cube, so the structure function with container effects model suggests that on-axis lines from the spectral esti-

mates of a ZM be avoided or that a spherical container be used instead of a cube. The predictions of this model also apply to estimating BSCs from ultrasound signals. When estimating BSCs, there is a lateral cross sectional area associated with the finite aperture of the source and an axial length associated with the length of the time gate used. These dimensions define a container that in the roughest approximation is a cylinder. By adjusting the focal properties of the source or the gate length used for analyzing the signal, the container can be manipulated. Using the proposed model, the effects of the container on the structure function could be studied and used to determine to what degree the container affects BSC estimates from ultrasound signals.

The final application is related to clustering of scatterers. Recent work has proposed using ultrasound to study the aggregation of red blood cells as an indicator of disease [30–32]. In these studies, clusters of red blood cells are modeled as being an effective scatterer with new acoustic properties related to the cluster properties. For example, the effective scatterer might be a sphere or a cylinder. A structure function model is then applied to the effective scatterers to characterize the BSC from blood. The structure function with container could be applied at the level of individual clusters of red blood cells. A container such as a sphere could be assumed for the red blood cells and a structure function with container effects model applied to the collection of red blood cells confined to the sphere. A second structure function could then be assumed for the collection of scattering clusterers. In this way a hierarchical structure function model could be constructed to describe scattering by red blood cell aggregates.

The goal of this section was to develop a structure function that incorporates the effects of confining scatterer positions to a finite container. Standard structure function analysis does not include this constraint on scatterer positions. Instead, the assumption is usually made that the container is large enough so that container effects are not a problem. The developed structure function with container effects can be used to determine the ratio between scatterer size and container size such that container effects would distort the structure function assuming no container effects. In addition, the model suggests that the magnitude of the structure function might be reduced (i.e., the structure function would be closer to one) by making the container smaller.

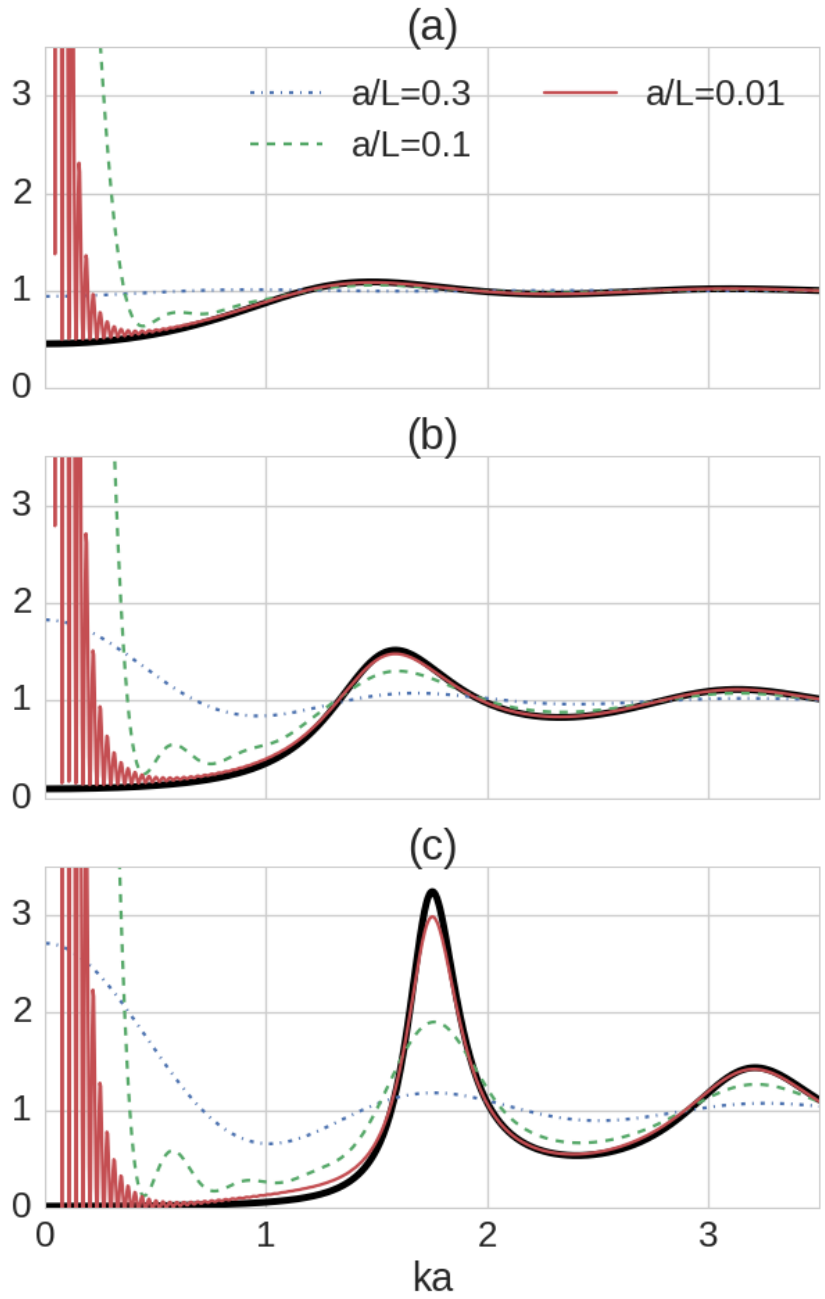

Figure 2.9: Example structure functions assuming PY correlation function and a spherical container. The volume fraction was (a) 10%, (b) 30%, and (c) 50%. The thick black line is the PY structure function without a container.

CHAPTER 3

IMPEDANCE MAP CONSTRUCTION AND ANALYSIS

For a particular biological tissue, the spatial random process that describes the ensemble collection of possible compressibility and density maps for this tissue is denoted by $\{\gamma(r')\}$. An impedance map (ZM) is a computational tool that can be used to characterize $\{\gamma(r')\}$, specifically the correlation coefficient and power spectrum. The reader is referred to the following sources for a complete development of the impedance map method: [16–18, 20, 34–36]. A three-dimensional impedance map (3DZM) is an array stored in the memory of a computer, where each array element is an acoustic impedance value with an associated spatial position in a 3D space. Similarly, a two-dimensional impedance map (2DZM) is an array stored in the memory of a computer, where each array element is an acoustic impedance value with an associated spatial position in a 2D space. Knowledge of acoustic impedance values and their spatial arrangement can be used to estimate the correlation coefficient and power spectrum for $\{\gamma(\mathbf{r}')\}$.

3.1 Constructing ZMs

3.1.1 3DZMs

The process for constructing a 3DZM from a tissue sample has been described before and is included here for completeness [16, 18, 34, 35]. A graphical illustration of the steps is shown in Fig. 3.1.

1. **Histology:** The tissue sample is fixed in formalin, embedded in paraffin, sectioned at a thickness (e.g., 3 μm), placed on glass slides, and a stain such as hematoxylin and eosin (H&E) is applied to highlight the suspected acoustic impedance structures.

2. **Digitization:** Each microscope slide is individually digitized using a microscope with image capture capabilities and having a given pixel resolution. The images are quantized in red, green, and blue color fields (RGB color).

3. **Slice registration:** During the histology preparation and digitization steps, the slices undergo physical transformations, such as shrinking, shearing, translation, etc. The transformation set is unique for each slice. If these transformations are not reversed, they can cause large artifacts in the constructed 3DZMs that have the potential to severely distort estimates of the correlation coefficient and power spectrum. Therefore, it is necessary to apply a slice registration procedure to align the tissue sections.

4. **Image color adjustment:** Slight variation in the thickness of each section results in varying uptake of the H&E stain. Therefore, the color properties of the tissue must be adjusted.

5. **Missing slice interpolation:** Approximately 10% of the tissue sections are inadvertently damaged during the normal histology process, rendering the information from these damaged sections unusable. For example, the sections can be torn or folded over onto themselves. The missing sections must be filled in to complete the reconstruction of the 3D tissue histology map. The missing sections are replaced using cubic Hermite interpolation. The process is repeated independently for each color field and along each stacked column of pixels.

6. **Impedance value assignment:** Each element of the tissue histology map is assigned an acoustic impedance value using the following process. A pink color in the H&E stained image indicates greater protein concentration and a blue color indicates a greater nucleic acid concentration. Therefore, the impedance values can be assigned by associating appropriate acoustic impedance values for each tissue structure with certain color ranges. For example, tissue areas with eosin staining (indicating protein concentration) range in color from light pink to dark pink, while tissue areas with hematoxylin staining (indicating nucleic acid concentration) range in color from light blue to dark blue. Therefore, it is reasonable to assume that the pink image elements

represented cell cytoplasm, while the blue image elements represented cell nuclei. Each tissue structure can be assigned a bulk materials impedance value, which can be increased or decreased proportionally to the amount of color saturation in each pixel. It is also reasonable to assume that elements which appeared very light or white are fat. Table 3.1 provides an example of how impedance values may be assigned based on color ranges. An example of a stained histology image and corresponding impedance map is shown in Fig. 3.2.

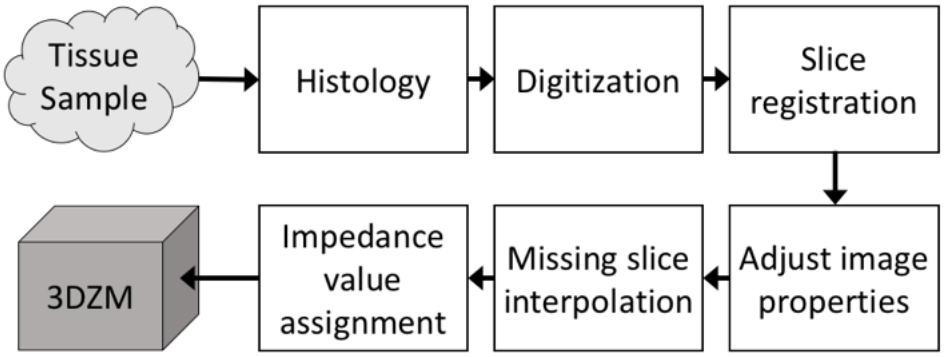

Figure 3.1: 3DZM creation process block diagram.

Table 3.1: Impedance value assignment.

Color	Tissue component	Impedance value range
Light to dark pink	Cytoplasm	1.5 - 1.7 Mrayl
Light to dark blue	Cell Nuclei	1.8 - 2.0 Mrayl
White	Fat	1.45 Mrayl

The 3DZM creation process is not guaranteed to produce a 3DZM that is acceptable for correlation coefficient and power spectral analysis. In addition, the process for constructing a 3DZM is expensive in terms of slide preparation time, computational time, and financial cost. Weaknesses of the 3DZM construction process are summarized below.

1. A large set of histological slides need to be meticulously stained, optically scanned, and digitized.

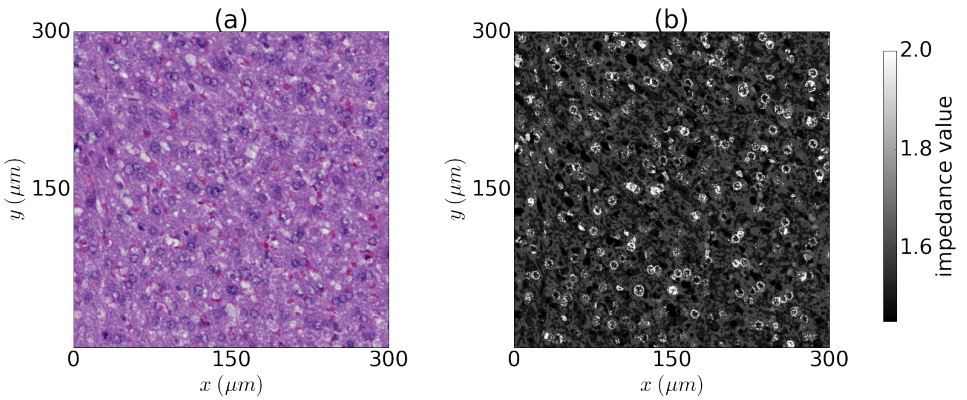

Figure 3.2: (a) Stained histology image and corresponding (b) impedance map from a rabbit liver.

2. During the slice registration step, if the actual physical transformations experienced by the slides during ZM preparation are not included in this set, it is impossible to correctly align the slides.

3. Standard interpolation methods for missing slides are not guaranteed to adequately account for the missing slides.

4. The spatial sampling rate perpendicular to the slice plane is limited by the minimum thickness that can be cut using a microtome. Currently, the spatial sampling rate perpendicular to the slice plane is approximately 6.5 times the spatial sampling rate in the slice plane.

5. Large discontinuities can be introduced at multiple stages in the 3DZM processing pipeline and these discontinuities can lead to distortions in the estimated correlation coefficient and power spectrum.

6. There is a sampling issue with the 3DZMs. A single 3DZM typically represents a resolution cell size or smaller of a medical ultrasonic imaging system. Therefore, large numbers of 3DZMs need to be constructed to represent a tissue volume, such as a tumor.

The goal of this section was to review the 3DZM construction process. In addition, a number of weaknesses of the 3DZM method were identified. The weakness of the 3DZM method motivates the development of improved ZM analysis methods. A method based on analyzing 2DZMs would avoid many of the described shortcomings of the 3DZM method.

3.1.2 2DZMs

The process for constructing a 2DZM from a tissue sample is a subset of the process for constructing a 3DZM and is summarized in Fig. 3.3. A 3DZM is a collection of 2DZMs that have been registered and aligned, and any missing 2DZMs have been accounted for using interpolation.

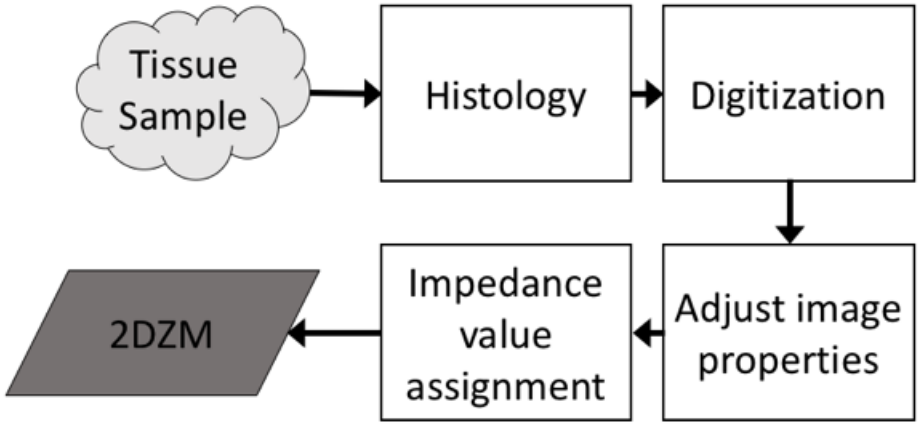

Figure 3.3: 2DZM creation process block diagram.

Comparing the 2DZM process to the 3DZM process, the slice registration and missing slice interpolation steps are not needed when constructing 2DZMs. Slice registration is an important step in the 3DZM process because this step can cause large artifacts in the constructed 3DZMs. These large artifacts have the potential to severely distort the estimates of the correlation coefficient and power spectrum. When analyzing the 2DZMs included in a 3DZM independently of each, the chance of these distortion effects is prevented. The missing interpolation step is another source of error for the correlation coefficient and power spectrum estimate. These errors can distort the shape of the estimated correlation coefficient and power spectrum.

Another disadvantage of the 3DZM compared to the 2DZM appears when considering tissues that are heterogeneous. To obtain good estimates from a 3DZM requires multiple independent 3DZMs. While many 2DZMs would also be needed, increasing the number of 2DZMs in an analysis comes at

a much smaller cost compared to increasing the number of 3DZMs in an analysis.

The main advantage of the 3DZM compared to the 2DZM is that 3DZMs provide more independent radial lines for averaging when estimating the correlation coefficient and power spectrum compared to using a single 2DZM. Increasing the number of independent estimates available for averaging improves correlation coefficient and power spectral estimates. However, this advantage does not apply to anisotropic media because radial averaging is not appropriate for an anisotropic medium.

In conclusion, this section described the 2DZM construction process and compared it to the 3DZM construction process. The 2DZM construction process has fewer opportunities for large errors to be introduced into the ZM analysis. Reducing large discontinuities in ZM analysis is desirable to reduce error when using ZMs to estimate form factors or to identity scattering sites in a specific tissue.

3.2 Estimating the correlation coefficient and power spectrum

3.2.1 Correlation coefficient

Estimating the correlation coefficient is an important step in ZM analysis. The correlation coefficient can be modeled to estimate parameters related to tissue properties and can also be used to estimate the power spectrum. For an $M \times N \times P$ matrix $Z[i,k,l]$, where the integer $i = \{0,1,...,M-1\}$ is associated with the z-direction, $k = \{0,1,...,N-1\}$ is associated with the y-direction, and $l = \{0,1,...,P-1\}$ is associated with the x-direction, the correlation coefficient was estimated using

$$\hat{b}[m,n,p] = \frac{1}{N_v} \sum_{i=0}^{M-1} \sum_{k=0}^{N-1} \sum_{l=0}^{P-1} Z[i+m, k+n, l+p]\, Z[i,k,l]\,. \tag{3.1}$$

The integer indices can be converted to a spatial coordinate using $z_i = i\Delta z$, $y_k = k\Delta y$, and $x_l = l\Delta x$, where Δz, Δy, and Δx are the spatial sampling

periods in each direction. The integer $m = \{-(M-1), -(M-2), ..., M-2, M-1\}$ is associated with the spatial lag in the z-direction, the integer $n = \{-(N-1), -(N-2), ..., N-2, N-1\}$ is associated with the spatial lag in the y-direction, and the integer $l = \{-(P-1), (P-2), ..., P-2, P-1\}$ is associated with the spatial lag in the x-direction. N_v is a normalizing term equal to the number of matrix elements used in the triple summation for a specific combination (m, n, p).

Similarly, for an $M \times N$ matrix $Z[i,k]$, the correlation coefficient was estimated using

$$\hat{b}[m,n] = \frac{1}{N_p} \sum_{i=0}^{M-1} \sum_{k=0}^{N-1} Z[i+m, k+n] Z[i,k] \tag{3.2}$$

where the integers i, k, m, n are defined similarly to the 3D case. N_p is a normalizing term equal to the number of matrix elements used in the double summation for a specific combination (m, n).

3.2.2 Power spectrum

Direct estimation of the power spectrum without estimating the correlation coefficient is possible using the discrete Fourier transform. For an $M \times N \times P$ matrix $Z[i,k,l]$, the power spectrum can be estimated as

$$\hat{S}[m,n,p] = \left| \frac{1}{MNP} \sum_{i=0}^{M} \sum_{k=0}^{N} \sum_{l=0}^{P} Z[i,k,l] \, e^{-j2\pi(m \cdot i/M + n \cdot k/N + p \cdot l/P)} \right|^2 \tag{3.3}$$

where the integers i, k, and l represent spatial coordinates and are defined in the same way as for estimating the correlation coefficient. However, the integers m, n, and p are associated with spatial frequency. The spatial frequencies can be found using $k_i = 2\pi m/\Delta z$, $k_k = 2\pi n/\Delta y$, and $k_l = 2\pi l/\Delta x$. The relationship between the modulus squared of a discrete Fourier transform and power spectrum is given by the Wiener-Khintchine theorem [37].

Similarly, for an $M \times N$ matrix $z[i,k]$, the power spectrum can be estimated as

$$\hat{S}\left[m,n\right]=\left|\frac{1}{MN}\sum_{i=0}^{M}\sum_{k=0}^{N}Z\left[i,k\right]e^{-j2\pi(m\cdot i/M+n\cdot k/N)}\right|^{2} \tag{3.4}$$

where the integers i, k, m, n are defined similarly to the 3D case. Efficient evaluation of the discrete Fourier transforms in Eqs. 3.3 and 3.4 is possible using the fast Fourier transform (FFT).

3.2.3 Radial averaging

Description of radial averaging

Several of the methods that will be proposed for estimating the correlation coefficient and power spectrum rely on using a radial average over a 2D or 3D rectangular grid of values. When an isotropic assumption can be made, radial averaging may be used to reduce a 2D or 3D sampled function to a 1D sampled function. Reducing to a 1D sampled function is a necessary step when using 2DZMs to estimate a 3D power spectrum.

Radial averaging was applied using a binning procedure that is illustrated for the 2D case in Fig. 3.4. The spatial sampling periods were Δx and Δy along the x-axis and y-axis, respectively. The widths of the bins used were $h=\max\{\Delta x,\Delta y\}$, a condition which prevents the existence of empty bins. The first bin consisted of a circle centered at the coordinate origin for the rectangular grid and having radius h. The second bin consisted of the annulus surrounding the first bin and having width h. The third bin consisted of the annulus surrounding the first two bins and having width h. The bins were built up in this manner to cover the entire rectangular grid. For each bin, the rectangular grid points included in the bin were averaged to estimate the radial function for the radial spatial coordinate at the center of the bin annulus. A similar procedure was used in 3D, except spherical shells with width h were used instead of annuli.

Radial averaging has the advantage of decreasing the error in the estimated correlation coefficient. This can be observed in Fig. 3.5 which shows several radial lines from the correlation coefficient estimated from a 2D section of a random process governed by a spherical Gaussian correlation function. The blue lines are lines extracted at different radial directions from the 2D corre-

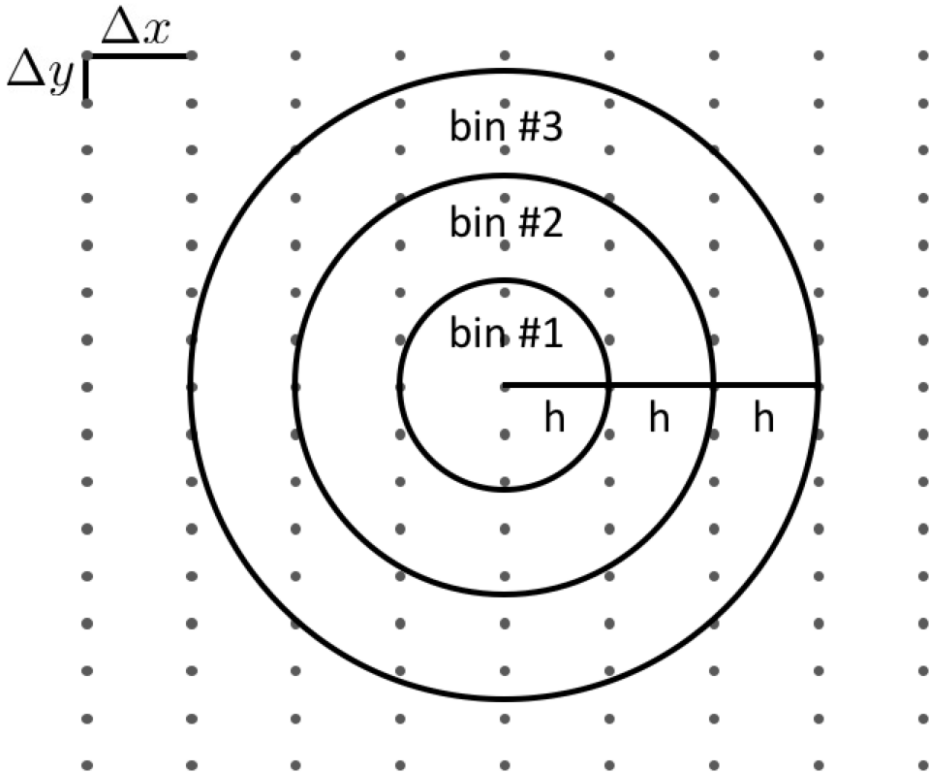

Figure 3.4: Binning procedure used to perform radial averaging in 2D. The spacing between adjacent grid points was Δx and Δy along the x-axis and y-axis, respectively, and the bin widths were $h = \max\{\Delta x, \Delta y\}$. The first bin was centered at the coordinate origin of the rectangular grid. The second bin consisted of an annulus surrounding the first bin and having width h. The values of the grid points in each bin were averaged to perform radial averaging.

lation coefficient estimated from a 2D section of a spherical Gaussian random process. The black line is the average of all of the blue lines. The dashed red line is the theoretical correlation coefficient for a spherical Gaussian random process. Clearly the black line has less error relative to the dashed red line than the individual blue lines.

Grid size and scatterer size estimate error when radial averaging

The effect of grid spacing on 3D sampled functions produced with radial averaging is illustrated in Fig. 3.6 using the fluid sphere, spherical Gaussian, and exponential model functions (correlation coefficient and form factor) discussed in Sec. 2.2. These model functions in 1D are shown in Fig. 2.3.

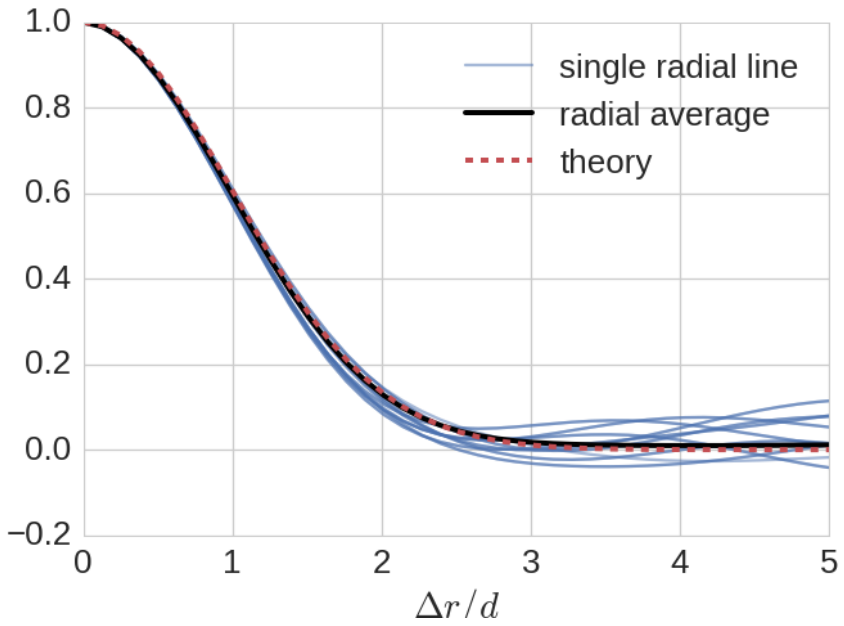

Figure 3.5: The blue lines are lines extracted at different radial directions from the 2D correlation coefficient estimated from a 2D section of a spherical Gaussian random process. The black line is the average of all of the blue lines. The dashed red line is the theoretical correlation coefficient for a spherical Gaussian random process.

To test the effect of the number of grid points used to sample a function, the function was sampled using a specified number of grid points along each dimension. The correlation coefficient was sampled in the spatial lag range $-2 \leq \{\Delta r_x, \Delta r_y, \Delta r_z\}/d \leq 2$ and the form factor was sampled in the spatial frequency range $-2 \leq \{k_x, k_y, k_z\}d \leq 2$. A radial average was performed to find a 1D sampled function from the 3D sampled function and the size was estimated based on the 1D sampled function. Percentage error between actual size and estimated size are shown when using the correlation coefficient and form factor. The error curves are shown in terms of the number of grid points along each axis used to sample the function in 3D.

When using a small number of grid points to sample the functions, errors in the estimated sizes were in excess of 20%. To achieve an error in estimated size less than 5% for all models, 15 and 25 grid points along each dimension were needed when using the correlation coefficient and form factor, respectively. When using the correlation coefficient to estimate sizes, the spherical Gaussian model performed best when using the correlation coefficient and

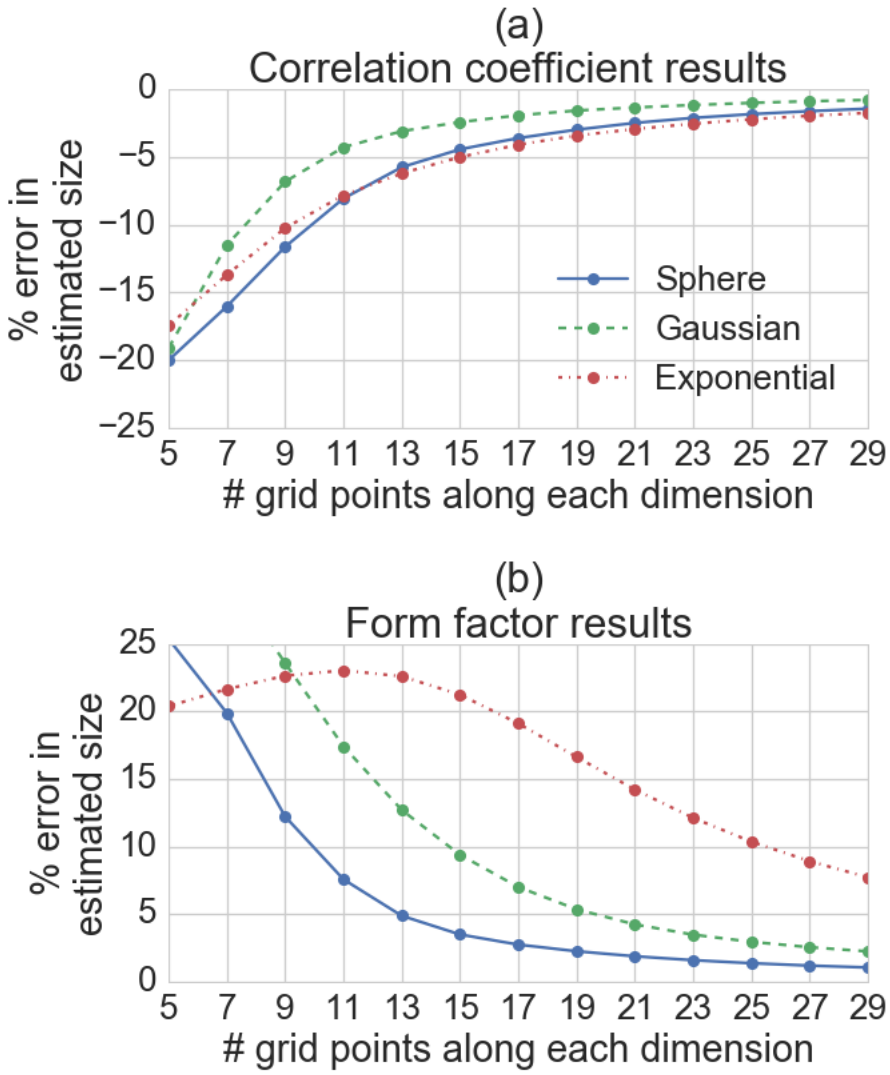

Figure 3.6: Percentage errors between actual size and estimated size are shown when studying the (a) correlation coefficient and (b) form factor of the (blue) fluid sphere, (green) spherical Gaussian, and (red) exponential models. The x-axis represents the number of grid points used along each dimension when sampling the functions in 3D. The spatial lag range $0 \leq \Delta r/d \leq 2$ was used for the correlation coefficient and the spatial frequency range $0 \leq kd \leq 2$ was used for the form factor.

the fluid sphere model performed best when using the form factor. The sizes were underestimated when using the correlation coefficient and overestimated when using the form factor.

The errors from using a radial averaging process for the purpose of reducing

a 3D sampled function to a 1D sampled function were quantified using correlation coefficient and form factor functions from the fluid sphere, spherical Gaussian, and exponential models. The analysis of these model functions is useful for determining the extent to which radial averaging introduces errors into size estimates.

3.3 Foundations of 2DZM analysis

3.3.1 Correlation functions as linear systems

The correlation function for a random process in an n-dimensional space is a linear system. For example, consider an arbitrary spatial random process $\gamma(x, y, z)$ in 3D; the correlation function is

$$B(\Delta x, \Delta y, \Delta z) = \int_{-\infty}^{\infty}\int_{-\infty}^{\infty}\int_{-\infty}^{\infty}\gamma(x+\Delta x, y+\Delta y, z+\Delta z)\gamma(x, y, z)\mathrm{d}x\mathrm{d}y\mathrm{d}z. \tag{3.5}$$

Next, this correlation function is found for a plane that is perpendicular to the Δz dimension and that passes through the origin

$$B(\Delta x, \Delta y, 0) = \int_{-\infty}^{\infty}\int_{-\infty}^{\infty}\int_{-\infty}^{\infty}\gamma(x+\Delta x, y+\Delta y, z)\gamma(x, y, z)\mathrm{d}x\mathrm{d}y\mathrm{d}z. \tag{3.6}$$

Separating the integral along the z dimension,

$$B(\Delta x, \Delta y, 0) = \int_{-\infty}^{\infty}\left[\int_{-\infty}^{\infty}\int_{-\infty}^{\infty}\gamma(x+\Delta x, y+\Delta y, z)\gamma(x, y, z)\mathrm{d}x\mathrm{d}y\right]\mathrm{d}z. \tag{3.7}$$

And the integration on the inside of the brackets is a 2D correlation function that depends on z

$$B(\Delta x, \Delta y, 0) = \int_{-\infty}^{\infty} B_{2D}(\Delta x, \Delta y, z)\mathrm{d}z. \tag{3.8}$$

This development could be repeated for any planar section that passes through

the origin.

The key observation from this section is that planar sections were shown to be all that was necessary to find a planar section from a volume correlation function. It should be noted that this development does not place restrictions on the correlation function for the examined random process and therefore applies to anisotropic random processes. To use the result in this section requires that all slices be available for the analysis. In future developments, restrictions will be placed on the correlation function for the random process to relax the requirement that all slices be available for the analysis.

Another important observation is that the correlation function for the 2D sections does not include information about how the sections have been translated relative to each other. This fact implies that relative slice translations do not need be reversed when averaging the 2D correlation functions.

Assuming that the correlation function is anisotropic, the obtained planar section from the volume correlation function will not be radially symmetric. Therefore, relative section rotation would need to be taken into account when doing the averaging. In other words, the rotationally variant structure observed in the correlation function from the individual 2D sections needs to be aligned before averaging.

The development in this section shows that 2DZM analysis can be used to find information about 3D volumetric structure. To reiterate, no restrictions were placed on the correlation function for the random process under consideration; i.e., the planar section from the 3D volume correlation function could be found exactly for a random process with an anisotropic correlation function when all 2D sections were available. From a theoretical perspective, the development in this section definitively demonstrates that 2DZM analysis can replace 3DZM analysis.

3.3.2 Power spectra and the projection-slice theorem

In contrast to the correlation function, the estimated power spectrum is not a linear system with respect to a ZM. However, the projection-slice theorem can still be used to transform a 3D analysis into a 2D analysis. The estimated power spectrum for a ZM $\gamma(\mathbf{r}')$ is

$$\hat{S}(k_x, k_y, k_z) = \left| \int_{-\infty}^{\infty} \int_{-\infty}^{\infty} \int_{-\infty}^{\infty} \gamma(x, y, z) e^{-j(k_x x + k_y y + k_z z)} \mathrm{d}x\mathrm{d}y\mathrm{d}z \right|^2 . \quad (3.9)$$

Next, this power spectrum is found for a plane that is perpendicular to the k_z dimension and that passes through the origin

$$\hat{S}(k_x, k_y, 0) = \left| \int_{-\infty}^{\infty} \int_{-\infty}^{\infty} \int_{-\infty}^{\infty} \gamma(x, y, z) e^{-j(k_x x + k_y y)} \mathrm{d}x\mathrm{d}y\mathrm{d}z \right|^2 . \quad (3.10)$$

Evaluating the integral along the k_z dimension,

$$\hat{S}(k_x, k_y, 0) = \left| \int_{-\infty}^{\infty} \int_{-\infty}^{\infty} P_{\gamma,z}(x, y) e^{-j(k_x x + k_y y)} \mathrm{d}x\mathrm{d}y \right|^2 . \quad (3.11)$$

where $P_{\gamma,z}(x, y)$ is the projection of γ along the z-direction. Any planar section that passes through the origin from a 3D power spectral estimate can be written as a Fourier transform of the projection of the ZM onto a plane that is perpendicular to the z direction and that passes through the origin. This result is a statement of the projection-slice theorem.

This section shows that a slice passing through the origin of a 3D power spectral estimate can be estimated by finding the Fourier transform of the projection of the ZM onto a plane. Compared to the development of the correlation function as a linear system, this result is not as useful because full construction of a 3DZM is still necessary to find the projection of the 3D volume. However, it could still be useful in the case when missing slices are a major problem as the projection operation will be more immune to these effects compared to a full 3DZM analysis.

3.3.3 Fourier transform relationships

The methods that will be utilized for estimating a power spectrum using ZMs for the purpose of evaluating the BSCs in Eqs. 2.11, 2.13, and 2.15 require special Fourier transform relationships. For the case of an anisotropic random process, the rectangular coordinate Fourier transform pair given for an arbitrary n-dimensional space and shown in Table 3.2 is used to evaluate

the BSC.

Table 3.2: Fourier transform pair in rectangular coordinates for an n-dimensional space.

Dimension	Direction	Fourier transform relation
n	Forward	$S_n(\mathbf{K}) = \int_{\mathbb{R}^n} \exp(-j\mathbf{K}\cdot\mathbf{\Delta r}) d^n\Delta r$
n	Inverse	$b_n(\mathbf{\Delta r}) = \int_{\mathbb{R}^n} \exp(j\mathbf{K}\cdot\mathbf{\Delta r}) d^n k$

For the case of isotropic and transverse isotropic random processes, Fourier transform relationships for rotationally symmetric functions may be used to evaluate the BSCs in Eqs. 2.13 and 2.15. These relationships are shown in Table 3.3.

An important property of isotropic random processes is emphasized in Table 3.3. An isotropic random process in $\mathbb{R}^n$ having correlation coefficient $b(\Delta r)$ has the property that for any positive integer (n-m) the values of this process on an arbitrary (n-m)-dimensional subspace of the original n-dimensional space form an isotropic random process with correlation coefficient $b(\Delta r)$ [38]. Therefore, the correlation functions indicated in Table 3.3 do not depend on the number of dimensions. This property concerning the correlation coefficient for isotropic random processes serves as the foundation for 2DZM analysis. In general, power spectra in different dimensions are not equal to each other and therefore the power spectra in Table 3.3 do depend on the number of dimensions. In some special cases, e.g., the spherical Gaussian model, power spectra in different dimensions are equal to each other.

For a random process with a given rotationally symmetric correlation coefficient, the power spectrum in an (n-m)-dimensional space can be written in terms of an integral over the power spectrum in an n-dimensional space [15]

$$S_{n-m}(k) = \int_{\mathbb{R}^m} S_n(\sqrt{k^2 + (k')^2}) d^m k' \tag{3.12}$$

where

$$\sqrt{k = k_1^2 + k_2^2 + ... + k_{n-m}^2} \tag{3.13}$$

Table 3.3: Fourier transform pairs of rotationally symmetric functions in one-, two-, and three-dimensional spaces. $J_0(x)$ is the zero order cylindrical Bessel function of the first kind.

Dimension	Direction	Fourier transform relation
1	Forward	$S_1(k) = 2\int_0^\infty b(\Delta r)\cos(k\Delta r)d\Delta r$
2	Forward	$S_2(k) = 2\pi\int_0^\infty b(\Delta r)\Delta r J_0(k\Delta r)d\Delta r)$
3	Forward	$S_3(k) = \frac{2}{k}\int_0^\infty b(\Delta r)\Delta r\sin(k\Delta r)d\Delta r$
1	Inverse	$b(\Delta r) = 2\int_0^\infty S_1(k)\cos(k\Delta r)dk$
2	Inverse	$b(\Delta r) = 2\pi\int_0^\infty S_2(k)kJ_0(k\Delta r)dk$
3	Inverse	$b(\Delta r) = \frac{2}{\Delta r}\int_0^\infty S_3(k)k\sin(k\Delta r)dk$

and

$$\sqrt{k' = k_{n-m+1}^2 + k_{n-m+2}^2 + ... + k_n^2}. \tag{3.14}$$

The geometric interpretation of this integration is that it is a projection from a higher dimensional space onto a lower dimensional space.

Another useful Fourier transform relationship that was derived by Waag et al. relates the 3D power spectrum to the 1D power spectrum [15]

$$S_3(k) = -\frac{1}{2\pi k}\frac{d}{dk}S_1(k). \tag{3.15}$$

The Fourier transform relationships and isotropic random process properties discussed in this section form the basis for the 2DZM analysis methods of isotropic random media that will be proposed. In particular, these relationships imply that the 3D correlation function and power spectrum can be estimated from a single 2D slice. Without these relationships, performing a 2DZM analysis would require that all 2DZMs be included to estimate the correlation function and power spectrum for a 3D random process with low error.

3.4 Estimating BSCs using ZMs

3.4.1 Using compounding to reduce BSC estimate variance

If a single ZM is used to estimate the BSC for the random process $\{\gamma(\mathbf{r}')\}$, the estimated power spectrum will suffer from high variance. Reducing this variance is desirable when using the BSC in a diagnostic task because the variance will decrease the classification performance. Several methods exist for reducing variance, including ensemble averaging, spatial compounding, and angular compounding.

In the case of ensemble averaging, multiple ZMs are acquired from different realizations of the same biological tissue. Power spectral estimates are calculated for each ZM and averaged to reduce variance and better estimate the true BSC for the random process $\{\gamma(\mathbf{r}')\}$ associated with the examined tissue region.

When the random process $\{\gamma(\mathbf{r}')\}$ is stationary, spatial averaging may be used to reduce variance. In this case, ZMs are created from different regions of the same tissue/organ realization and the collection of BSC estimates from these ZMs are averaged to reduce variance and obtain a better estimate for the true BSC for the examined tissue structure. Spatial compounding in this manner is frequently used when estimating the BSC using ultrasound, when the RF signal from a region of interest is divided into small data blocks and the BSC estimates for the collection of data blocks are averaged.

When the random process $\{\gamma(\mathbf{r}')\}$ is isotropic, the BSC no longer depends on the incident angle of the acoustic plane wave. In this case, radial averaging can be applied to the correlation coefficient and power spectral estimates of a ZM to obtain a better estimate of the true BSC for the examined biological tissue.

All of these compounding methods can be combined to provide better estimates of the correlation coefficient and power spectrum for the random process $\{\gamma(\mathbf{r}')\}$. Averaging independent estimates reduces the variance of the estimated quantities, leading to better estimates of the true BSC associated with a biological tissue and to increased performance when using the BSC for disease classification and better resolution for therapy monitoring.

3.4.2 3DZM method #1

The Wiener-Khinchin theorem relates the Fourier transform of the spatial correlation coefficient given in Eq. 2.10 to the squared magnitude of the 3D spatial Fourier transform of a realization $\gamma(\mathbf{r}')$ [37]. For a 3DZM, the power spectrum for the random process $\{\gamma(\mathbf{r}')\}$ can be estimated using a 3DZM using the spectral estimator in Eq. 3.3. If the random process is anisotropic, it is necessary to extract the line from this 3D power spectral estimate that corresponds to the incident ultrasound wave propagation direction. Otherwise, if the random process is isotropic, radial averaging can be used to estimate the function $S(2k)$ from Eq. 2.12. Currently, 3DZMs are processed using the method described in this section as 3DZM method #1 [16–18, 20].

3.4.3 3DZM method #2

Instead of directly estimating the power spectrum using the method described above, the 3DZM can be used to estimate the correlation coefficient using Eq. 3.1. The power spectrum can then be estimated using the discrete Fourier transform. Similar to above, if the random process is anisotropic, it is necessary to extract the line from the discrete Fourier transform that corresponds to the corresponding incident ultrasound propagation direction. Otherwise, if the random process is isotropic, radial averaging can be used to estimate the rotationally symmetric function $b(\Delta r)$ in Eq. 2.12.

3.4.4 2DZM method #1 for isotropic media

Given an isotropic random process in 3D with correlation coefficient $b(\Delta r)$, this isotropic random process will have the same correlation coefficient in a 2D space [38]. Based on this fact, the following process can be used to estimate the 3D power spectrum in Eq. 2.13 and ultimately the BSC:

1. The correlation coefficient was estimated for 2D slices using Eq. 3.2. If more than one slice was available for the analysis, the resulting correlation coefficients were averaged together. The result was a 2D correlation coefficient.

2. Radial averaging was performed on the 2D correlation coefficient to obtain a 1D correlation coefficient.

3. The estimated correlation coefficient was substituted into Eq. 2.12 to estimate the BSC. Numerical integration was used to evaluate the integral of Eq. 3.2.

3.4.5 2DZM method #2 for isotropic media

For an isotropic random process in 3D, Waag et al. proposed the following process for estimating the 3D power spectrum from the 2D power spectrum [15]:

1. The power spectrum in a 2D space was estimated using the discrete Fourier transform in Eq. 3.4. If more than one slice was available for the analysis, the resulting power spectra were averaged together to produce a single 2D power spectral estimate.

2. Radial averaging was performed on the 2D power spectrum to obtain a 1D power spectrum.

3. The relationship for the 2D inverse Fourier transform in Table 3.3, which relates the 2D power spectrum to the correlation coefficient was used to estimate the correlation coefficient.

4. The relationship for the 3D forward Fourier transform in Table 3.3, which relates the 3D power spectrum to the correlation coefficient, was used to estimate the 3D power spectrum.

The disadvantage of this method compared to 2DZM method #1 is that the correlation coefficient estimated from the power spectrum can be estimated directly without first estimating the 2D power spectrum. There is no need to first estimate the power spectrum of the slices if the correlation coefficient from slices can be estimated without estimating the power spectrum. For this reason, 2DZM method #1 is preferred over 2DZM method # 2.

3.4.6 2DZM method #3 for isotropic media

For an isotropic random process in 3D, Waag et al. proposed the following process for estimating the 3D power spectrum from the 2D power spectrum [15]:

1. Convert the 2D power spectrum into a power spectrum of scattering in a 1D space using Eq. 3.12. This step can be accomplished by summing the vertical coordinates for each horizontal coordinate in the 2D power spectrum.

2. Convert the 1D power spectrum into a 3D power spectrum using Eq. 3.15

In this 2DZM method, the analysis takes place entirely in the frequency domain. When using this method, a correlation coefficient estimate is never estimated. In addition, this method relies on numerical differentiation, a step that can amplify noise. For these reasons, 2DZM method #1 is preferred over 2DZM method #3.

3.4.7 2DZM method for transverse isotropic media

The following process can be used to estimate the 1D and 2D power spectra needed to evaluate Eq. 3.4. Extract 2D slices from the medium that are in the same plane as the r_2-r_3 plane as shown in Fig. 3.7. The propagation direction for the ultrasound should be in the r_2-r_3 plane. The 2D correlation coefficient and 2D power spectrum can be estimated based on these slices to obtain estimates for $b_{\gamma,2}$ and $S_{\gamma,2}$ in Eqs. 2.14 and 2.15 . Next, the variation along the r_1 plane needs to be characterized and can be accomplished in several different ways. For example, the correlation coefficient along the r_1 axis can be estimated by studying sequential slices. As an alternative, the medium can be assumed to be constant along the r_1 axis so that $b_{\gamma,1}(\Delta r_1) = 1$ and $S_{\gamma,1}(k_x) = \delta(k_x)$. The 2D power spectrum can be estimated using the squared magnitude of the 2D spatial Fourier transform as given in Eq. 3.4.

It should be noted that converting between power spectra of different dimensions is not necessary when examining a transverse isotropic medium. The power spectra that need to be estimated from Eq. 3.4 are a 1D and

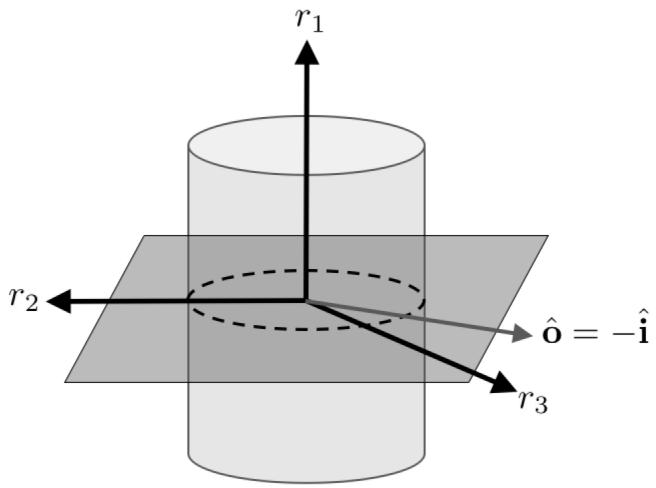

Figure 3.7: Scattering geometry for transverse isotropic medium.

a 2D power spectrum. The required 2D power spectrum can be estimated from a 2D slice and the required 1D power spectrum by examining sequential slices or by making assumptions about the medium.

The transverse isotropic ZM method is useful for tissues such as muscle or nerve, which exhibit cylindrical structure. When conducting 2DZM analysis in this case, the goal would be to cut the tissue in the transverse direction to the cylindrical structures. Using 2DZM analysis of these cross sections would then provide estimates for the 2D power spectrum in Eq. 3.4.

3.4.8 Conclusions

There are two fundamental approaches to analyzing ZMs. In the first approach, the squared modulus of the Fourier transform is used to estimate the power spectrum of a random process. Estimation of the correlation function is not needed in this approach. In the second approach, the correlation function for the random process is estimated first and then used to estimate the power spectrum.

3DZM analysis can be conducted using either of the described approaches. 2DZM analysis of isotropic media can be conducted using the second approach. 2DZM analysis of transverse isotropic media can be conducted using either of the described approaches.

CHAPTER 4

SIMULATIONS

In the first section of this chapter, methods for packing scatterers inside a volume are discussed. Next, the structure function with container was validated using simulations. In the later sections, the 2DZM computational tool was validated using simulations. Each simulation was designed to answer a specific question related to ZM analysis. Practical issues related to ZM analysis include the role of ZM size and regularly spaced slices in estimating correlation coefficient and power spectrum. The simulated media had a known correlation coefficient and power spectrum, and therefore it was possible to study ZM performance by comparing the correlation coefficient and power spectrum estimated using a ZM to a ground truth.

4.1 Scatterer packing

Several methods exist for filling a specified volume with discrete scatterers (e.g., spheres) such that the scatterers do not overlap with each other. Two classes of methods exist for performing this task, including equilibrium methods and non-equilibrium methods [39]. Equilibrium methods sample the scatterer configuration space in a uniform manner, such that the probability distribution for the scatterer configurations is uniform. For non-equilibrium methods, the probability distribution for the scatterer configurations is not uniform and some configurations are preferred over others.

The random sequential absorption algorithm (RSA) is a non-equilibrium method that consists of sequentially attempting to place a scatterer in a specified volume. If the scatterer being placed overlaps with any existing scatterers in the volume, that position is rejected. Otherwise, that position is accepted and the scatterer is placed in the volume. This sequential addition of scatterers repeats until the specified number of scatterers have been placed

in the volume. Scatterers placed using the RSA algorithm are frozen in place once they have been placed and do not diffuse to make room for the placement of other scatterers. For this reason, RSA reaches a saturation limit that is significantly lower than equilibrium methods. For monodisperse hard spheres in 3D, the maximum achievable volume fraction using RSA is approximately 38% [40].

The most commonly used equilibrium method for placing scatterers is the Metropolis algorithm, which is described below [39].

1. An initial configuration of scatterer positions in a specified volume is generated without regard to whether scatterers are overlapping. The energy of the configuration is computed.

2. A scatterer is displaced along each axis by amounts governed by a uniform distribution [-δ, δ], where δ is the maximum step size. The energy of the new configuration is computed. If the new energy is smaller than the old energy, the move is accepted. If the new energy is larger than the old energy, the move is accepted according to an exponential distribution that depends on the energy change.

3. Each scatterer is moved sequentially in this manner, accepting or rejecting the move according to the previous rule.

4. This process is repeated until an equilibrium state is achieved and no scatterers overlap each other.

For the Metropolis algorithm, the maximum achievable volume fraction is approximately 64% in 3D for monodisperse spheres [40]. An example of a cross section from a volume that was filled with spheres using the Metropolis algorithm is in Fig. 4.1.

Two methods for placing non-overlapping scatterers such as spheres were reviewed in this section, including RSA and the Metropolis algorithm. The Metropolis algorithm was used in this work because it is an equilibrium method. Associated with the way that scatterers are placed in a volume is a pair correlation function in the spatial domain and a structure function in the spatial frequency domain. Non-overlapping monodisperse spheres placed using an equilibrium method will be governed by the PY pair correlation function and structure function. If the spheres were placed such that overlap

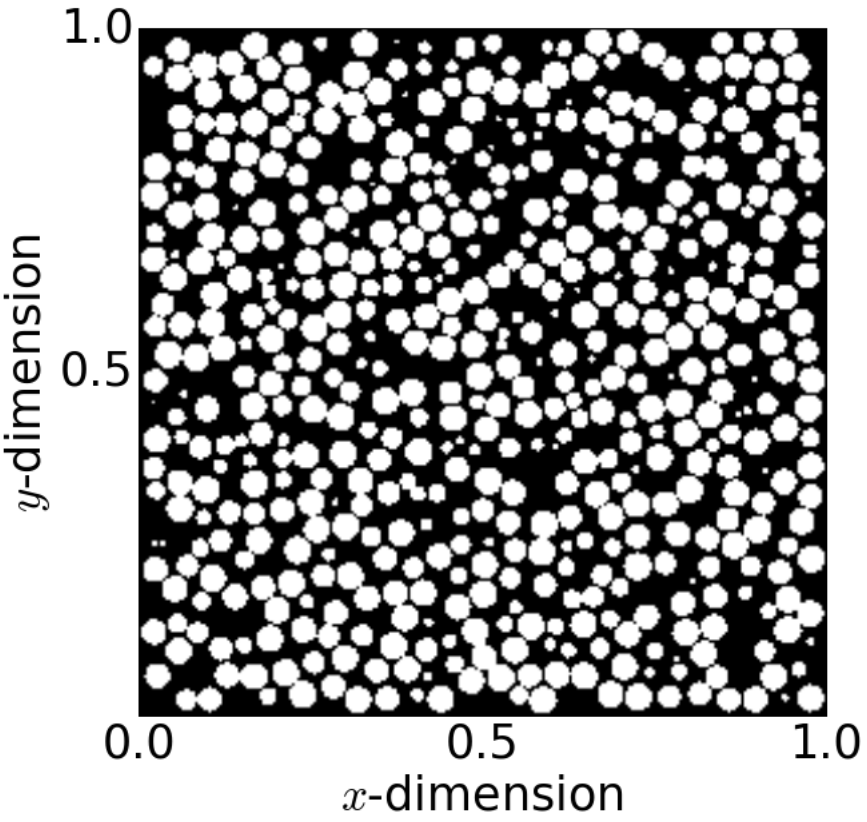

Figure 4.1: Example cross section from a collection of spheres with 45% volume fraction. White indicates a value of one and black indicates a value of zero.

was acceptable, the IP pair correlation function would apply. The Metropolis algorithm will be used in future sections to validate the structure function with container model and to simulate media to demonstrate that the 2DZM method works for dense collections of objects.

4.2 Validation of structure function with container

Simulations were used to test the structure function with container model. Four simulations were used to validate this model, including cube container with IP, sphere container with IP, cube container with non-overlapping spheres, and sphere container with non-overlapping spheres. Once validated using simulations, the model can be used to predict structure function behavior for different model parameters, such as container size, shape, and pair correlation function.

4.2.1 Description of simulations

Cube container and independent positions

The scatterer spacing probability distribution $p(\mathbf{\Delta r})$ in Eq. 2.45 assuming IP scatterers and a cube container having side length $L = 1.0$ was estimated in the following manner. A total of 10^4 scatterer positions inside the cube container were selected randomly and independently. In other words, each coordinate for each scatterer position in 3D space was generated using a continuous uniform random number generator with range [0, 1]. The spacing between each scatterer position and every other scatterer position was computed. Because there were 10^4 scatterer positions, there were a total of $10^4(10^4 - 1)$ scatterer spacings that were computed. Using this collection of scatterer spacings, kernel density estimation was used to estimate the scatterer spacing probability distribution, $p(\mathbf{\Delta r})$. This simulation was repeated ten times and the average of the set of scatterer spacing probability distributions was found. The model of the scatterer spacing probability distribution for this simulation was given by Eq. 2.50, where the IP pair correlation function $g(\Delta r) = 1$ and the cube container autocorrelation function $W_{cube}(\mathbf{\Delta r}) = \text{tri}\left(\frac{\Delta x}{L}\right)\text{tri}\left(\frac{\Delta y}{L}\right)\text{tri}\left(\frac{\Delta z}{L}\right)$ were used.

Sphere container and independent positions

The described process for simulating the scatterer spacing probability distribution $p(\mathbf{\Delta r})$ assuming IP and a cube container was repeated for a sphere container with diameter $L = 1.0$. A total of 10^4 scatterer positions inside the sphere container were selected randomly and independently. Rejection sampling was used to sample scatterer positions inside the sphere container. Similar to the cube container simulation, each coordinate for each scatterer position in 3D space was generated using a continuous uniform random number generator with range [0, 1]. The scatterer position was discarded if it was outside of the sphere container and retained if it was inside the sphere container. Using the collection of scatterer spacings, kernel density estimation was used to estimate the scatterer spacing probability distribution, $p(\mathbf{\Delta r})$. This simulation was repeated ten times and the collection of scatterer spacing probability distributions were averaged. The model of the scatterer spacing probability distribution for this simulation was given by Eq. 2.50, where the IP pair correlation function $g(\Delta r) = 1$ and the sphere container autocorrelation function $W_{sphere}(\Delta r) = 1 - \frac{3\Delta r}{4(L/2)} + \frac{\Delta r^3}{16(L/2)^3}, \quad 0 \leq \Delta r \leq L$, were used.

Cube container and non-overlapping spheres

The scatterer spacing probability distribution $p(\mathbf{\Delta r})$ in Eq. 2.45 for a cube container with side length $L = 1.0$ and using the PY structure function, i.e., non-overlapping spheres, was estimated in the following manner. Spherical scatterers having radius $a = 0.05$ were placed in a cube container using the Metropolis algorithm [39]. A total of 573 spheres were placed in the cube container for a volume fraction of 30%. The simulation produced a set of scatterer positions associated with each of the spherical scatterers in the volume. The spacing between each scatterer position and every other scatterer position was computed. Because there were 573 scatterer positions, a total of $573(573 - 1) = 327,756$ scatterer spacings were computed. Using the collection of scatterer spacings, kernel density estimation was used to estimate the scatterer spacing probability distribution, $p(\mathbf{\Delta r})$. This simulation was repeated 1000 times and the collection of scatterer spacing probability distributions were averaged. The model of the scatterer spacing probability

distribution for this simulation was given by Eq. 2.50, where the PY pair correlation function shown in Fig. 2.4 (c) and the cube container autocorrelation function were used.

Sphere container and non-overlapping spheres

The described process for simulating the scatterer spacing probability distribution $p(\mathbf{\Delta r})$ assuming the PY structure function and a cube container was repeated for a sphere container with diameter $L = 1.0$. In this case, spherical scatterers were simulated inside a cube container with side length $L = 1.0$. Once the Metropolis algorithm stopped, the scatterer positions outside a sphere having diameter $L = 1.0$ were discarded. Using the collection of scatterer spacings, kernel density estimation was used to estimate the scatterer spacing probability distribution, $p(\mathbf{\Delta r})$. This simulation was repeated 1000 times and the collection of scatterer spacing probability distributions were averaged. The model of the scatterer spacing probability distribution for this simulation was given by Eq. 2.50, where the PY pair correlation function shown in Fig. 2.4 (c) and the sphere container autocorrelation function were used.

4.2.2 Simulation results

Cross sectional views of the scatterer spacing distribution $p(\mathbf{\Delta r})$ for IP assuming a cube container for model and simulation are in Figs. 4.2 (a) and (c), respectively. When using a sphere container, the resulting cross sectional views for model and simulation are in Figs. 4.2 (b) and (d), respectively. The error between the modeled and simulated distributions is

$$\text{error} = p_{model}(\mathbf{\Delta r}) - p_{simulation}(\mathbf{\Delta r}). \tag{4.1}$$

The error between the model and simulation scatterer spacing probability distribution is in Fig. 4.3. The root-mean-square error (RMSE) was found between the model and simulation probability distributions. The error in the simulated scatterer spacing probability distribution depends on the number of scatterer spacings used to estimate the scatterer spacing probability distribution. Therefore, the RMSE is a function of the number of scatterer

spacings included in the analysis. If the modeled probability distribution is correct, the simulated probability distribution RMSE should converge to zero as the number of scatterer spacings in the analysis increases. The RMSE curves for the IP spacing probability distributions are in Fig. 4.4.

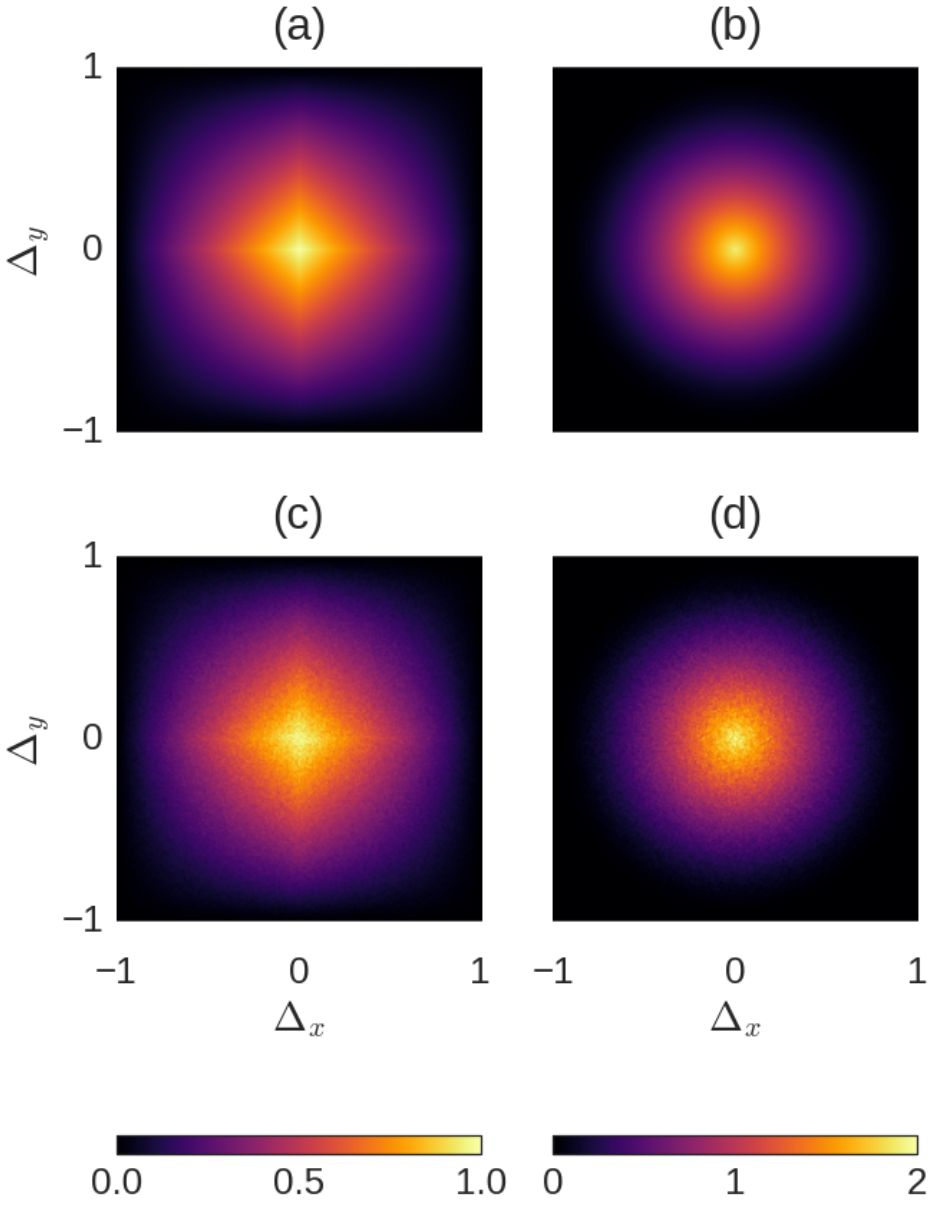

Figure 4.2: Example cross sections from the scatterer spacing probability distribution assuming IP. Modeled probability distributions for the (a) cube and (b) sphere containers. Estimated probability distributions for the (c) cube and (d) sphere containers. The cube container had side length $L = 1.0$ and the sphere container had diameter $L = 1.0$.

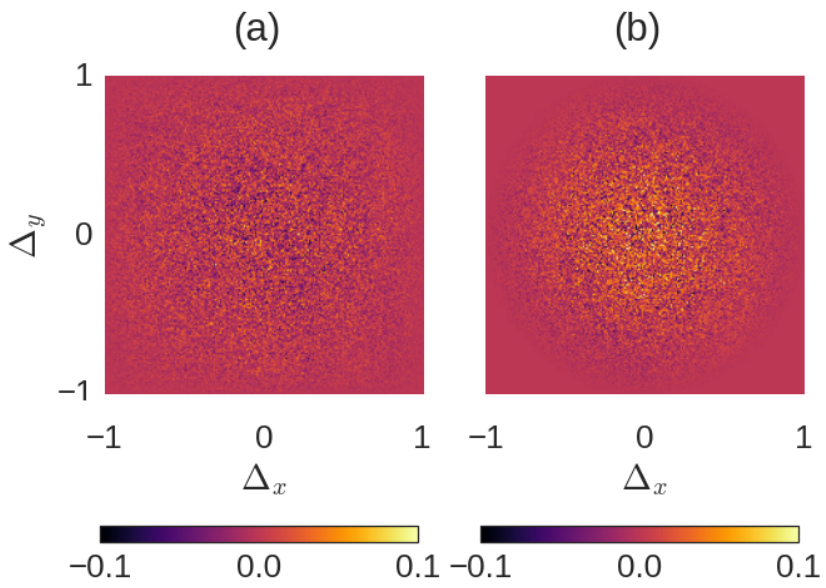

Figure 4.3: Error between modeled and simulated scatterer spacing probability distributions for (a) cube and (b) spherical containers assuming the IP pair correlation function.

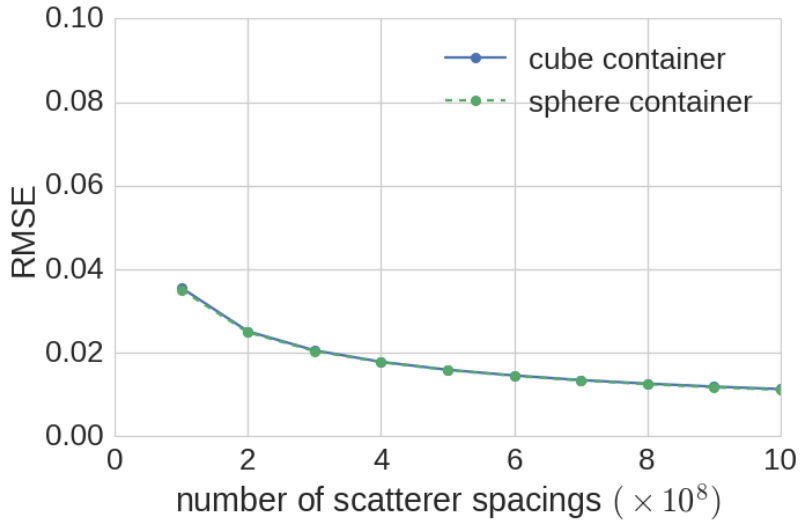

Figure 4.4: RMSE between modeled and simulated scatterer spacing probability distributions for cube and spherical containers assuming the IP pair correlation function. The RMSE is given as a function of the number of scatterer spacings included in the simulation analysis. The number of scatterer spacings can be increased by including more spheres in the simulation or by averaging results from independent simulations.

Examples of cross sections of the scatterer spacing distribution $p(\mathbf{\Delta r})$ for the PY pair correlation function assuming a cube container for the model and simulation are in Figs. 4.5 (a) and (c), respectively. When using a sphere container, resulting example cross sections for model and simulation are in Figs. 4.2 (b) and (d), respectively. The error defined in Eq. 4.1 between the model and simulation scatterer spacing probability distribution is in Fig. 4.6. The RMSE between model and simulation is shown as a function of the number of scatterer spacings included in the simulation in Fig. 4.7.

4.2.3 Discussion

For the IP scatterer spacing probability distribution, visual inspection between the model and simulation results in Fig. 4.2 showed good agreement for the cube and sphere containers. The error between simulation and model presented in Fig. 4.3 does not show a systematic source of error. The error between model and simulation decreased as a function of the distance from the origin. The scatterer spacing distribution also decreases in this manner, so the error appears to be random noise that is proportional to the magnitude of the probability distribution itself. The RMSE curves for the IP probability distributions, shown in Fig. 4.4, suggest that the simulation probability distribution was converging to the model probability distribution for both cube and sphere containers. These results suggest that for the case of IP, the suggested model probability distribution and associated structure function with container effect models are valid.

For the PY pair correlation function scatterer spacing probability distributions, visual inspection between the model and simulation in Fig. 4.5 shows good agreement for the cube and sphere containers. However, there were some discrepancies between model and simulation that appeared when examining the error between model and simulation as shown in Fig. 4.6. For the case of a cube container, discrepancies existed on-axis where the model probability distribution had magnitude value below the simulation probability distribution (i.e., a negative error value). In addition, for both cube and sphere containers, discrepancies existed between model and simulation near the scatterer spacing radial value $\Delta r = 2a$, where a is the radius of the spherical scatterers. These errors indicated that the model probability

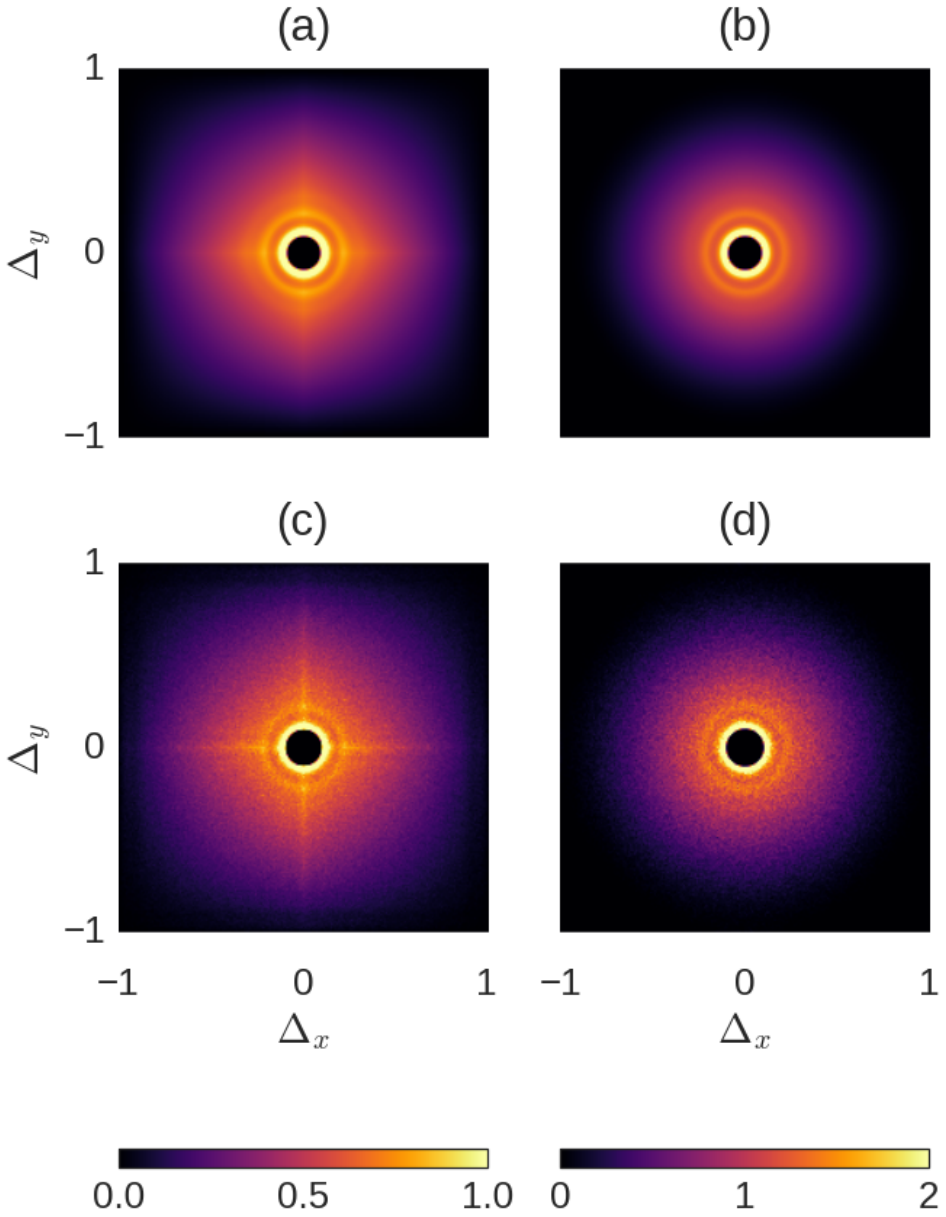

Figure 4.5: Example cross sections from the scatterer spacing probability distribution assuming IP. Modeled probability distributions for the (a) cube and (b) sphere containers. Estimated probability distributions for the (c) cube and (d) sphere containers. The cube container had side length $L = 1.0$ and the sphere container had diameter $L = 1.0$. The spherical scattering objects had radius $a = 0.05$.

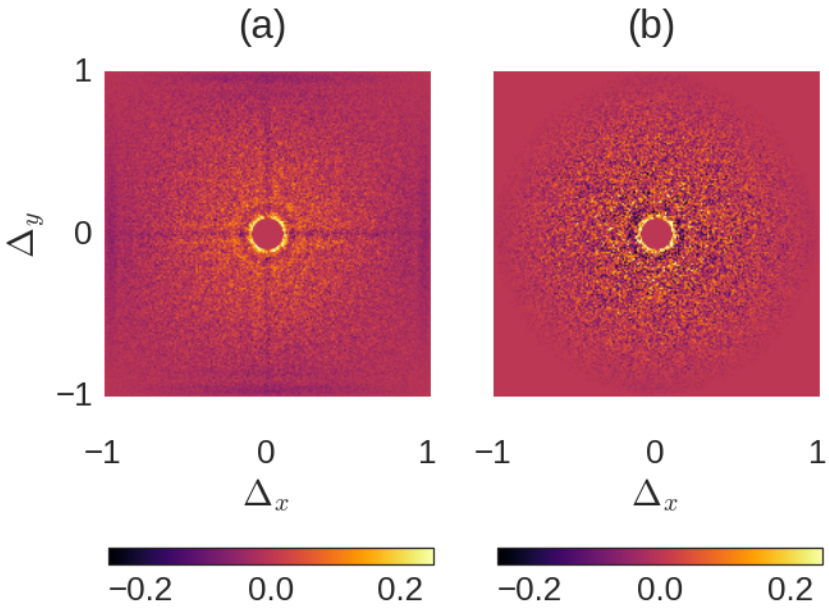

Figure 4.6: Error between modeled and simulated scatterer spacing probability distributions for (a) cube and (b) spherical containers assuming the PY pair correlation function.

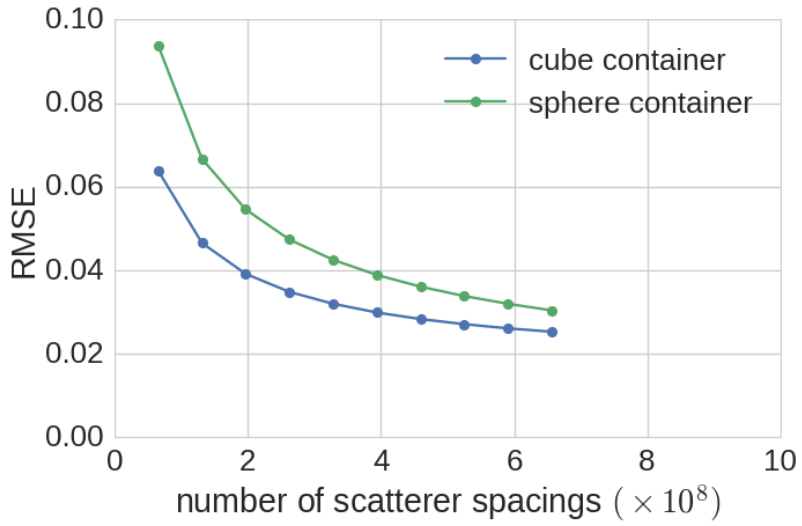

Figure 4.7: RMSE between modeled and simulated scatterer spacing probability distributions for cube and spherical containers assuming the PY pair correlation function. The RMSE is given as a function of the number of scatterer spacings included in the simulation analysis.

distribution had magnitude value greater than the simulation probability distribution (a positive error value). The RMSE curves for the PY correlation function probability distributions, shown in Fig. 4.7, shows that the simulation probability distribution was not converging to the model probability distribution for both cube and sphere containers. However, the error between the model and simulation probability distributions was small. The PY pair correlation function is an approximation for the pair correlation function produced by using an equilibrium method to fill a volume with non-overlapping spheres. Therefore, the error between the model and simulation may be due to this approximation. The proposed model still offers a good approximation for the actual probability distribution produced for a volume containing non-overlapping spheres.

When modeling BSCs from dense media, it is important to account for the structure function; otherwise, error will be introduced into the parameter estimates. However, it should also be noted that when using the PY structure function to model BSCs, the fact that the PY structure function is an approximation also introduces errors in the parameter estimates.

4.2.4 Conclusion

The simulations in this section serve as validation for the structure function with container effects. Excellent agreement (RMSE: 1%) was observed between model and simulation scatterer spacing distribution for the case of IP and cube and sphere containers. Good agreement (RMSE: 3%) between model and simulation was observed in the case of the PY pair correlation function. This model could be used to study the effect of a container on ZMs or the effect of a focal region on BSC estimation.

4.3 2DZM simulations of sparse isotropic media

The primary goal of the simulation studies in this section was to verify that 2DZMs can be used to estimate correlation coefficients and power spectra with low error for sparse collections of objects. The correlation coefficient and 3D power spectrum of the media studied in this section have simple shapes as shown in Fig. 4.8 and provide an excellent starting point for

demonstrating that the 2DZM method works. Because the simulated ZMs had known correlation coefficients and power spectra, they could be used to assess error when using 2DZMs to estimate these quantities. The studies were also designed to offer practical guidance for 2DZM analysis, including ZM size, spacing, and section thickness.

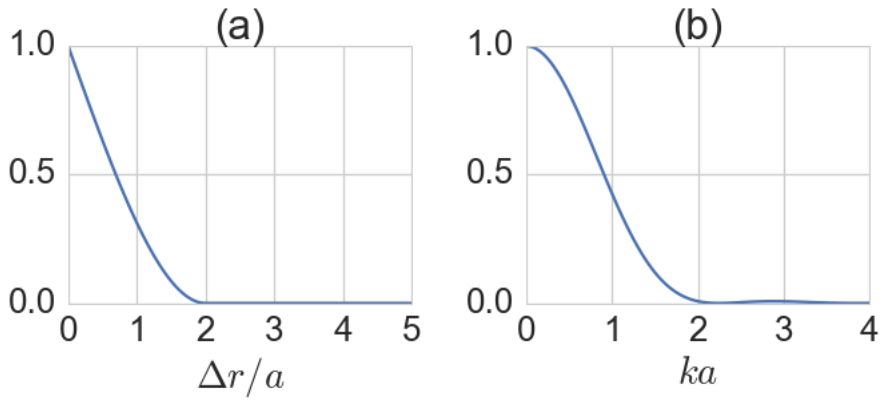

Figure 4.8: (a) Correlation coefficient and (b) power spectrum for a collection of sparse monodisperse spheres.

For a typical tissue, each histological section contains many scattering object cross sections. These objects could be cells, ductal structures, nerve bundles, muscle fibers, etc. The error of the correlation coefficient and power spectral estimates is related to the number of object cross sections included in the analysis. The error of these estimates will decrease as the number of object cross sections included in the analysis increases and increase as the number of object cross sections decreases. Therefore, 2DZM size should be made as large as possible. However, the tissue of interest may not be stationary and it may be desirable to spatially localize the analyzed tissue properties. Therefore, it also desirable to make the 2DZM size as small as possible. Simulations can be used to determine how many object cross sections need to be included in a 2DZM analysis to obtain tissue correlation coefficient and power spectral results having low error.

Two methods were explored for reducing error when using 2DZMs to estimate correlation coefficients and power spectra representing 3D volumes. The first method was to increase the physical size of the 2DZM. Increasing the physical size of the 2DZM increases the number of object cross sections

included in the ZM analysis, leading to power spectral estimates with reduced error assuming that the properties of the objects in the cross section are uniform.

The second method for reducing error was to increase the number of 2DZMs that were extracted from the volume. Each 2DZM was used to independently estimate the correlation coefficient and the resulting correlation coefficients were averaged before being used to estimate the power spectrum. When sectioning a tissue for 3DZM analysis, the slices are successively cut from the tissue and have regular spacings, suggesting that slices extracted at regular spacings be studied for 2DZM analysis. Furthermore, analyzing 2DZMs that intersect different sets of objects as shown in Fig. 4.9 (a) is equivalent to increasing the size of the 2DZM. Averaging correlation coefficients from slices that intersect different objects discards information about the positions of objects relative to each other. For regularly spaced slices having separation less than the object diameter, information about relative object positions will be present in the estimated correlation coefficients. Therefore, the regularly spaced slices were extracted from a layer of the volume that had thickness on the order of the size of the scattering objects as shown in Fig. 4.9 (b). Increasing the regularly spaced slice density in this manner is different from increasing the physical size of the 2DZM, because adjacent 2DZMs have similar cross sections.

4.3.1 Description of simulations

For the first set of simulations, two-phase media were constructed by placing discrete scatterers (i.e., spheres, ellipsoids) into volumes. The simulated volumes were two-phase media; i.e., the background had a value of zero and the inside of the object had a value of one. The collection of spheres in Fig. 4.10 (a) and the collection of randomly oriented ellipsoids in Fig. 4.10 (b) are examples of isotropic media. The sparse two-phase media simulate a biological medium filled with one scattering structure (e.g., cell, cell nucleus, duct, nerve bundle, muscle fiber, etc.) and when the scattering structures were sparsely located.

The centers of the objects were sparsely located and had a separation distance of at least twice the largest diameter of the object. The purpose of

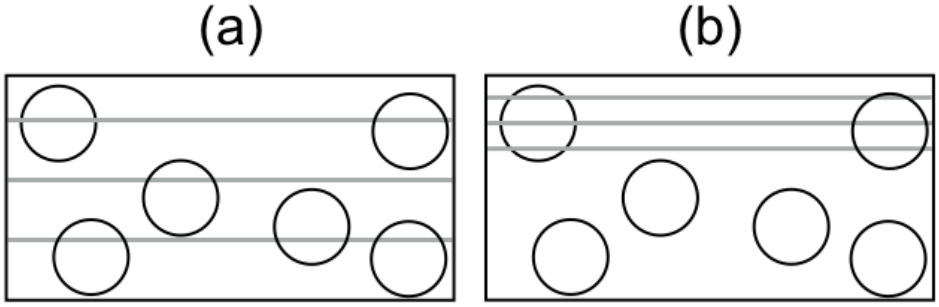

Figure 4.9: Two-dimensional side view of several collections of spheres. Spheres are depicted as black circles and slices as gray lines. (a) Three regularly spaced slices having spacing greater than the sphere diameter causing the object cross sections in adjacent slices to be unrelated. (b) Three regularly spaced slices having spacing less than the sphere diameter causing the object cross sections in adjacent slices to be related.

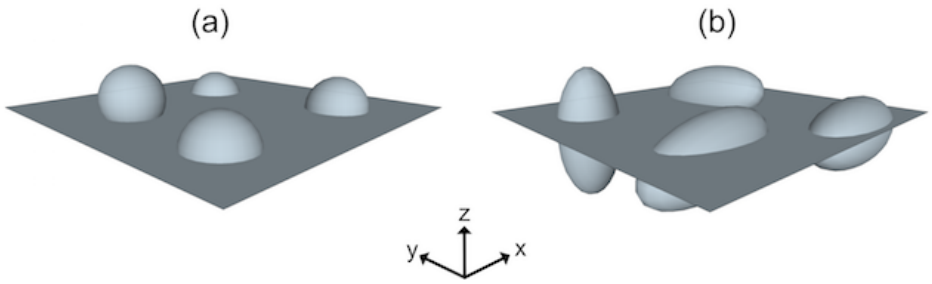

Figure 4.10: (a) Collection of randomly located spheres and (b) collection of randomly located and randomly oriented ellipsoids in isotropic media.

this separation criterion was that the correlation coefficient in the lag range $0 \leq \Delta r \leq 2a$, where a was the largest radius for the object, consisted of the sum of the correlation coefficients for each individual object. In other words, correlation coefficient values resulting from the interaction between different objects only existed at lag ranges greater than $2a$. Therefore, it was possible to set the correlation coefficient to 0.0 for the range $\Delta r > 2a$ to eliminate interaction effects between the objects. The separation criteria for monodisperse spheres are in Fig. 4.11.

These simulation studies were used to determine the effectiveness of the two described methods for reducing the error in 2DZM correlation coefficient and power spectrum estimates. Volumes containing different numbers of objects were simulated. To study the effect of physical 2DZM size on power spectral estimates, the size of the simulated 2DZM was expanded to increase the number of objects included in the analysis. Initially, a single slice was extracted from the volume. To study the effect of regularly spaced slice density, the analysis was repeated using different numbers of regularly spaced slices that were drawn from a layer in the volume having the same thickness as the diameter of the objects. Therefore, each simulation volume was generated by specifying an average number of objects per slice (physical 2DZM size) and an average number of regularly spaced slices per object (regularly spaced slice density). The number of objects per slice was varied in the range $\{1, 2, ..., 50\}$ and the number of regularly spaced slices per object was varied in the range $\{1, 3, 5\}$. For each 2DZM size and regularly spaced slice density combination, a total of 50 simulation volumes were generated to produce 50 correlation coefficient and power spectral estimates.

For this type of medium, the correlation coefficient and power spectra could be found for each individual scatterer and then averaged to find the correlation coefficient and power spectral estimates for the collection. Processing the correlation coefficient and power spectra in this way eliminates the effects of the object locations (i.e., structure function and container effects). The performance of the 2DZM could then be studied based on the number of objects included in the analysis without regard to the effects of the object spatial locations. Therefore, any discrepancy between correlation coefficient and power spectrum and its respective theoretical curve would be due to the 2DZM processing method and not to scattering object interaction

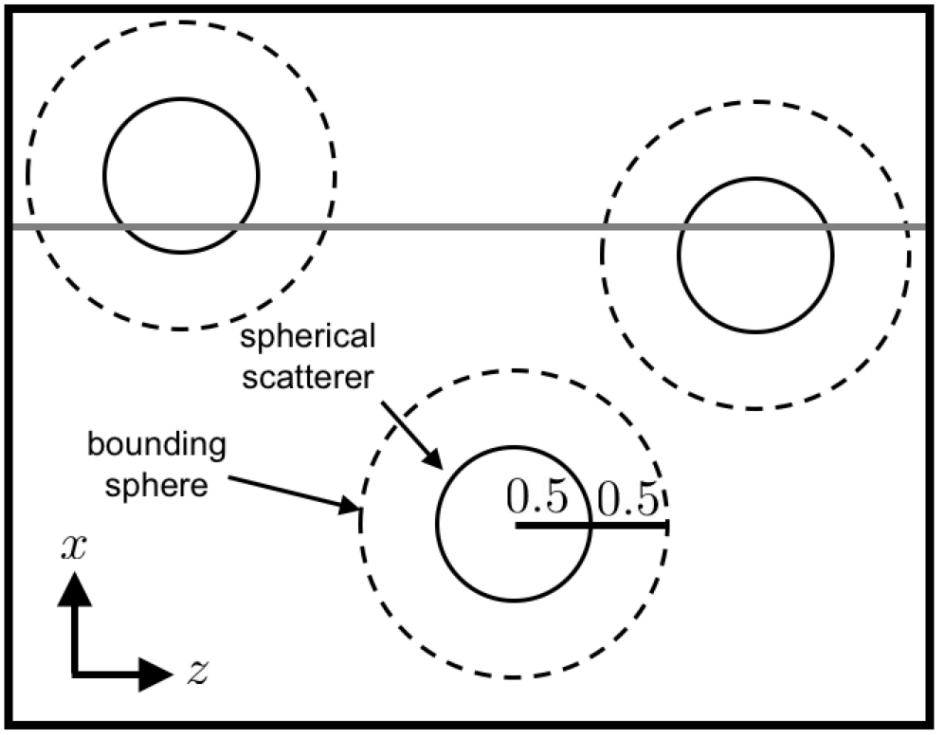

Figure 4.11: Illustration of the separation criteria for collections of sparse monodisperse spheres. The black circles represent the spherical scatterers with radius 0.5. The dashed circles are bounding spheres for the spherical scatterers and had radius 1.0. The bounding spheres for the spherical scatterers were not allowed to overlap so that the minimum separation distance between the sphere centers was 2.0. The gray line represents the 2DZM extracted from the volume.

effects.

Collections of monodisperse spheres having radius 0.5 were simulated as shown in Fig. 4.11. A correlation coefficient was estimated for each 2DZM and then radially averaged to form a 1D function of spatial lag and used in the numerical evaluation of Eq. 2.12. In the case of multiple 2DZMs, a correlation coefficient was estimated for each 2DZM and the correlation coefficients were averaged to form a single 2D correlation coefficient before radial averaging. Performance was quantified using the RMSE between the simulation estimated curves and the theoretical curves.

Simulations of monodisperse spheres are a standard example when exploring new methods for studying acoustic scattering. However, real tissues are more complex than monodisperse spheres, so it is important to examine the behavior of 2DZMs when analyzing more complex media. Collections of randomly oriented ellipsoids having radii 0.5, 0.4, and 0.3 were simulated as shown in Fig. 4.12. The correlation coefficient and power spectrum were processed in the same way as for the sphere collection simulations. Performance was quantified using the RMSE between the simulation estimated curves and the theoretical curves. The correlation coefficient for a collection of randomly oriented and monodisperse ellipsoids is a linear combination of spherical correlation coefficients

$$b_{ellipsoid}(\Delta r) = \int_0^{2\pi} \int_0^{\pi} a_{\theta,\phi}^3 b_{sphere}(\Delta r, a_{\theta,\phi}) \mathrm{d}\phi \mathrm{d}\theta \tag{4.2}$$

where $b_{sphere}(\Delta r, a)$ is the correlation coefficient for a sphere with size a, $a_{\theta,\phi}$ is the radius of the ellipsoid for the given spherical coordinate angles, and $b_{ellipsoid}(\Delta r)$ is the correlation coefficient for the collection of randomly oriented ellipsoids. The power spectrum is found by taking the Fourier transform of the correlation coefficient in Eq. 4.2. The primary goal of these simulations was to study the performance of the 2DZM method for an isotropic medium having scatterers with non-uniform shape.

In addition to having non-spherical shape, the scatterers in real tissues often have varying sizes. Therefore, collections of polydisperse spheres having radii governed by a uniform distribution with minimum of 0.4 and maximum of 0.5 were simulated as shown in Fig. 4.13. The correlation coefficient and power spectrum were processed in the same way as for the sphere collection

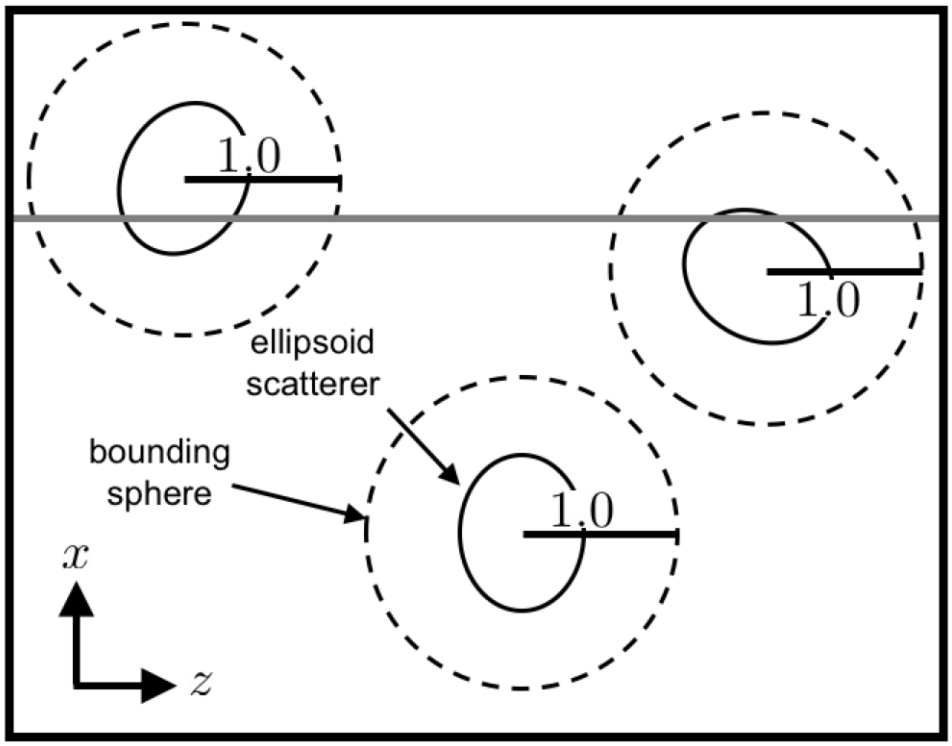

Figure 4.12: Illustration of the separation criteria for collections of sparse monodisperse ellipsoids. The black circles represent the ellipsoidal scatterers. Notice how the ellipsoids are not aligned in the same direction. The ellipsoids had radii (0.3, 0.4, 0.5). The dashed circles are bounding spheres for the ellipsoidal scatterers and had radius 1.0 (twice the maximum ellipsoidal scatterer radius). The bounding spheres were not allowed to overlap so that the minimum separation distance between the ellipsoid centers was 2.0. The gray line represents a 2DZM extracted from the volume.

simulations. Performance was quantified by comparing the theoretical power spectrum for a collection of polydisperse spheres with the 2DZM power spectral estimates [22]. The correlation coefficient for a collection of polydisperse spheres, i.e., each scatterer has the same shape but different size, is a linear combination of spherical correlation coefficients

$$b_{pd-spheres}(\Delta r) = \int a^3 p(a) b_{sphere}(\Delta r, a) da \tag{4.3}$$

where $b_{sphere}(\Delta r, a)$ is the correlation coefficient for a sphere with size a, $p(a)$ is the probability distribution governing sphere sizes, the integration is over the support of this probability distribution, and $b_{pd-spheres}(\Delta r)$ is the correlation coefficient for the polydisperse collection of spheres. The power spectrum for a collection of polydisperse spheres is found by taking the Fourier transform of the correlation coefficient in Eq. 4.3. The primary goal of these simulations was to study the performance of the 2DZM method for an isotropic medium having scatterers with non-uniform shape.

When creating histological slices from a tissue, the slides have finite thickness and this thickness affects the results of the ZM analysis. In order to study the effect of ZM slice thickness on the processing of 2DZMs, the simulations were repeated using a finite slice thicknesses of 10% of the maximum diameter of the scatterer (i.e., 0.05 in all cases). The cross section was produced by extracting a 3DZM having y- and z-dimensions of the 2DZM and x-dimension equal to the slice thickness. Next, the 3DZM was projected to form a 2DZM by taking the maximum value along the x-axis. In this way, the largest radius contained in the sphere cross section was obtained. After creating 2DZMs, processing proceeded the same as with the normal sphere collection simulations. These thickness simulations were studied for monodisperse and polydisperse spheres.

4.3.2 Simulation results

Monodisperse spheres

Figures 4.14 and 4.15 present examples of estimated correlation coefficients and power spectra for different configurations of object cross sections per

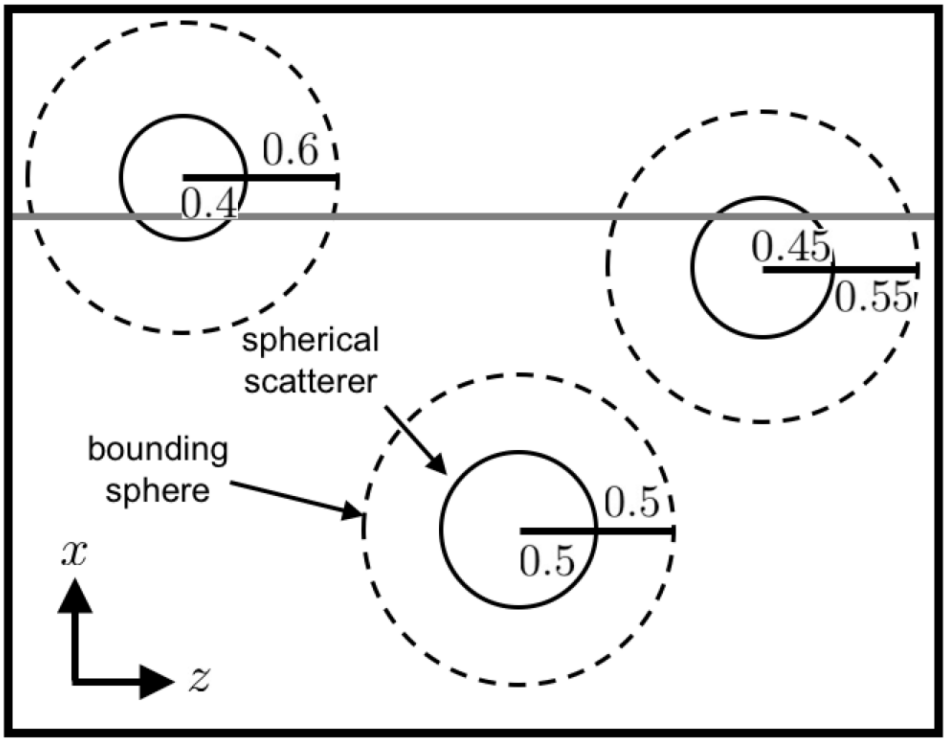

Figure 4.13: Illustration of the separation criteria for collections of sparse polydisperse spheres. The black circles represent the spherical scatterers. The spherical radii were governed by a uniform distribution with minimum of 0.4 and maximum of 0.5. The dashed circles are bounding spheres for the spherical scatterers and had radius 1.0 (twice the maximum spherical scatterer radius). The bounding spheres for the spherical scatterers were not allowed to overlap so that the minimum separation distance between the sphere centers was 2.0. The gray line represents a 2DZM extracted from the volume.

slice and number of regularly spaced slices for collections of monodisperse spheres. The power spectra were estimated using 2DZM method #1. A total of 50 simulations for each 2DZM size and density configuration were used. Figures 4.16 and 4.17 present examples of estimated correlation coefficients and power spectra for different configurations of object cross sections per slice and number of regularly spaced slices for collections of monodisperse spheres, except that the slice thickness was set to 10% of the sphere diameter. Figure 4.18 shows the RMSE for the estimated correlation coefficient as the number of spheres included in the analysis was increased, i.e., the size of the 2DZM was increased. Figure 4.18 shows the RMSE for the estimated power spectrum as the number of spheres included in the analysis was increased.

For the monodisperse sphere simulations, the results in Figs. 4.14 and 4.15 show that the 2DZM correlation coefficient and power spectral estimates converged to their respective theoretical forms as the number of sphere cross sections included in the analysis was increased by increasing either the number of regularly spaced slices or the number of spheres. Figure 4.14 (a) and 4.15 (a) clearly demonstrate the need for the present simulation. A collection of randomly located spheres is an isotropic random process, so it should be possible to estimate the correlation coefficient and power spectrum from this random process using 2DZMs. However, the correlation coefficient and power spectrum estimates based on one slice from a single sphere showed significant error. In contrast, Fig. 4.14 (i) and 4.15 (i) demonstrate that the correlation coefficient and power spectrum can be estimated using many slices from a large collection of spheres. Analysis of Figs. 4.14 and 4.15 suggests that a sufficient number of slices and/or scattering objects need to be included in a 2DZM analysis to estimate the correlation coefficient and power spectrum with low error. The goal of these simulations was to relate such 2DZM analysis parameters to the error in the estimated correlation coefficient and power spectrum.

Visual inspection of Figs. 4.14 and 4.15 indicates that the correlation coefficient estimates converged more quickly to theory than did the power spectral estimates. This result was also visible from Figs. 4.18 (a) and 4.19 (a), as the falloff in the RMSE curves was much steeper for the correlation coefficients than for the power spectra. The RMSE curves for the correlation coefficient estimates exhibited a region of rapid decline followed by a region of

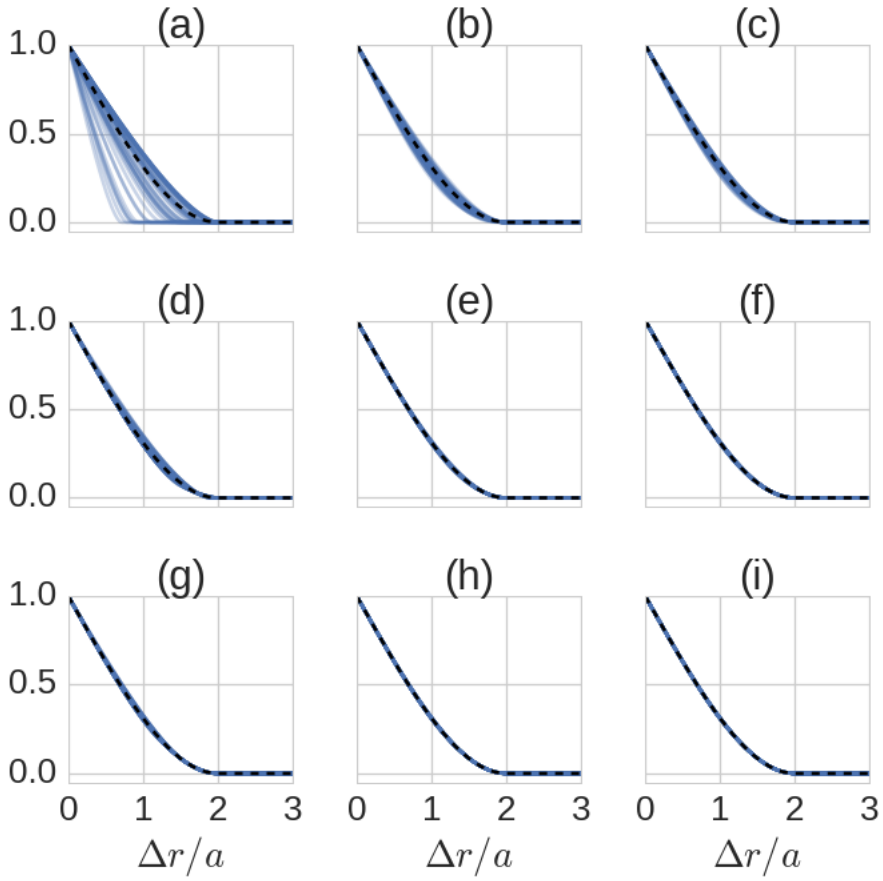

Figure 4.14: Estimated correlation coefficients for monodisperse spheres when using (a, b, c) one regularly spaced slice, (d, e, f) three regularly spaced slices, (g, h, i) five regularly spaced slices, (a, d, g) 1 object cross section per slice, (b, e, h) 15 object cross sections per slice, and (c, f, i) 30 object cross sections per slice. The dashed line represents the theoretical correlation coefficient. Each solid line represents one of 50 simulations.

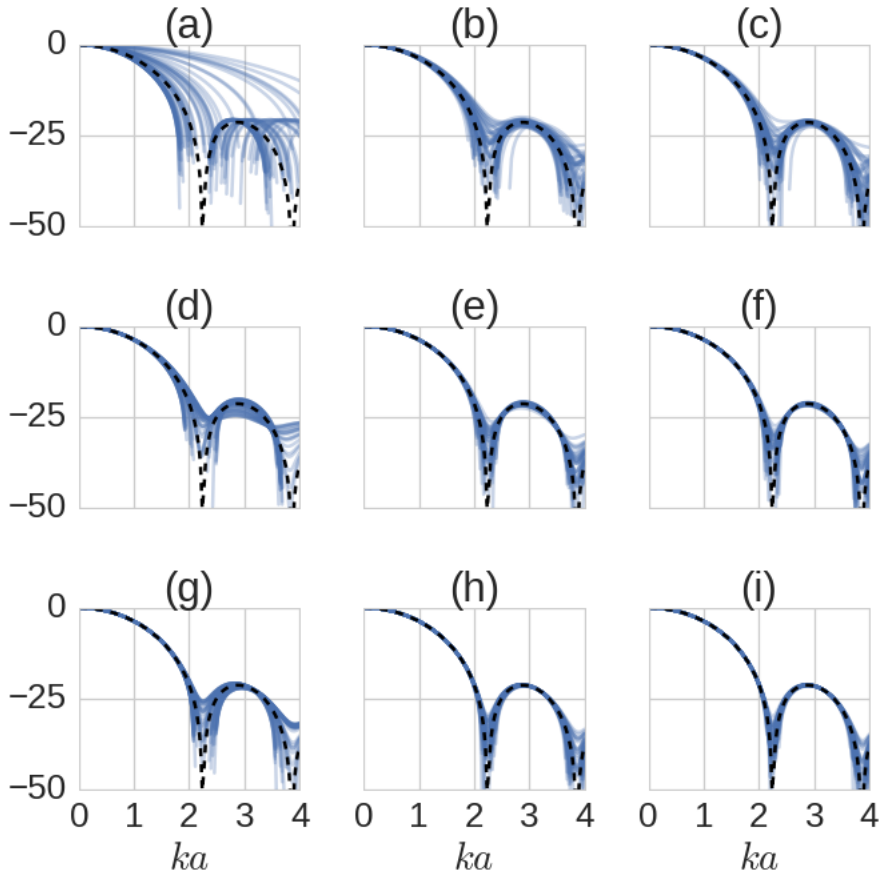

Figure 4.15: Estimated power spectra for monodisperse spheres when using (a, b, c) one regularly spaced slice, (d, e, f) three regularly spaced slices, (g, h, i) five regularly spaced slices, (a, d, g) 1 object cross section per slice, (b, e, h) 15 object cross sections per slice, and (c, f, i) 30 object cross sections per slice. The dashed line represents the theoretical power spectrum. Each solid line represents one of 50 simulations.

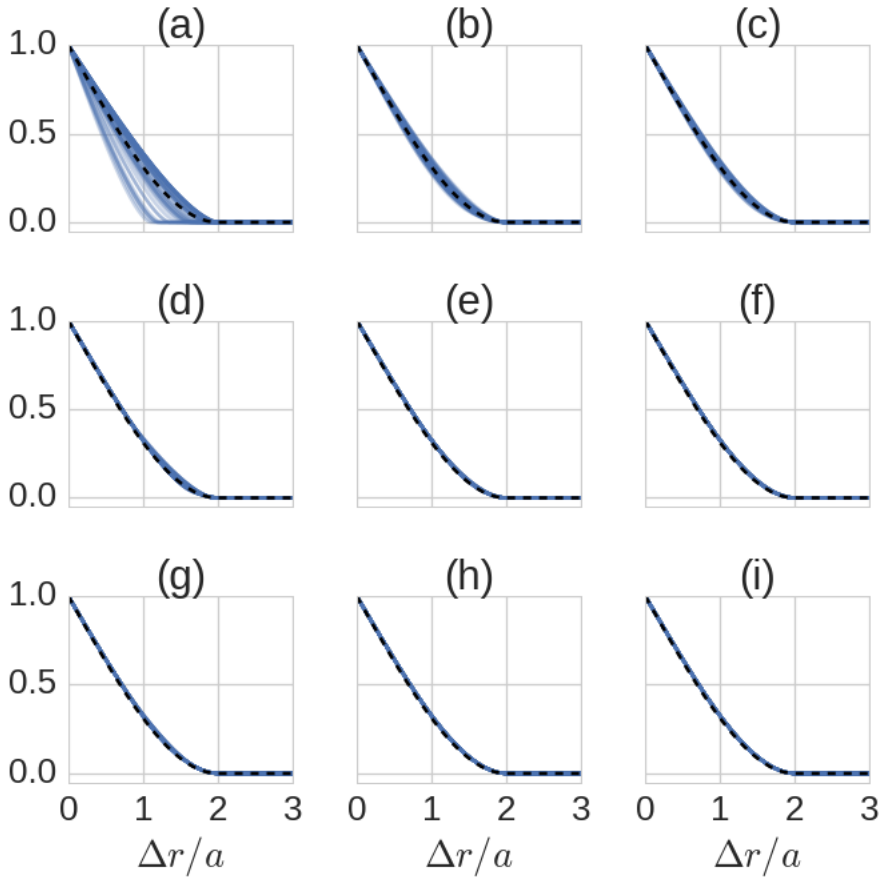

Figure 4.16: Estimated correlation coefficients for monodisperse spheres when using a slice thickness of 10% of the sphere diameter and when using (a, b, c) one regularly spaced slice, (d, e, f) three regularly spaced slices, (g, h, i) five regularly spaced slices, (a, d, g) 1 object cross section per slice, (b, e, h) 15 object cross sections per slice, and (c, f, i) 30 object cross sections per slice. The dashed line represents the theoretical correlation coefficient. Each solid line represents one of 50 simulations.

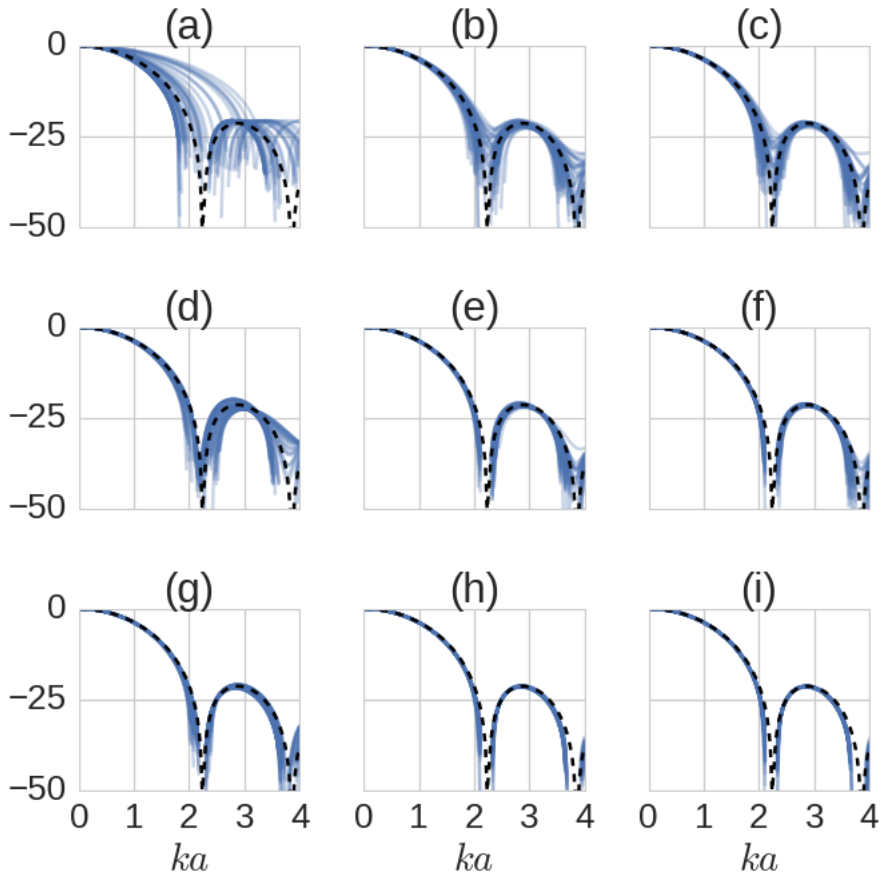

Figure 4.17: Estimated power spectra for monodisperse spheres when using a slice thickness of 10% of the sphere diameter. Presentation is the same as Fig. 4.16.

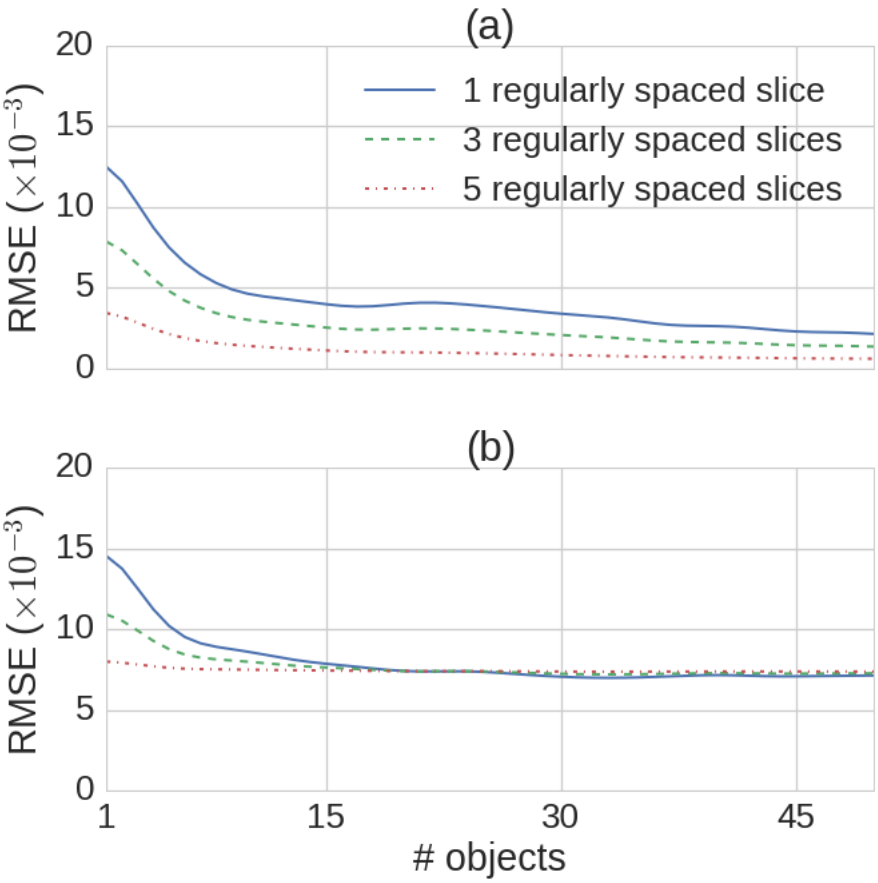

Figure 4.18: RMSE for estimated correlation coefficients for monodisperse spheres. Using a slice thickness of (a) 0% (i.e., a perfect cross-section through the 3DZM) and (b) 10% of object diameter.

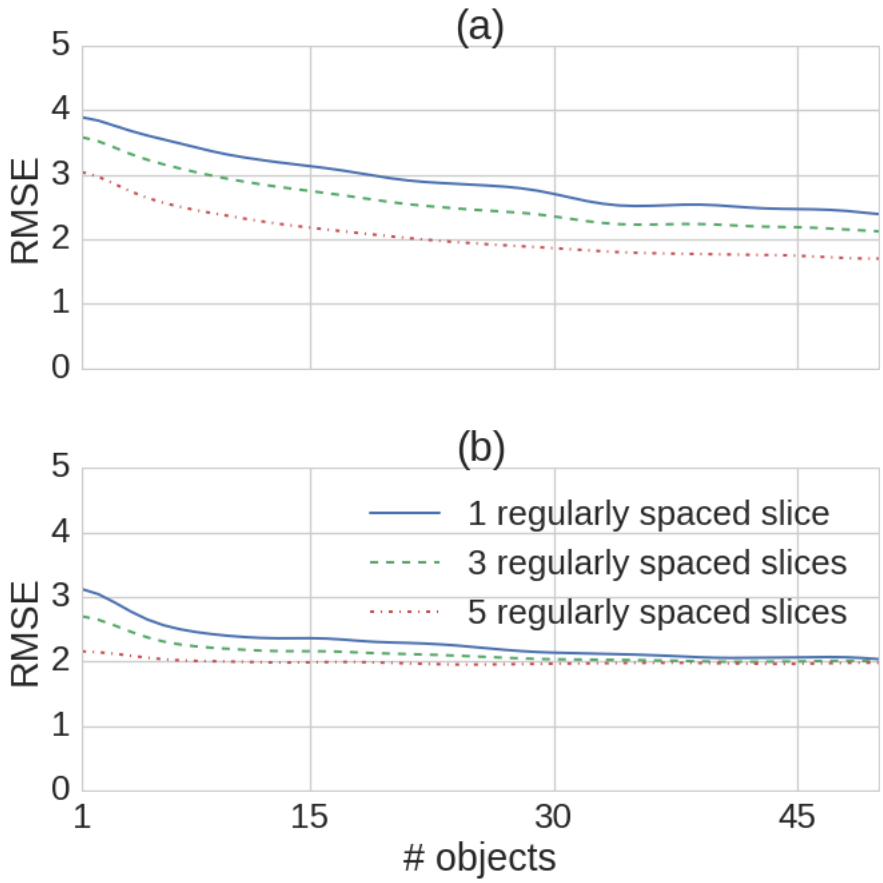

Figure 4.19: RMSE for estimated power spectra for monodisperse spheres. Using a slice thickness of (a) 0% (i.e., a perfect cross-section through the 3DZM) and (b) 10% of object diameter.

slow decline. The division in 2DZM size between the region of rapid and slow decline for the correlation coefficient was approximately 15 spheres. Only marginal decreases in RMSE were observed by adding additional spheres. The described region of rapid decline was not as pronounced for the power spectrum as it was for the correlation coefficient. However, the RMSE in the power spectral estimates showed appreciable decay by including up to 30 spheres in the analysis. Only marginal reductions in RMSE error were observed by increasing the 2DZM size further. A significant source of error in the power spectral estimates shown in Fig. 4.15 was the nulls in the theoretical power spectrum. These nulls could be the reason why the 2DZM needed to be larger when estimating the power spectrum compared to the correlation coefficient.

The RMSE curves for the correlation coefficient in Fig. 4.18 (a) indicated that significant reductions in error were possible by increasing the number of regularly spaced slices included in the analysis. For example, it was possible to reduce the RMSE in the correlation coefficient estimate by approximately 40% when using three regularly spaced slices instead of one slice from a single sphere. To achieve the same error reduction when using one regularly spaced slice, a total of six spheres had to be included in the analysis. It should be noted that RMSE reduction from increasing the number of regularly spaced slices decreased as the number of spheres in the analysis was increased. This result suggests that the use of a small 2DZM size could be compensated for by increasing the number of regularly spaced slices used in the analysis. A related conclusion was that the use of regularly spaced slices has diminishing returns as the physical size of the 2DZM size is increased.

The effect on the correlation coefficient and power spectral estimates of using a slice thickness of 10% of the object diameter is shown in Figs. 4.16 and 4.17. For the correlation coefficient, the effect of the finite slice thickness was that the correlation coefficient values were slightly larger than the expected theoretical values. In other words, the correlation coefficients bulged in the vertical direction relative to the theoretical correlation coefficient. However, the spatial extent of the correlation coefficient did not change, i.e., the first value when the correlation coefficient was zero was the same using 0% slice thickness and 10% slice thickness. Increasing the slice thickness caused the power spectrum nulls to shift slightly toward the origin, which is the same as

an increase in size in the spatial domain. Using a finite slice thickness causes the circle cross sections to be larger than if zero thickness slices were used, leading to a power spectral estimate with an inflated sphere size compared to the actual sphere size. 3DZMs are also affected by slice thickness resulting in biases in scatterer size estimates.

The effect on the RMSE for the correlation coefficient and power spectral estimates when using a finite slice thickness is shown in Figs. 4.18 (b) and 4.19 (b). When using low numbers of objects, having a 10% object diameter slice thickness actually exhibited smaller error compared to using a 0% slice thickness. However, as the number of objects in the analysis was increased, the error was larger when using a 10% compared to a 0% slice thickness. In addition, the reduction in error when increasing the number of regularly spaced slices was not as great when using 10% versus 0% slice thickness. This result suggests that the effectiveness of using regularly spaced slices was reduced significantly when increasing the slice thickness. The results in Figs. 4.18 (b) and 4.19 (b) show that the RMSE converged to a constant value as the number of objects increased. It was not possible to eliminate this error by increasing the number of regularly spaced slices or the size of the 2DZM.

The monodisperse sphere simulations demonstrated that the correlation coefficient and power spectrum for a collection of spheres could be estimated with low error from cross sections of the spheres. When estimating the correlation coefficient, the 2DZM size should be made large enough to include 15 spheres. When estimating the power spectrum, the 2DZM size should be made large enough to include 30 spheres. Using 2DZMs with at least these numbers of objects means that the estimated correlation coefficient and power spectrum will be in the region of slow RMSE decline. For monodisperse spheres, significant reductions in RMSE were achieved by increasing the regularly spaced slice density. However, when even a small slice thickness (10% of object diameter) was introduced, the advantages of using regularly spaced slices largely disappeared.

Polydisperse spheres

Figures 4.20 and 4.21 present examples of estimated correlation coefficients and power spectra for different configurations of sphere cross sections per slice and number of regularly spaced slices for collections of polydisperse spheres. The radii of the spheres had uniform distribution in the range $[0.8, 1]$. The power spectra were estimated using 2DZM method #1. A total of 50 simulations for each 2DZM size and density configuration were used.

Similar to the monodisperse sphere simulations, the polydisperse sphere simulation results in Figs. 4.20 and 4.21 show that the 2DZM estimated correlation coefficient and power spectrum converged to their respective theoretical forms as the number of object cross sections included in the analysis was increased. In contrast to monodisperse spheres, the power spectrum for polydisperse spheres did not contain any nulls, which was a significant source of error in the case of monodisperse spheres.

For the polydisperse spheres, the RMSE curves in Figs. 4.22 (a) and 4.23 (a) for the correlation coefficient and the power spectrum display a region of rapid decline followed by a region of slow decline. For the correlation coefficient and the power spectrum, the division between rapid and slow decline in the RMSE was approximately 15 polydisperse spheres included in the analysis. The region of rapid decline offered greater reductions in error for the correlation coefficient compared to the power spectrum.

The gaps between the RMSE curves for both the correlation coefficient and the power spectrum were slightly smaller than for monodisperse spheres, indicating that increasing the number of regularly spaced slices was also effective for reducing error in the case of polydisperse spheres. For example, a reduction of 30% was possible in the error when using three regularly spaced slices instead of one regularly spaced slice extracted from a single object.

Comparing the RMSE curves for the estimated correlation coefficients and power spectra for the polydisperse spheres in Figs. 4.22 (a) and Figs. 4.23 (a) to the RMSE curves for the monodisperse spheres, shows that the error was greater for the collection of polydisperse spheres. This result was consistent with expectations because more object cross sections need to be included in the analysis to account for the randomness introduced by the probability distribution that governed the scatterer size. These results suggest that for

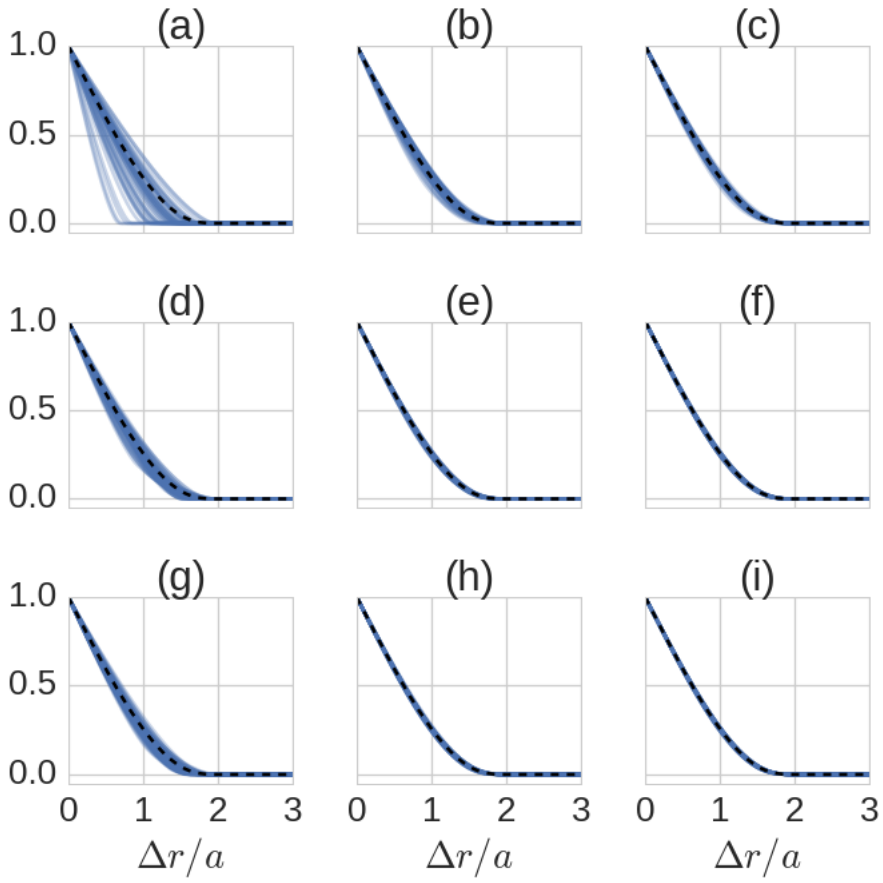

Figure 4.20: Estimated correlation coefficients for polydisperse spheres. Presentation is the same as Fig. 4.14.

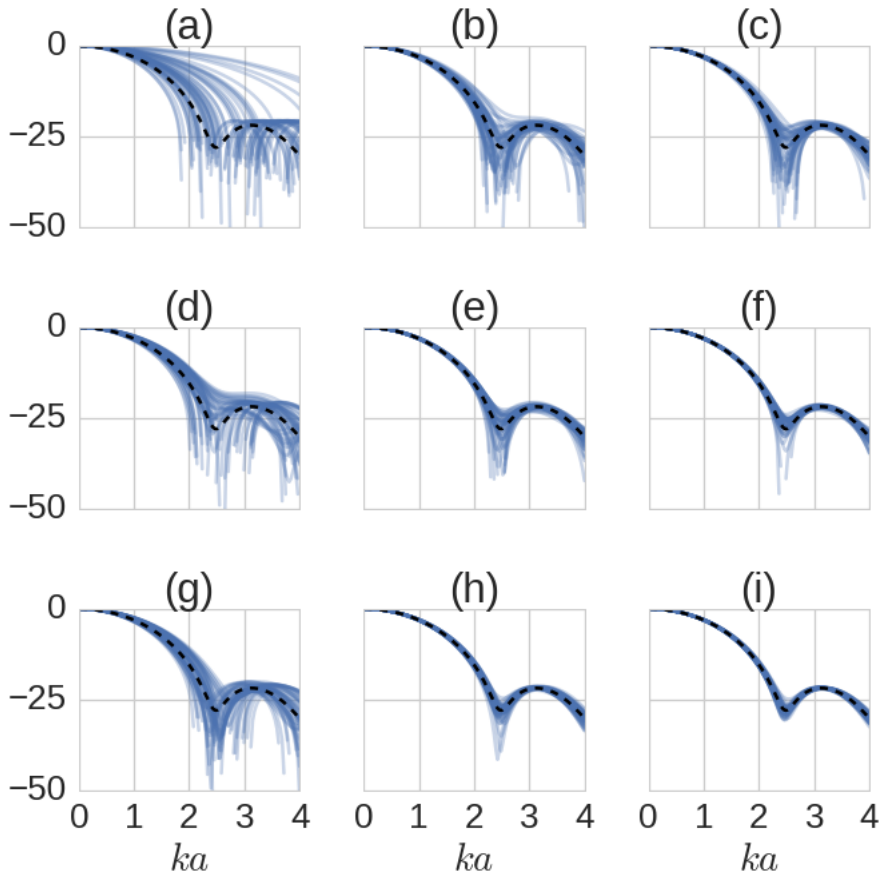

Figure 4.21: Estimated power spectra for polydisperse spheres. Presentation is the same as Fig. 4.14.

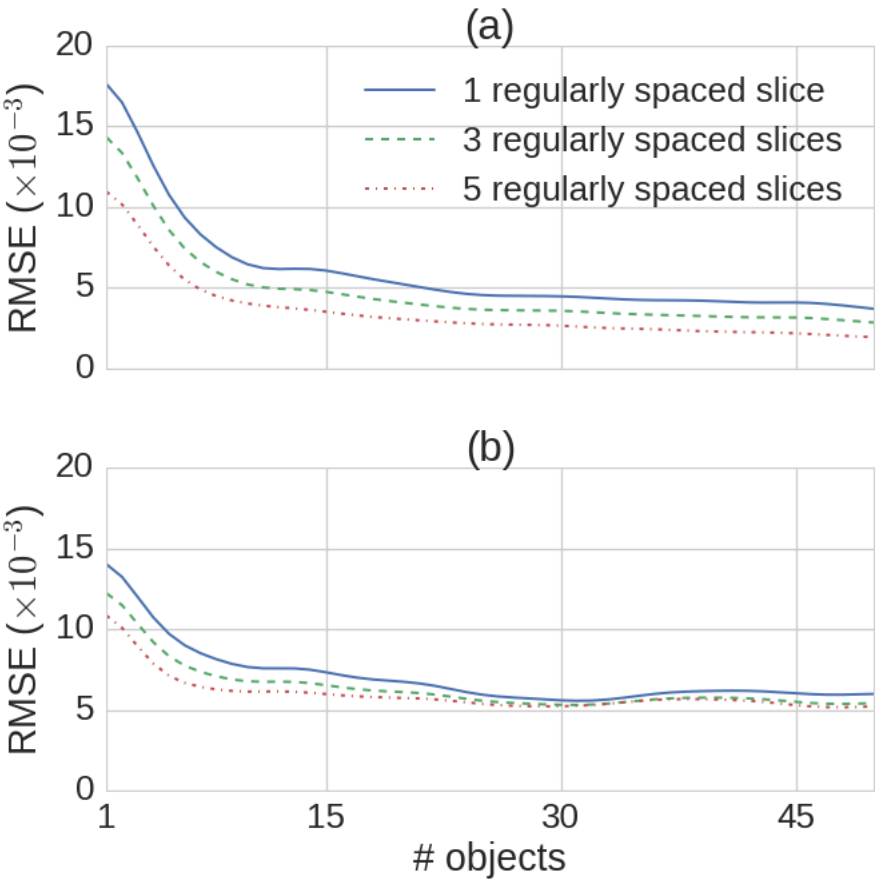

Figure 4.22: RMSE for estimated correlation coefficients. Using a slice thickness of (a) 0% (i.e., a perfect cross-section through the 3DZM) and (b) 10% of object diameter.

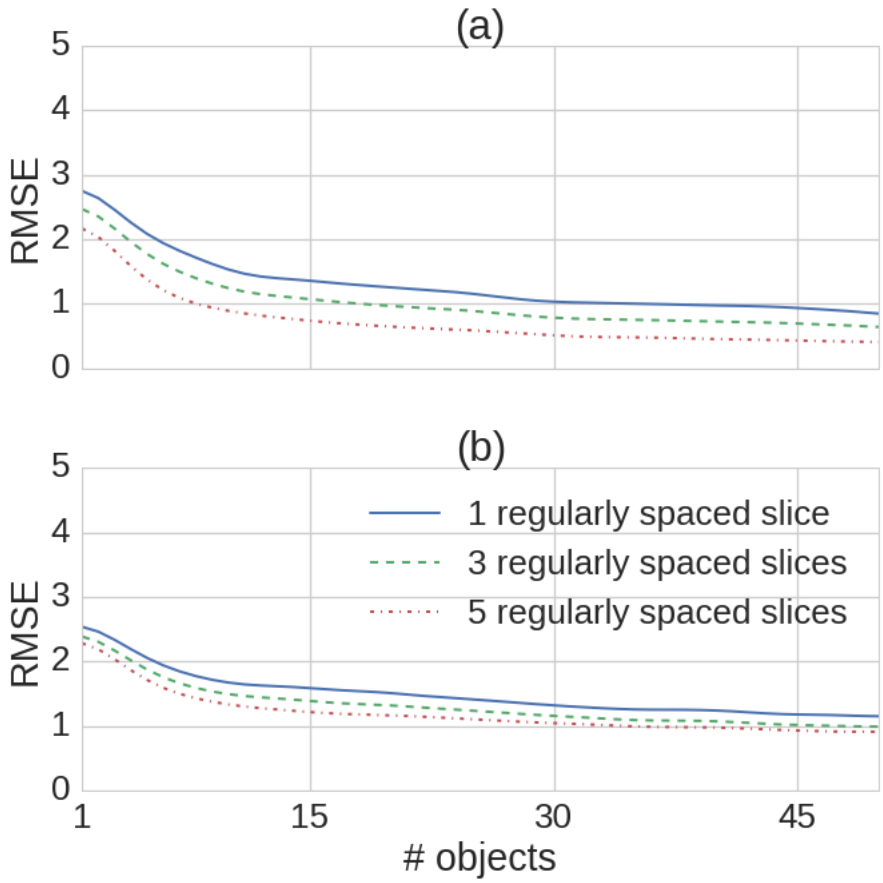

Figure 4.23: RMSE for estimated power spectra for polydisperse spheres. Using a slice thickness of (a) 0% (i.e., a perfect cross-section through the 3DZM) and (b) 10% of object diameter.

an isotropic medium of discrete scatterers with large variance in scatterer size, more objects need to be included in the analysis to achieve reductions in error. In contrast, if the variance in scatterer size is small, fewer objects need to be included in the analysis and increasing regularly spaced slices is preferable for reducing error.

In contrast to the monodisperse sphere results, where the correlation coefficient was found to converge to the theoretical correlation coefficient at a faster rate than the power spectrum converged to the theoretical power spectrum, the correlation coefficient and power spectrum for the polydisperse spheres converged at similar rates. However, based on Figs. 4.20 and 4.21, it was still apparent that the error in the correlation coefficient was smaller compared to the estimated power spectrum.

Similar to the monodisperse sphere results, the RMSE curves in Figs. 4.22 (b) and 4.23 (b) for a slice thickness of 10% of the object diameter show that increasing the slice thickness reduced the advantage of using regularly spaced slices. In addition, when using a finite slice thickness, the RMSE converged to a constant value that did not decrease when increasing the regularly spaced sliced density or the 2DZM size.

The polydisperse sphere simulations demonstrated that correlation coefficient and power spectrum for a collection of spheres having non-uniform size distribution could be estimated from cross sections of the spheres. When estimating the correlation coefficient and the power spectrum for such a collection, the 2DZM size should be made large enough to include 15 spheres. Using 2DZMs with at least this numbers of objects means that the estimated correlation coefficient and power spectrum will be in the region of slow RMSE decline. For polydisperse spheres, significant reductions in RMSE were achieved by increasing the regularly spaced slice density. However, when a finite slice thickness was introduced, the advantages of using regularly spaced slices largely disappeared.

Randomly oriented and monodisperse ellipsoids

Figures 4.24 and 4.25 present examples of estimated correlation coefficients and power spectra for different configurations of object cross sections per slice and number of regularly spaced slices for collections of monodisperse

ellipsoids. The ellipsoids had radii $[0.6, 0.8, 1.0]$. The power spectra were estimated using 2DZM method #1. A total of 50 simulations for each 2DZM size and density configuration are represented.

The randomly oriented ellipsoid simulation results in Figs. 4.24 and 4.25 show that correlation coefficients and power spectra could be estimated for non-spherical objects. Similar to the polydisperse sphere simulations, rapid reductions in error were observed for the correlation coefficient and the power spectrum by increasing the number of objects in the analysis. Similar to the polydisperse spheres, multiple randomly oriented ellipsoids were needed to estimate the correlation coefficient and power spectrum with low error.

The RMSE curves in Fig. 4.26 indicate that the division between rapid and slow decline was 15 ellipsoids included in the analysis for the correlation coefficient and the power spectrum. Including more ellipsoids in the analysis offered only marginal reductions in RMSE. Increasing the size of the 2DZM proved most beneficial for reducing RMSE in the case of the ellipsoids. Similar to the polydisperse spheres, multiple randomly oriented ellipsoids need to be included in the analysis to represent a collection of randomly oriented ellipsoids.

In the region of rapid RMSE decline, significant reductions in RMSE were achievable by increasing the regularly spaced slice density. In the region of slow RMSE decline, minimal reductions in RMSE were achievable by increasing the regularly spaced slice density.

The randomly oriented ellipsoid simulations demonstrated that correlation coefficient and power spectrum for a collection of randomly oriented and non-spherical objects could be estimated from cross sections of the objects. When estimating the correlation coefficient and the power spectrum for such a collection, the 2DZM size should be made large enough to include 15 ellipsoids. Using 2DZMs with at least this number of objects means that the estimated correlation coefficient and power spectrum will be in the region of slow RMSE decline. For the ellipsoid collection, significant reductions in RMSE were achieved by increasing the regularly spaced slice density, but only in the region of rapid decline. Therefore, for these types of objects, increasing regularly spaced slice density is not an effective strategy for reducing RMSE.

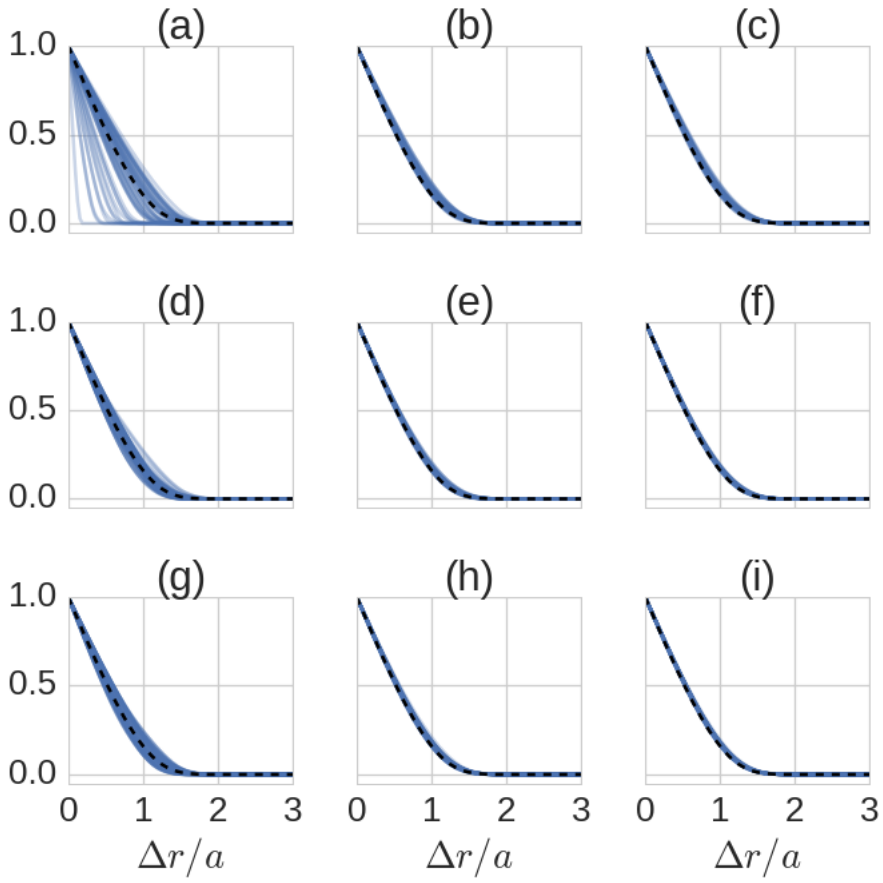

Figure 4.24: Estimated correlation coefficients for monodisperse and randomly oriented ellipsoids. Presentation is the same as Fig. 4.14.

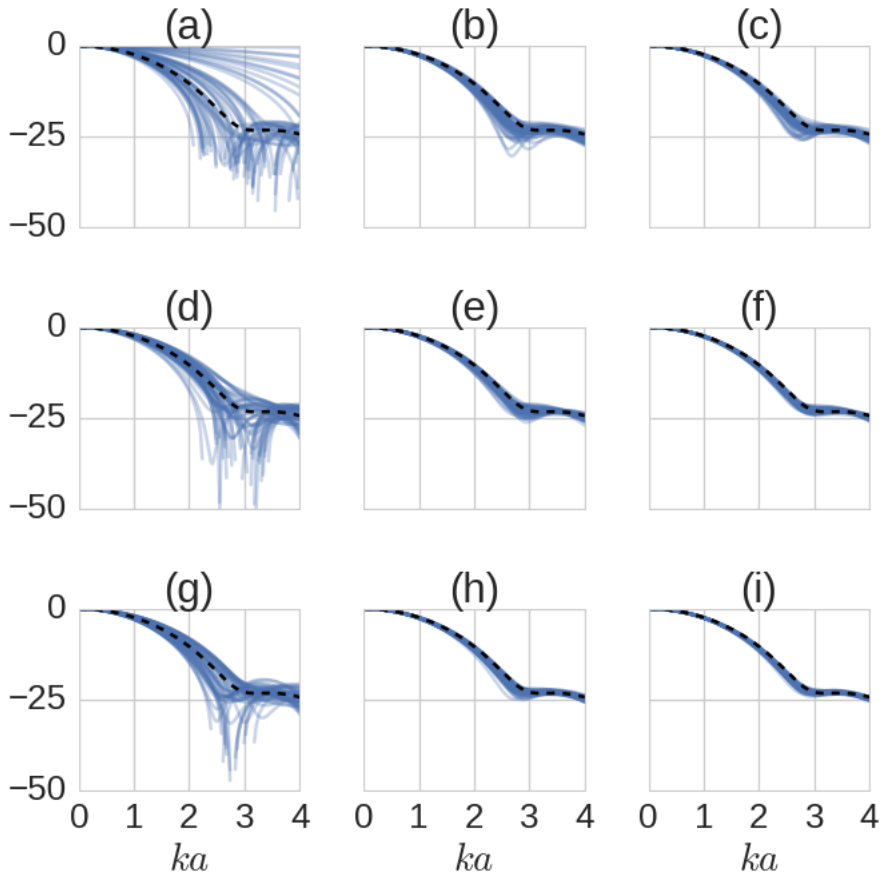

Figure 4.25: Estimated power spectra for monodisperse and randomly oriented ellipsoids. Presentation is the same as Fig. 4.14.

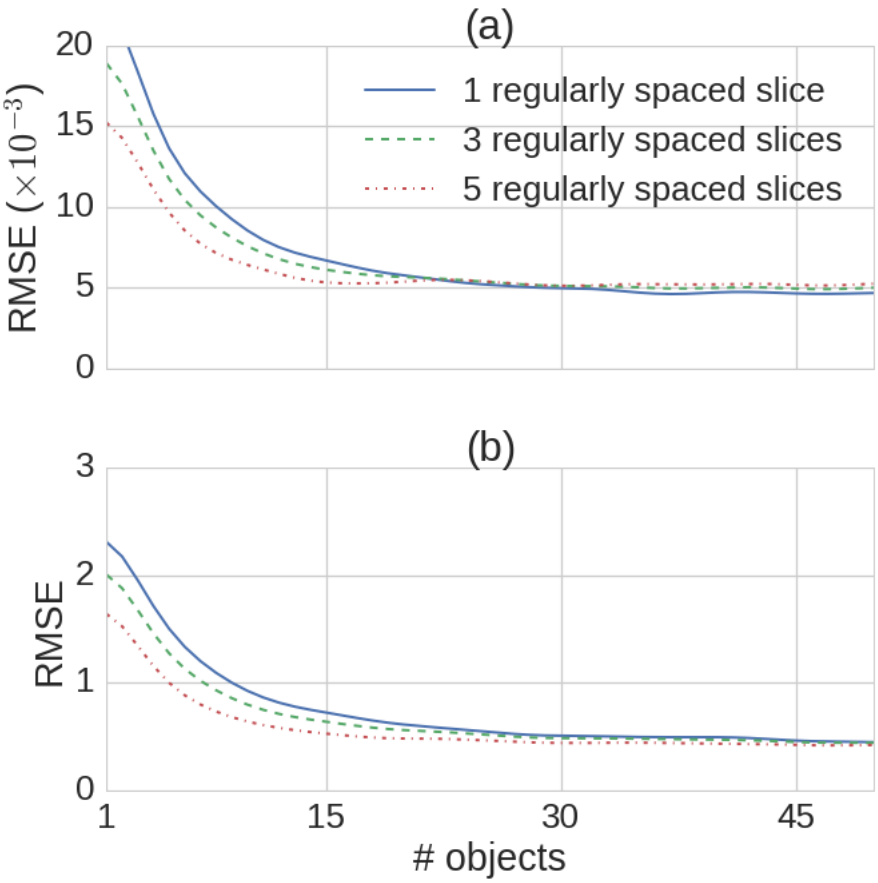

Figure 4.26: RMSE for (a) estimated correlation coefficients and (b) estimated power spectra for monodisperse and randomly oriented ellipsoids.

4.3.3 General discussion of results

The results shown in Figs. 4.14-4.26 demonstrate that correlation coefficients and power spectra can be estimated using 2DZMs for sparse isotropic media consisting of discrete collections of objects. To minimize correlation coefficient and power spectrum error, the size of the 2DZMs and regularly spaced slice density should be made as large as possible to maximize the number of object cross sections included in the analysis. However, ZM size is limited by tissue size and computational limitations. Slice density is limited by slice thickness and by the financial cost of slice processing. The simulations in this study can help to assess expected error for the slice size, spacing, and thickness in a ZM analysis of real tissue.

The results from these simulations suggest the following guidelines for determining the size of a 2DZM. Nearly all of the RMSE curves for correlation coefficients and power spectra exhibited regions of rapid decline followed by regions of slow decline when expanding the size of the 2DZM. Ideally, ZM analysis would take place in the region of slow decline, as the correlation coefficients and power spectra gradually converge to the actual quantities. For the monodisperse spheres, the cutoff between rapid and slow decline in RMSE was 15 and 30 spheres for the correlation coefficient and power spectrum, respectively. For the polydisperse spheres, the cutoff between rapid and slow decline in RMSE was 15 spheres for both correlation coefficient and power spectrum. For the randomly oriented ellipsoids, the cutoff between rapid and slow decline was 15 ellipsoids for correlation coefficient and power spectrum. Based on these simulations, it is suggested that at least 30 object cross sections be included in a ZM to guarantee that the ZM is in the region of slow decline. Fewer objects need to be included in the analysis when analyzing media that do not contain nulls in the power spectrum.

The results from these simulations suggest the following guidelines for using regularly spaced slices. Note that increasing the regularly spaced slice density cannot be accomplished by dividing a single 2DZM into smaller regions and processing the collection of 2DZMs. To realize the observed reductions in error, the slices need to be adjacent to each other at regularly spaced intervals and from a slab of the tissue that has thickness less than the size of the objects. The advantage of using regularly spaced slices was most pronounced for the sphere simulations. Only minimal reductions were observed for the

ellipsoid simulations. All of the simulations studied in this section suggest that the advantages of increasing regularly spaced slice density decreased as the number of objects in the analysis was increased. In other words, the observed reduction in RMSE from increasing the regularly spaced slice density was a function of 2DZM size and RMSE reduction decreased as the 2DZM size increased. This result was true for correlation coefficient estimates and power spectral estimates.

The results from these simulations also suggest that the advantage of using regularly spaced slices largely disappeared when using slices with thickness on the order of 10% of the object diameter. If the histology sections are greater than 10% of the radius of the suspected scattering objects in the image, using regularly spaced slices is not an effective means to reduce error in the correlation coefficient and power spectral estimates. Finite slice thicknesses distorted the sampling of the object cross sections and caused the correlation coefficients and power spectra to overestimate the actual size of the scattering objects. When estimating the scatterer size based on ZM analysis, this distorting effect of the slice thickness on scatterer size estimates needs to be kept in mind if the slice thickness is appreciable compared to the estimated scatterer size. Based on these findings, it is suggested that using regularly spaced slices in 2DZM analysis is not an effective method for reducing RMSE in correlation coefficient and power spectral estimates.

The simulations in this section were conducted for collections of spheres and ellipsoids having known sizes and the results were given in terms of those sizes. In a real tissue ZM analysis the sizes of the objects in the medium are unknown and need to be determined based on the ZM analysis. The simulation results can still be applied to guide ZM analysis of an uncharacterized medium if the first step is to use the correlation coefficient to estimate an object size, $\hat{a}$, using a model of choice. The simulation results are also presented in terms of the number of object cross sections per slice. For a sparsely filled medium of discrete objects, counting the number of object cross sections per slice can be achieved through visual inspection of histology images or the ZMs themselves. For example, it is straightforward to count the number of cell nuclei in a histology image.

4.3.4 Conclusions

The simulations in this section demonstrate that correlation coefficients and power spectra can be estimated for 3D random processes consisting of collections of discrete objects through the analysis of 2D slices extracted from these 3D volumes. The simulations demonstrate that the 2D slices need to have a sufficient size, i.e., the slices need to include a certain number of object cross sections to estimate correlation coefficient and power spectra with low error. The simulations also demonstrate that even a small slice thickness (10% of object diameter) significantly reduced the advantages of using regularly spaced slices. Therefore, when looking to improve correlation coefficient and power spectral estimates, the physical size of the 2DZM should be increased instead of trying to analyze adjacent sections from the 2DZM. In general, the results showed that 2DZMs were effective for studying 3D volume quantities such as the correlation coefficient and power spectrum from the examined random processes.

4.4 2DZM accuracy analysis of monodisperse spheres

A binary classification problem was studied in simulation using collections of sparse monodisperse spheres to assess the accuracy of the 2DZM method in a classification problem context. The first class consisted of spheres having radius 100 μm and the second class consisted of spheres having radius 90 μm (10% difference). The goal of the simulation was to determine if 2DZM analysis could be used to correctly assign an observation to its appropriate class.

The simulation for the first class consisted of the following steps. A single sphere with radius 100 μm was randomly placed to intersect a 2DZM slice such that the 2DZM contained one sphere cross section. The correlation coefficient and 3D power spectrum were estimated using this 2DZM and scatterer size estimates were made using the correlation coefficient and using the power spectrum. Next, a second sphere was randomly placed to intersect the same 2DZM slice, such that the 2DZM contained two sphere cross sections. The correlation coefficient and 3D power spectrum were estimated using this 2DZM and scatterer size estimates were made using the correlation coefficient and using the power spectrum. This process was repeated by

successively adding a new sphere to the simulated 2DZM and estimating the correlation coefficient, power spectrum, and scatterer size at each step. The result consisted of two vectors of scatterer size estimates, one using the correlation coefficient and the second for the power spectrum, given as a function of the number of spheres included in the analysis. The first vector contained scatterer sizes estimated using the correlation coefficient. The second vector contained scatterer sizes estimated using the power spectrum. This simulation was repeated for a total of 100 iterations. The simulation for the second class consisted of the same steps as for the first class, except that the sphere radius was 90 μm.

The sample data was sorted into the first or second class based on the scatterer size estimate. If the estimated scatterer size was greater than 95 μm, the sample was sorted into the first class. If the estimated scatterer size was less than 95 μm, the sample was sorted into the second class. This decision rule was applied to the simulated data described above. Sensitivity, specificity, and accuracy were calculated and are shown in Fig. 4.27 as a function of the number of sphere cross sections included in the 2DZM. Class one (100 μm) was taken to be a positive result and class two (95 μm) was taken to be a negative result. Therefore, sensitivity indicated the fraction of class one samples that were correctly assigned to class one. Specificity indicated the fraction of class two samples that were correctly assigned to class two. Accuracy represents the total number of samples that were correctly classified divided by the total number of samples. Sensitivity, specificity, and accuracy are frequently used to assess classifier performance [41].

Several observations can be made from the results shown in Fig. 4.27. Sensitivity, specificity, and accuracy were higher when using the power spectrum compared to using the correlation coefficient. This can be observed in Fig. 4.27, which shows that in general, the green line was higher than the blue line. This finding suggests that the power spectrum was better for detecting a difference in sphere size compared to the correlation coefficient.

Better performance was observed for specificity than for sensitivity. In other words, the classifier did a better job of correctly classifying spheres having smaller radius (90 μm) than it did when classifying spheres having larger radius (100 μm). For example, the sensitivity was greater than 90% when a 2DZM contained 11 or more sphere cross sections. The specificity was greater than 90% when a 2DZM contained 3 or more sphere cross sections.

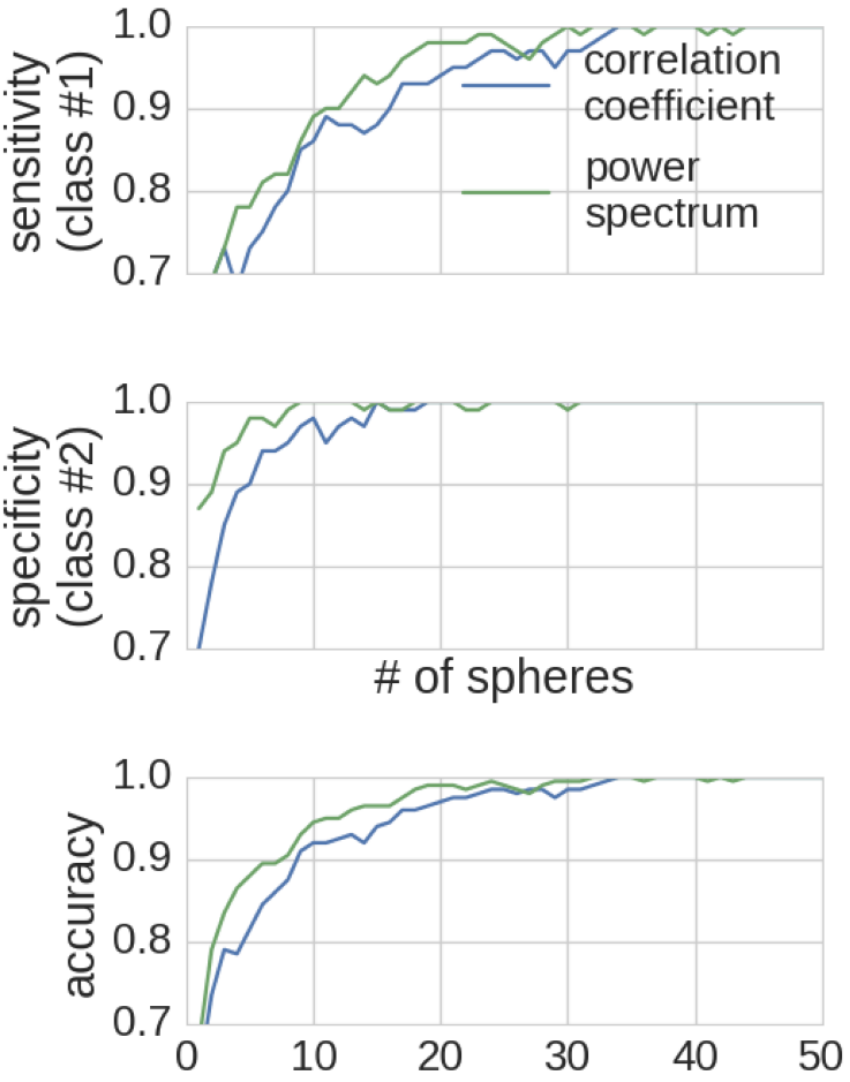

Figure 4.27: Sensitivity, specificity, and accuracy as a function of the number of sphere cross sections included in the 2DZM. The blue line represents the results when using the correlation coefficient to estimate scatterer size. The green line represents using the power spectrum to estimate the scatterer size. It should be noted that a single 2DZM is being used in this analysis and that an increase in the number of spheres indicates an increase in 2DZM size.

One possible explanation for this observation is that 2DZM analysis may tend to slightly underestimate scatterer size. The decision rule used for this analysis was rudimentary and it may be possible to improve sensitivity by adjusting the threshold used to assign observations to a class without sacrificing specificity.

The 2DZM required a small number of sphere cross sections to achieve a high level of accuracy. For example, when using the power spectrum to estimate scatterer size, accuracies of 90% and 95% were achieved when a 2DZM contained 8 and 10 sphere cross sections, respectively.

The average RMSE for the estimated correlation coefficients and power spectra used in this simulation are shown in Fig. 4.28 as a function of the number of sphere cross sections included in the 2DZM. Using these figures, it is possible to relate sensitivity, specificity, and accuracy to RMSE. For example, to achieve 95% accuracy when using the power spectrum to estimate scatterer size, required a 2DZM with 10 sphere cross sections. The average RMSE for the power spectrum when using 10 sphere cross sections was 1.5 dB.

In conclusion, the simulations in this section demonstrate that 2DZMs could be used to accurately detect differences in sphere size. The power spectrum was found to be more accurate than the correlation coefficient. Better accuracy was achieved when classifying observations having the smaller sphere size compared to the larger sphere size. Finally, a 2DZM needed to contain a small number of sphere cross sections (10) to achieve high accuracy (95%).

4.5 2DZM simulations of sparse anisotropic media

The primary goal of the simulation studies in this section was to demonstrate that in some cases, the processing steps used to estimate correlation coefficients and power spectra for isotropic media are still applicable to anisotropic media. Isotropy is a frequent assumption when studying scattering in biological media; however, this assumption will not always be valid with every tissue. Having the ability to relax the assumption of anisotropy when analyzing 2DZMs would be a major advantage.

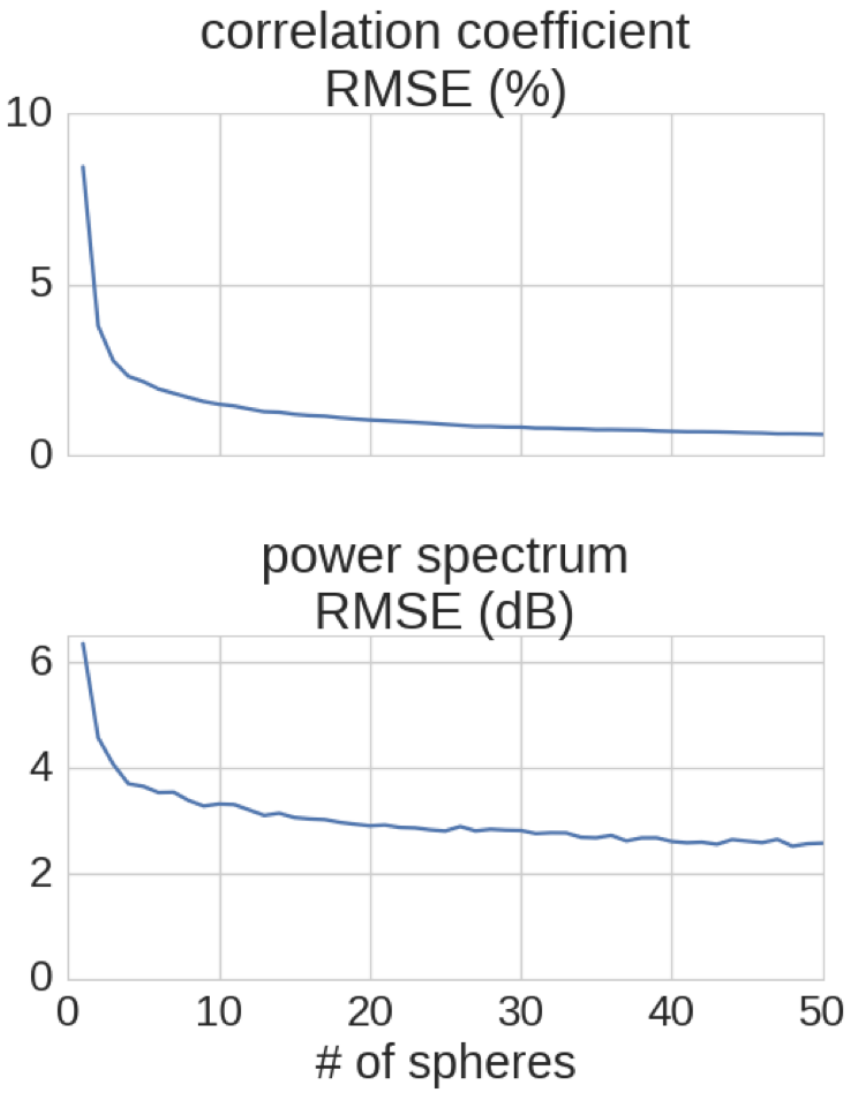

Figure 4.28: RMSE for the correlation coefficient and power spectrum as a function of the number of sphere cross sections included in the 2DZM.

4.5.1 Description of simulations

The media that were studied in this section consisted of randomly located and aligned ellipsoids with radii [0.3, 0.4, 0.5]. The ellipsoids were aligned so that the major axis of any ellipsoid having radius 0.3 was along the z-axis. The 2DZMs were sliced in the y-z plane. The goal was to use the 2DZMs to estimate the scattering response from assuming the plane wave propagation was parallel to the z plane. In this case, the shape of the scattering amplitude is the same as that of a sphere having radius 0.3. The ellipsoids were placed in the same way that the sparse objects in the previous section were placed. Figure 4.29 demonstrates how the aligned monodisperse ellipsoids were placed in the volume.

4.5.2 Simulation results

Figures 4.30 and 4.31 present examples of estimated correlation coefficients and power spectra for different configurations of object cross sections per slice and number of regularly spaced slices for collections of monodisperse ellipsoids. The power spectra were estimated using 2DZM method #1. A total of 50 simulations for each 2DZM size and density configuration are represented.

The results in Figs. 4.30 and 4.31 demonstrate that the 2DZM method could be used to estimate correlation coefficients and power spectra for an anisotropic medium. This result is significant because it suggests that the isotropy constraints applied to 2DZM method #1 may be relaxed when using this method to estimate correlation coefficients and power spectra.

The RMSE curves in Fig. 4.32 suggest that increasing regularly spaced slices was a good approach to reducing error for both the correlation coefficient and power spectrum. In addition, the RMSE curves exhibited a region of rapid decline followed by a region of slow decline for correlation coefficient and power spectrum. For the correlation coefficient, the region of rapid decline was from 1 to 7 objects. For the power spectrum, the region of rapid decline was from 1 to 10 objects. The advantages of using regularly spaced slices was reduced as the number of objects in the analysis was increased.

The correlation coefficient clearly converged to its theoretical form at a much quicker rate than did the power spectrum. Similar to the monodisperse

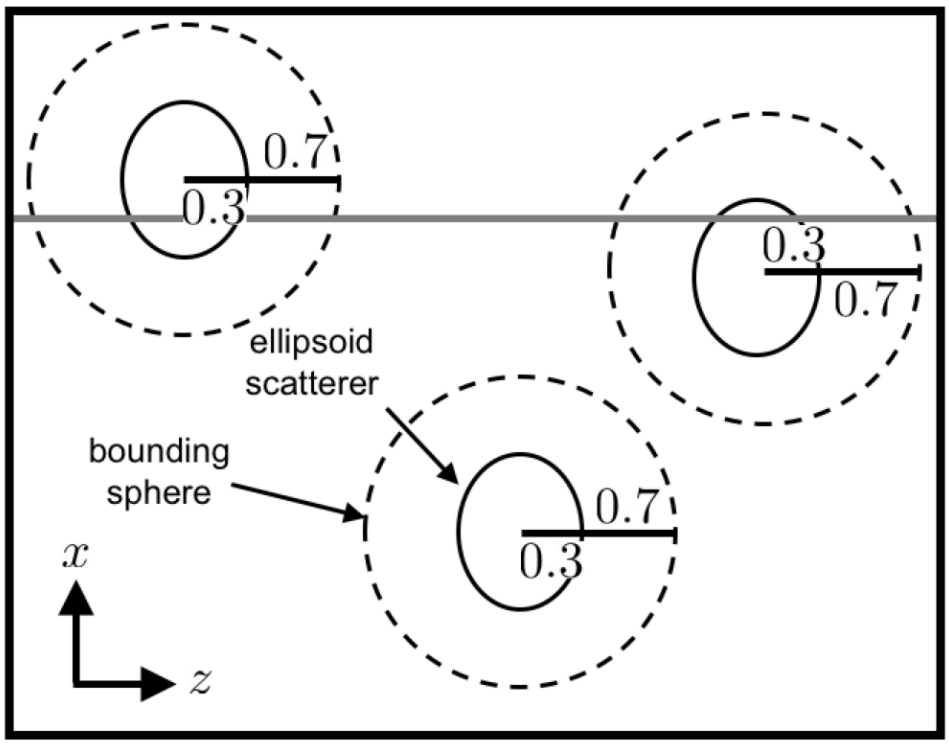

Figure 4.29: Illustration of the separation criteria for collections of sparse monodisperse and aligned ellipsoids. The black circles represent the ellipsoidal scatterers. Notice how the ellipsoids are aligned in the same direction. The ellipsoids had radii (0.3, 0.4, 0.5). The dashed circles are bounding spheres for the ellipsoidal scatterers and had radius 1.0 (twice the maximum ellipsoidal scatterer radius). The bounding spheres were not allowed to overlap so that the minimum separation distance between the ellipsoid centers was 2.0. They gray line represents a 2DZM extracted from the volume.

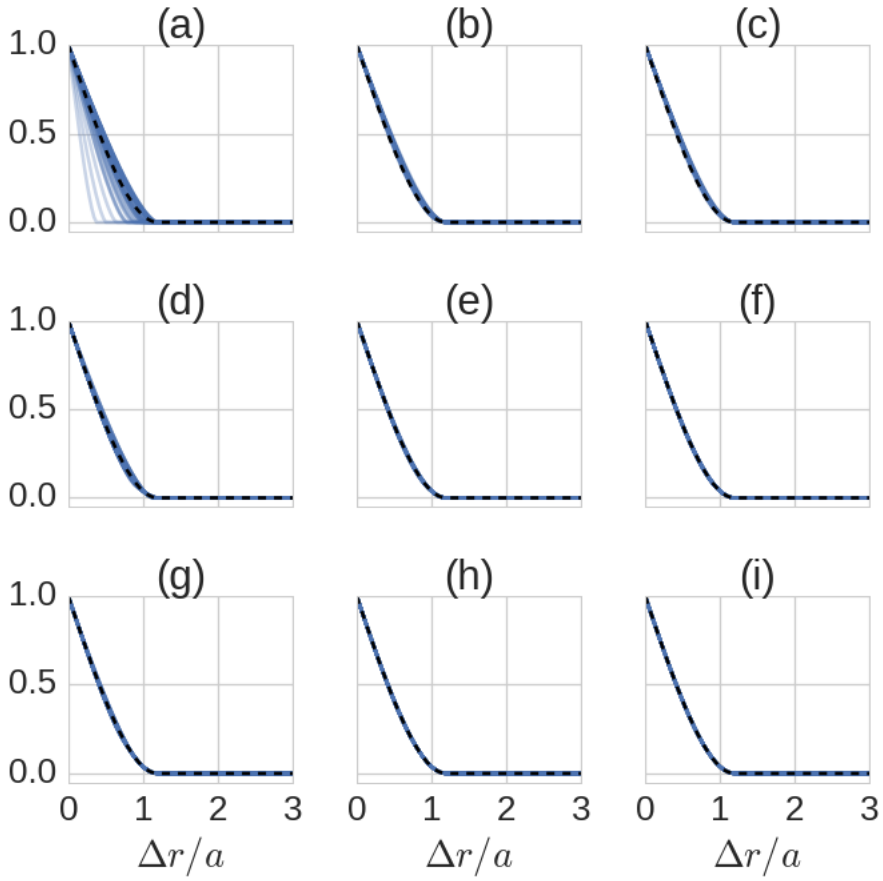

Figure 4.30: Aligned monodisperse ellipsoid simulations. Example correlation coefficient estimates when using (a, b, c) one regularly spaced slice, (d, e, f) three regularly spaced slices, and (g, h, i) five regularly spaced slices. (a, d, g) 1 object cross section per slice, (b, e, h) 15 object cross sections per slice, and (c, f, i) 30 object cross sections per slice. The dashed line represents the theoretical correlation coefficient. Each solid line represents one of 50 simulations.

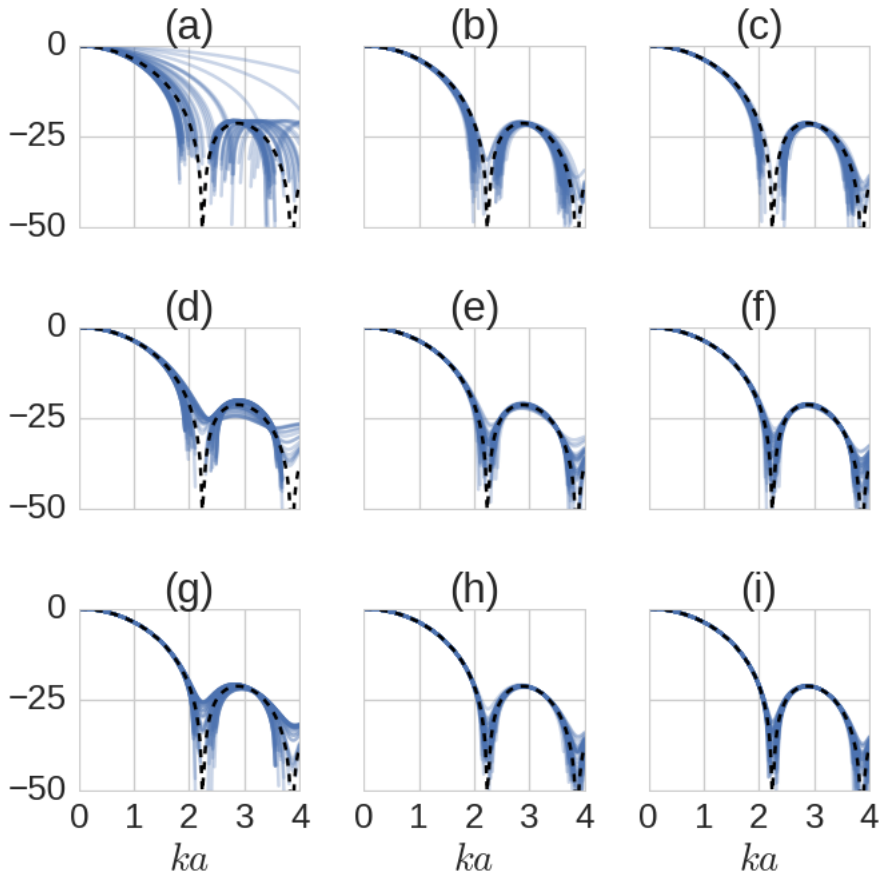

Figure 4.31: Aligned monodisperse ellipsoid simulations. Presentation is the same as Fig. 4.30 except that estimated power spectra are shown instead of correlation coefficients.

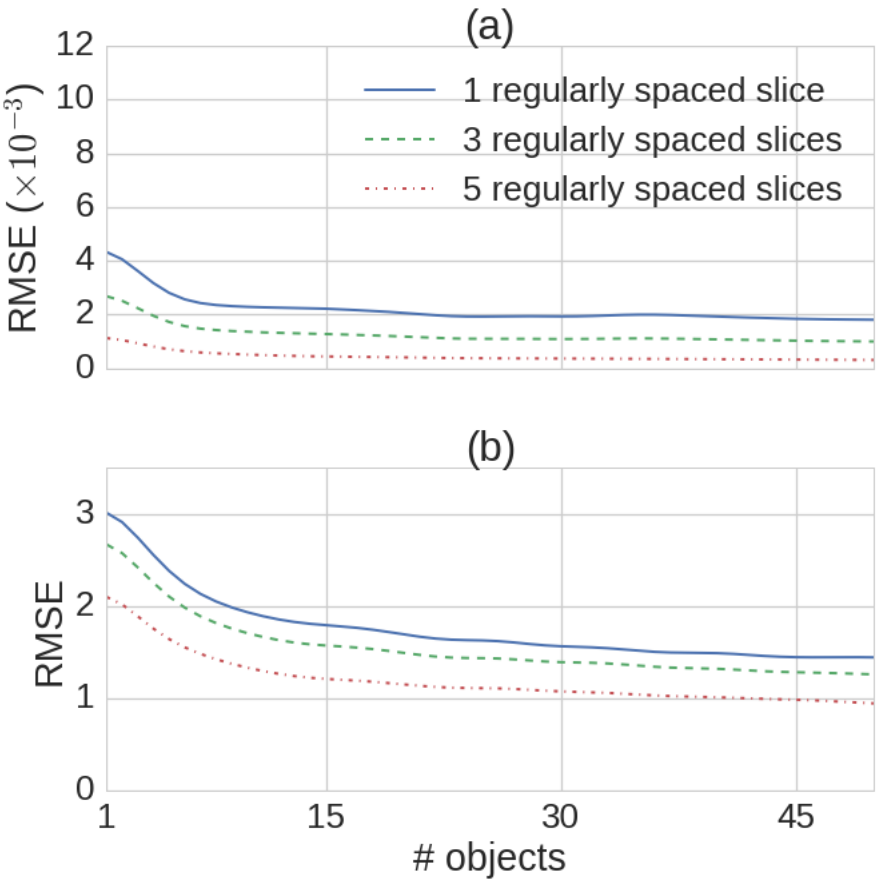

Figure 4.32: RMSE for (a) estimated correlation coefficients and (b) estimated power spectra for aligned monodisperse ellipsoids.

sphere simulations, the power spectrum for the aligned ellipsoids contained nulls, which were a large source of error for the power spectral estimates.

4.5.3 Conclusions

The simulations in this section demonstrate that 2DZM method #1 could be used to estimate the correct correlation coefficient and power spectrum for an anisotropic medium consisting of aligned ellipsoids. These results suggest that in some cases it is possible to relax the isotropy constraint required to derive the 2DZM methods while still obtaining valid results. To properly compare the 2DZM results for such an anisotropic medium to BSCs estimated using ultrasound requires that knowledge of the ultrasound propagation direction be known. However, knowledge of the ultrasound direction would also be required if 3DZMs were being used instead of 2DZMs. Therefore, this limitation is general to ZMs and not specific to 2DZMs.

4.6 2DZM simulations of continuous media

The second class of simulated media consisted of infinite phase media (i.e., continuous variations of impedance values). Whether the distribution of impedance values in biological media is continuous or discrete is still an open question. Therefore, it is important to study the 2DZM method in the context of continuous media. The continuous medium studied in this section had correlation coefficient and power spectrum that where Gaussian and are plotted in Fig. 4.33. Compared to the correlation coefficient for sparse discrete scatterers in Fig. 4.8 (a), the Gaussian correlation coefficient never falls to zero. Compared to the power spectrum for sparse discrete scatterers in Fig. 4.8 (b), the Gaussian power spectrum does not have any nulls. The spherical Gaussian medium serves as an excellent test medium to demonstrate that the 2DZM method works for continuous media.

4.6.1 Description of simulations

In these simulations, the function governing the impedance distribution for a single scatterer was specified to have a spherical Gaussian shape and scat-

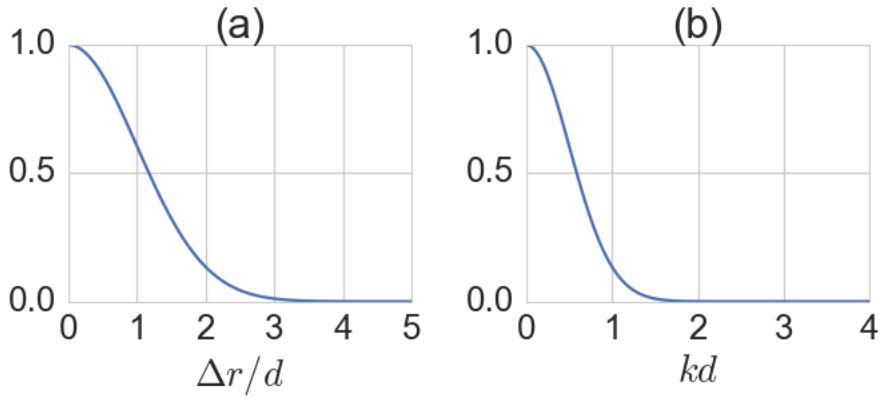

Figure 4.33: (a) Correlation coefficient and (b) power spectrum for a spherical Gaussian medium.

terers were placed to have independent positions. A copy of the specified impedance distribution was placed at each scatterer position to generate the random medium. The function governing the spatial behavior of a spherical Gaussian scatterer that is centered at the origin is given by

$$f(r) = e^{-r^2/d^2} \tag{4.4}$$

where r is the distance from the origin and the effective scatterer radius for this scatterer is $a_{eff} = d/(3\sqrt{\pi/2})^{1/3}$.

The process used to create the simulated Gaussian medium consisted of the following steps. A total of 10^4 scatterer positions inside a cube container with side length $L = 1.0$ were selected randomly and independently. In other words, each coordinate for each scatterer position in 3D space was generated using a continuous uniform random number generator with range [0, 1]. Next, a 3D grid of spatial positions that spanned the container was created. A total of 2^8 grid points were used to span each dimension so that a total of 2^{24} grid elements were used. Associated with each grid element was an impedance value. For each scatterer position, the spatial location of the scatterer was taken to be the origin and an impedance value was added to each element of the grid with magnitude depending on Eq. 4.4. The effective radius for the Gaussian scatterers was $a_{eff} = 0.02$. An example of a slice from a simulated Gaussian medium is shown in Fig. 4.34. A total of 50 independent spherical Gaussian media 3DZMs were simulated. The

theoretical correlation coefficient and power spectrum for this medium are given in Eqs. 2.20 and 2.21, respectively.

To estimate the power spectrum using the estimated correlation coefficient the following equation was used:

$$\hat{S}_3(k) = \frac{2}{k} \int_0^{\Delta r_{cutoff}} \hat{b}(\Delta r) \Delta r \sin(k\Delta r) d\Delta r \tag{4.5}$$

where Δr_{cutoff} served to eliminate the effect of the correlation coefficient amplitude values above the cutoff. The correlation coefficient values associated with the larger values of Δr represent correlations between scatterers and cause the estimated power spectrum to appear noisy. Using a Δr_{cutoff} value in this manner provides a way to smooth the estimated power spectrum without the need to increase averaging. The ability to smooth the estimated power spectrum in this manner is not possible when using 3DZM method #1 and is unique to 2DZM method #1 and 3DZM method #2. For the simulations in this section, $\Delta r_{cutoff}/\hat{d} = 4.0$, where $\hat{d}$ was the correlation length estimated from the correlation coefficient. When using this cutoff and the theoretical correlation coefficient for a spherical Gaussian medium to estimate the power spectrum, the RMSE between estimated and theoretical power spectra was less than 1%.

The estimated correlation coefficients and power spectra include two types of errors, including bias and variance. The bias component of the error is determined primarily by the size of the 2DZM used to estimate the correlation coefficient. The variance component of the error is determined by the number of 2DZMs used to estimate the correlation coefficient.

4.6.2 2DZM size

To study the bias in the estimated correlation coefficients and power spectra, the variance was eliminated by averaging large numbers of 2DZMs. Specifically, the correlation coefficient was estimated from every 2DZM from every 3DZM in this study such that a total of $256 \times 50 = 12,800$ 2DZMs were used to estimate the correlation coefficient. The 2DZM plane was perpendicular to the z-axis. Four different 2DZM sizes were studied, where the size of the 2DZM was specified by its side length L. The examined 2DZM sizes included

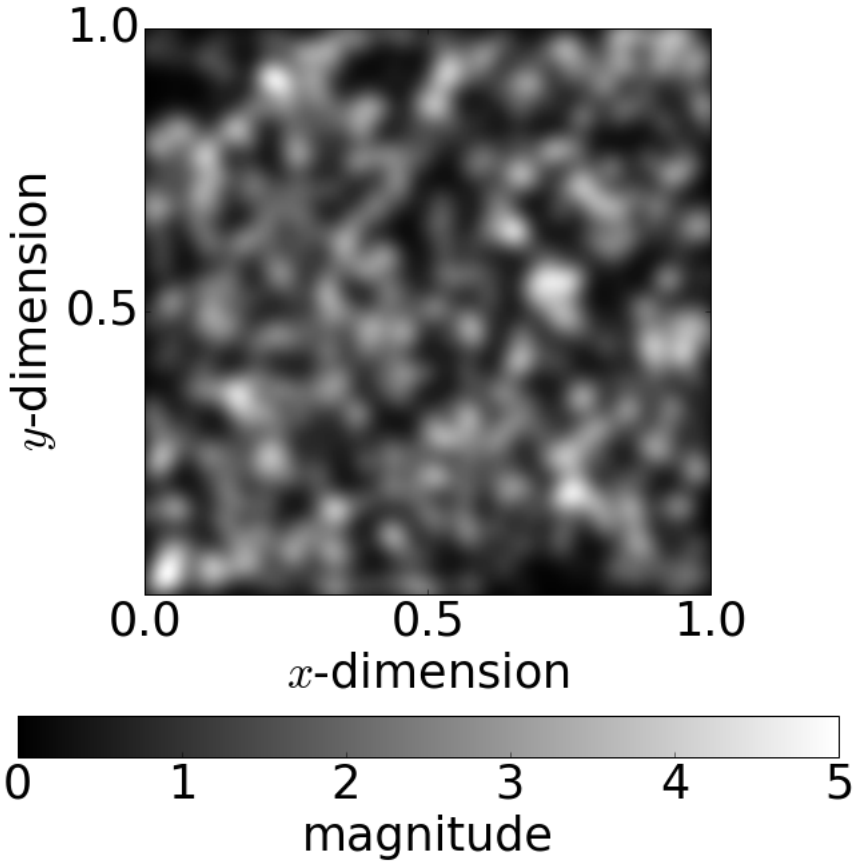

Figure 4.34: Example section from simulated spherical Gaussian medium.

$L = 0.125$, $L = 0.25$, $L = 0.5$, and $L = 1.0$.

The average estimated correlation coefficient and power spectrum for each of the studied 2DZM sizes are in Fig. 4.35. The RMSEs between estimated and theoretical correlation coefficients and the RMSEs between estimated and theoretical power spectra for the examined 2DZM sizes are shown in Fig. 4.36. Scatterer sizes were estimated from the correlation coefficients and power spectra in Fig. 4.35 and the percentage errors between the estimated and actual size are shown in Fig. 4.37.

The importance of the present simulation is demonstrated in Fig. 4.35. Large errors between the estimated and theoretical correlation coefficients (RMSE: 23%) and between the estimated and theoretical power spectra (RMSE: 101%) were observed when using 2DZMs with size $L = 0.125$. In contrast, excellent agreement was observed between the estimated and theoretical correlation coefficients (RMSE: 0.3%) and the estimated and theoretical power spectra (RMSE: 0.2%) when using 2DZMs with size $L = 1.0$.

The effect on correlation coefficient estimate bias when using a 2DZM that was too small relative to the scatterer size is shown Fig. 4.35. For example, the correlation coefficient for $L = 0.125$ in Fig. 4.35 was underestimated relative to the theoretical correlation coefficient. The RMSE curves in Fig. 4.36 show the trend that RMSE increased as 2DZM size decreased. The effect of 2DZM size on scatterer size estimates is displayed in Fig. 4.37. When using a 2DZM that was too small relative to the scatterer size, the effect on estimated scatterer size was to underestimate the actual scatterer size. For example, when using a 2DZM with size $L = 0.125$, the percent error between estimated and actual size based on the correlation coefficient was -30%.

The effect on power spectral estimate bias when using a 2DZM that was too small relative to the scatterer size is shown Fig. 4.35. For example, the power spectrum for $L = 0.125$ in Fig. 4.35 had a negative value for low values of ka. A negative power spectrum for low ka values indicates a negatively balanced correlation coefficient (i.e., the correlation coefficient is more negative than positive). The RMSE curves in Fig. 4.36 show the trend that RMSE increased as 2DZM size decreased. When using the estimated power spectrum to estimate scatterer size, the effect of using a 2DZM that was too small relative to the scatterer size was to underestimate the scatterer size. For example, when using 2DZM size $L = 0.25$, the percent error between

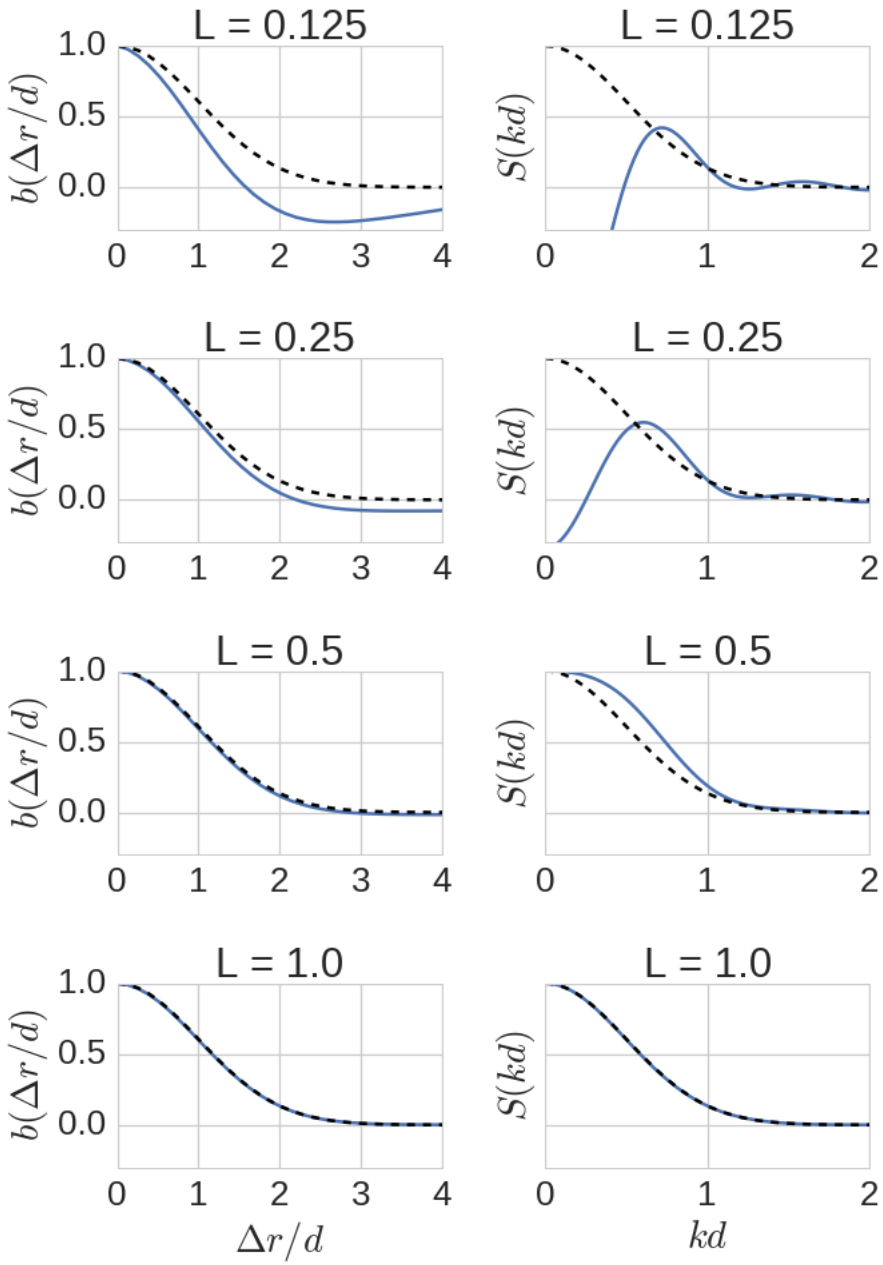

Figure 4.35: Estimated (left column) correlation coefficient and (right column) power spectrum for spherical Gaussian media using 2DZMs with different sizes. L is the side length of the studied 2DZM.

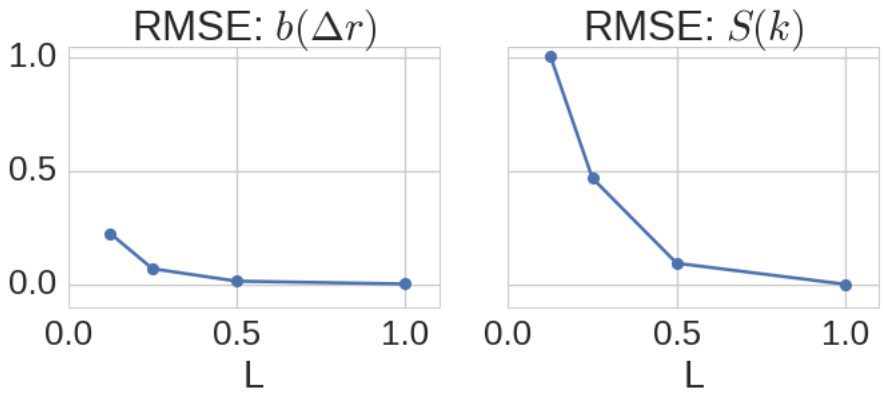

Figure 4.36: RMSE for estimated correlation coefficients and power spectra for spherical Gaussian media using 2DZMs with different sizes. L is the side length of the studied 2DZM.

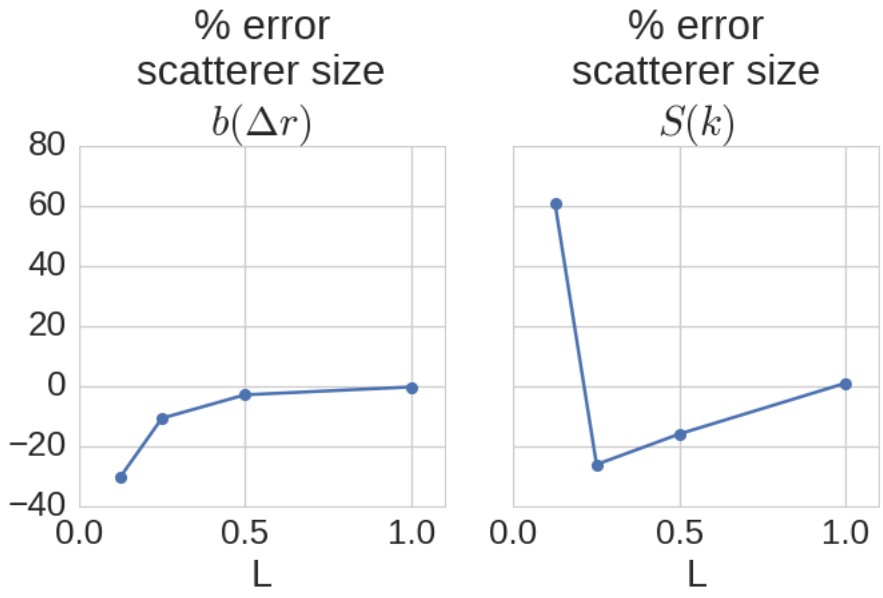

Figure 4.37: Percentage error in estimated scatterer size based on the estimated correlation coefficient and power spectrum using 2DZMs with different sizes. L is the side length of the studied 2DZM.

estimated and actual size based on the power spectrum was -25%.

From Fig. 4.37, it is interesting to note that the correlation coefficient produced scatterer size estimates with lower error compared to scatterer size estimates based on the power spectrum. For example, for $L = 0.25$ the percent error in estimated scatterer size using the correlation coefficient and power spectrum was -11% and - 25%, respectively. For $L = 0.5$, the percent error in estimated scatterer size using the correlation coefficient and power spectrum was -3.0% and -16%, respectively. This result shows that when estimating scatterer size based on ZMs in the case when correlation coefficient and power spectral variance have been eliminated, estimates based on the correlation coefficient had lower error than estimates based on the power spectrum.

In conclusion, the simulation analysis in this section was important because it demonstrated that the correlation coefficient and power spectrum could be estimated for a continuous medium using 2DZMs. In addition, the analysis demonstrated that biased correlation coefficient and power spectral estimates resulted as 2DZM size was decreased and that this bias was eliminated when using 2DZMs that had sufficient size. The important quantity is the ratio L/a, where L is the 2DZM side length and a is the scatterer radius. The RMSE between estimated and theoretical correlation coefficients was 7.0% ($L/a = 12.5$), 1.5% ($L/a = 25$), and 0.3% ($L/a = 50$). The RMSE between the estimated and theoretical power spectra was 47% ($L/a = 12.5$), 9% ($L/a = 25$), and 0.2% ($L/a = 50$). The effect of bias on scatterer size estimates was also studied and it was found that biased scatterer sizes resulted from the biased correlation coefficients and biased power spectra. The percent error in scatterer size estimates based on the correlation coefficients was -11% ($L/a = 12.5$), -3.0% ($L/a = 25$), and -0.3% ($L/a = 50$). The percent error in scatterer size estimates based on the power spectra was -25% ($L/a = 12.5$), -16% ($L/a = 25$), and 1% ($L/a = 50$). These results demonstrate the advantage of estimating scatterer size based on the correlation coefficient instead of the power spectrum.

4.6.3 Number of 2DZMs

To study the variance in the estimated correlation coefficients and power spectra, the bias was eliminated by using 2DZMs having size $L = 1.0$. The results from the previous section demonstrated that 2DZMs with this size exhibited minimal bias because excellent agreement was observed between the estimated and theoretical correlation coefficients. The variance of an estimated correlation coefficient is controlled by the number of 2DZMs that are used to estimate the correlation coefficient. Using more 2DZMs to estimate the correlation coefficient results in decreased correlation coefficient variance. Therefore, the analysis in this section consisted of changing the number of 2DZMs used to estimate the correlation coefficient in order to study correlation coefficient variance.

In order to study correlation coefficient variance, the following process was used. First, one 2DZM was randomly selected from the collection of 50 spherical Gaussian 3DZMs. A total of $256 \times 50 = 12,800$ 2DZMs were available for selection. This 2DZM was used to estimate the correlation coefficient. The RMSE between the estimated and theoretical correlation coefficients was computed. The scatterer size was estimated using the correlation coefficient. This process was repeated 100 times, that is, for 100 different randomly selected 2DZMs.

Second, ten 2DZMs were randomly selected from the collection of $12,800$ spherical Gaussian 2DZMs. The correlation coefficient was estimated using these ten 2DZMs. RMSE values were computed for the estimated correlation coefficient. Scatterer sizes were computed using the estimated correlation coefficient. This process was repeated 100 times, that is, for 100 different sets of ten randomly selected 2DZMs.

The above processing steps were repeated but using sets of $20, 30, ..., 100$ randomly selected 2DZMs from the $12,800$ spherical Gaussian 2DZMs. In this way, the correlation coefficient RMSE and estimated scatterer size could be studied as a function of the number of 2DZMs used to estimate the correlation coefficient. Because the 2DZMs were randomly selected from the set of 50 spherical Gaussian 3DZMs, which each had 256 2DZMs, the 2DZMs were independent. In addition, because the size of the 2DZMs was $L = 1.0$, the observed errors were due to variance in the estimates and not due to bias.

The process above was repeated to study power spectral variance. In

this case, each examined correlation coefficient was used to estimate a power spectrum. The RMSE was computed for each power spectrum and a scatterer size was estimated based on each power spectrum.

Examples of correlation coefficients and power spectra that were estimated using different numbers of 2DZMs are in Fig. 4.38. The RMSE between estimated and theoretical correlation coefficients and the RMSE between estimated and theoretical power spectra are shown in Fig. 4.39. Scatterer sizes were estimated from the estimated correlation coefficients and power spectra in Fig. 4.38. The percent error and coefficient of variation between the estimated and actual size as a function of the number of 2DZMs used to estimate the correlation coefficient are shown in Fig. 4.40.

Previously, it was demonstrated that 2DZMs could be used to estimate correlation coefficients when using large numbers of 2DZMs. The results in Fig. 4.38 demonstrate that correlation coefficients and power spectra could be estimated using small numbers of 2DZMs.

The displayed correlation coefficient and power spectral examples in Fig. 4.38 show the variance that results when using very small numbers of 2DZMs to estimate the correlation coefficient. This variance decreased as the number of 2DZMs used to estimate the correlation coefficient was increased. This fact is also visible in Fig. 4.39, which shows the RMSE for correlation coefficient and power spectrum as a function of the number of 2DZMs used to estimate the correlation coefficient. The RMSE decreased as the number of 2DZMs used to estimate the correlation coefficient was increased. For the correlation coefficient, the RMSE was 3.0% (1 2DZM), 0.9% (10 2DZMs), and 0.5% (20 2DZMs). For the power spectrum, the RMSE was 11% (1 2DZM), 4% (10 2DZMs), and 2% (20 2DZMs).

Mean percent error in estimated scatterer size based on the correlation coefficient and power spectrum are shown in Fig. 4.40. For scatterer size estimates based on the correlation coefficients and power spectra, the mean percent error was typically less than 1%. This result shows that scatterer size estimates using 2DZMs having size $L = 1.0$ were not biased. The advantage of increasing the number of 2DZMs used to estimate the correlation coefficient can be observed in the scatterer size coefficient of variation curves in Fig. 4.40. The coefficient of variation decreased sharply as the number of 2DZMs used to estimate the correlation coefficient increased. For scatterer sizes estimated from the correlation coefficient, the coefficient of variation was

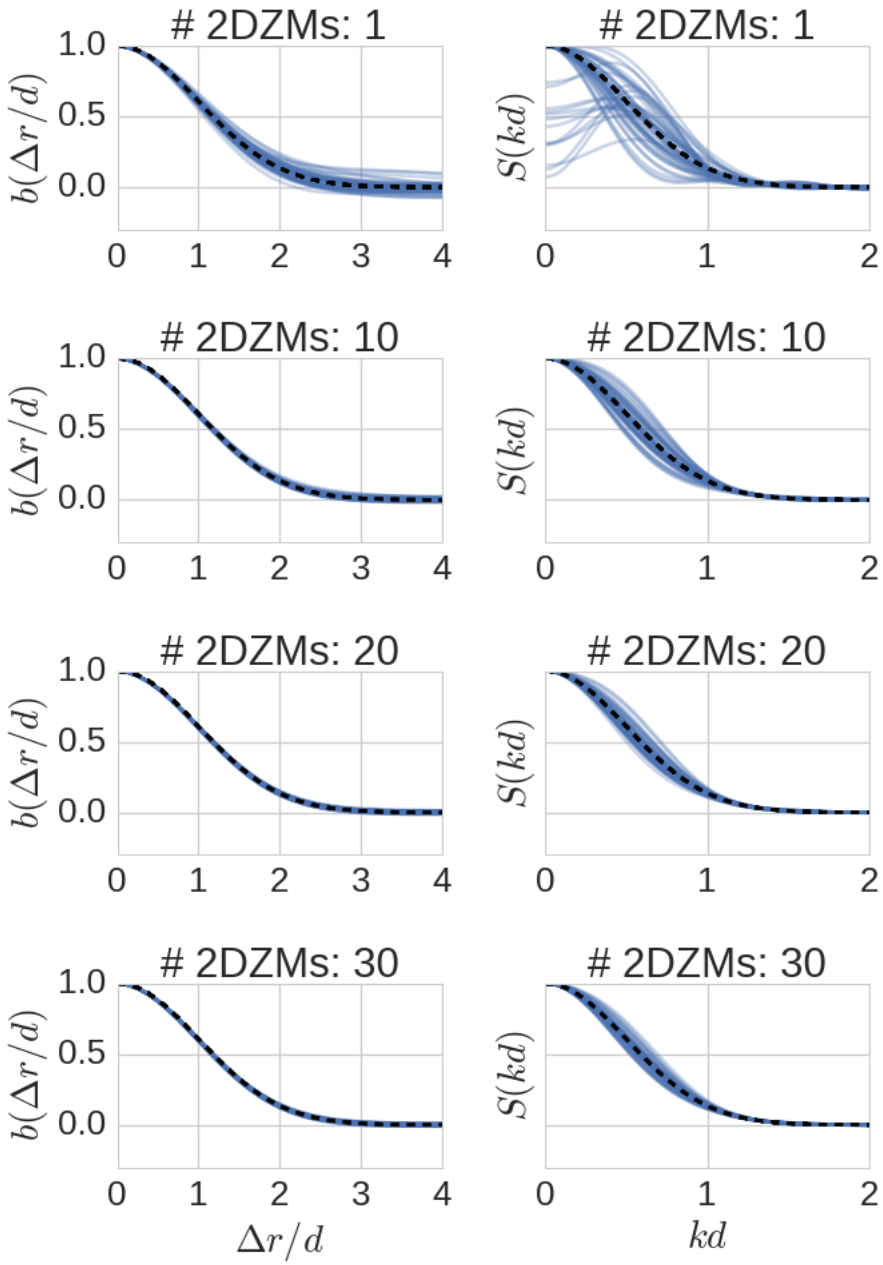

Figure 4.38: Estimated (left column) correlation coefficient and (right column) power spectrum for spherical Gaussian media using different numbers of 2DZMs to estimate the correlation coefficient.

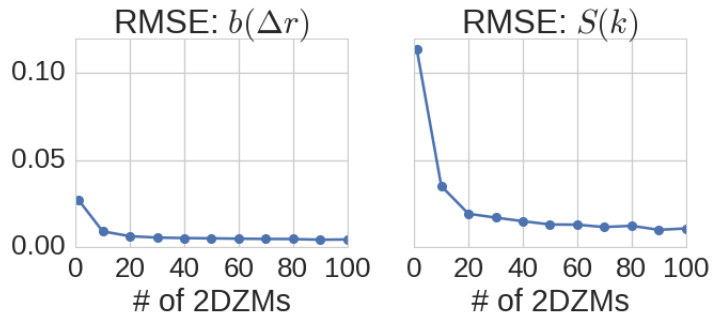

Figure 4.39: RMSE for estimated correlation coefficients and power spectra for spherical Gaussian media using different numbers of 2DZMs to estimate the correlation coefficient.

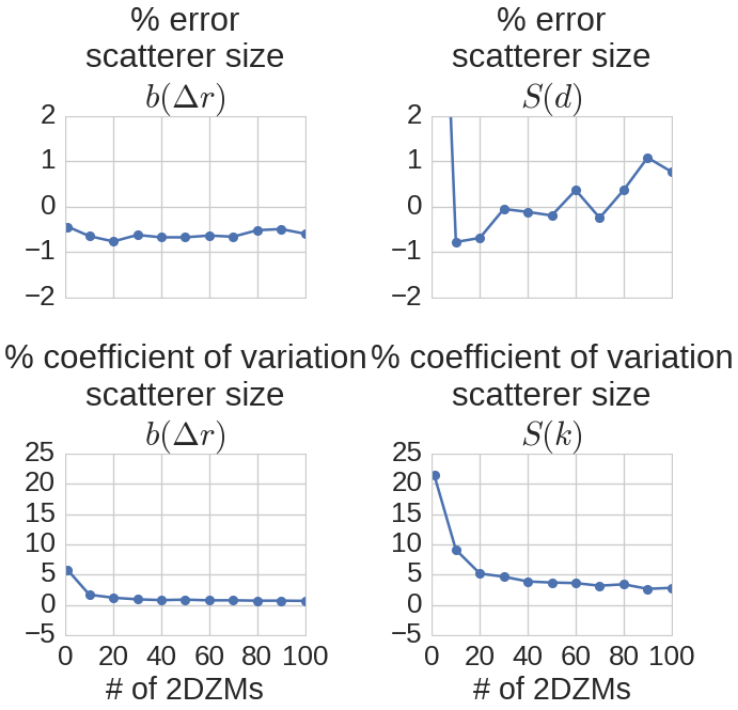

Figure 4.40: Percentage error and coefficient of variation of the estimated scatterer size using the correlation coefficient and using the power spectrum as a function of the number of 2DZMs used to estimate the correlation coefficient.

5.7% (1 2DZM), 1.7% (10 2DZMs), and 1.2% (20 2DZMs). For scatterer sizes estimated from the power spectrum, the coefficient of variation was 21% (1 2DZM), 9.1% (10 2DZMs), and 5.2% (20 2DZMs). These results demonstrate the advantage of estimating scatterer size based on the correlation coefficient instead of the power spectrum.

In conclusion, the simulation analysis in this section was important because it demonstrated that the correlation coefficient and power spectrum could be estimated using small numbers of 2DZMs. For comparison, a corresponding 3DZM analysis of the media simulated in this section would have included 256 2DZMs. The analysis in this section demonstrated that correlation coefficient and power spectral variance were reduced by increasing the number of 2DZMs used to estimate the correlation coefficient. Finally, the results suggest that using the correlation coefficient to estimate scatterer sizes was more robust compared to using the power spectrum.

4.6.4 Conclusions

The simulations in this section demonstrate that 2DZMs could be used to estimate the correlation coefficient and power spectrum for an isotropic continuous medium having correlation coefficient and power spectrum described by a Gaussian function. Two sources of error in the correlation coefficient and power spectral estimates were examined, including bias and variance. The analysis of bias found that it was necessary to use a sufficiently sized 2DZM to estimate the correlation coefficient; otherwise, biased correlation coefficient and power spectral estimates resulted. For example, to achieve correlation coefficient and power spectrum RMSE less than 1% required the use of a 2DZM with side length that was 50 times the scatterer radius. The analysis of variance demonstrated that small numbers of 2DZMs (relative to the number of 2DZMs included in a 3DZM) could be used to estimate the correlation coefficient and power spectrum. For example, to achieve correlation coefficient RMSE less than 2% required that 10 2DZMs be used to estimate the correlation coefficient. To achieve power spectrum RMSE of 5% required that 20 2DZMs be used to estimate the correlation coefficient. Both analyses suggested that scatterer size estimates based on the correlation coefficient had lower error than scatterer size estimates based on the power spectrum.

For specifying 2DZM size, the important quantity is the ratio between the 2DZM characteristic length L (e.g., side length or diameter) and the radius of the scattering objects, a. When conducting a ZM analysis, the quantity a is unknown and must be estimated initially. Once an initial estimate has been made, it can be determined whether the ZM is large enough relative to the estimated scatterer size. If not, the ZM can be expanded until the ratio between 2DZM size and scatterer size is of sufficient size. The results of this simulation can be used to guide determination of this sufficient size.

4.7 2DZM simulations of dense two-phase media

The sparse collections of discrete objects and the spherical Gaussian continuous medium simulations demonstrated that the 2DZM method works for media having correlation coefficients and power spectra determined by the size and shape of individual scatters. The goal of this section was to demonstrate that the 2DZM method also works for media with correlation coefficients and power spectra that depend on the size and shape of the scatterers, but also the 3D positions of the scatterers.

The simulations in this section consisted of dense collections of spheres having volume fraction 30%. The theoretical correlation coefficient and power spectrum for this random process are in Fig. 4.41. For finite sized volumes, these curves result when averaging over many realizations. Compared to the correlation coefficient for sparse discrete objects in Fig. 4.8 (a) and for a spherical Gaussian medium in 4.33 (a), the correlation coefficient for dense collections of monodisperse spheres in Fig. 4.41 (a) exhibits structure that depends on the 3D positions of the scatterers. Similar structure is exhibited for the power spectrum. The purpose of this section was to demonstrate that the 2DZM method was still able to capture the more complex structure in the correlation coefficient and power spectrum.

A total of 50 cube container volumes with side length $L = 1.0$ were filled with spherical scatterers having radius $a = 0.02$ and a volume fraction of 30%. The Metropolis algorithm was used to place the spheres so that they did not overlap. The 3D volume grid was sampled at 2^8 points along each dimension for a total of 2^{24} sampling points. The 2DZM plane was perpendicular to the z-axis. Equation 4.5 was used to estimate the power spectrum from the

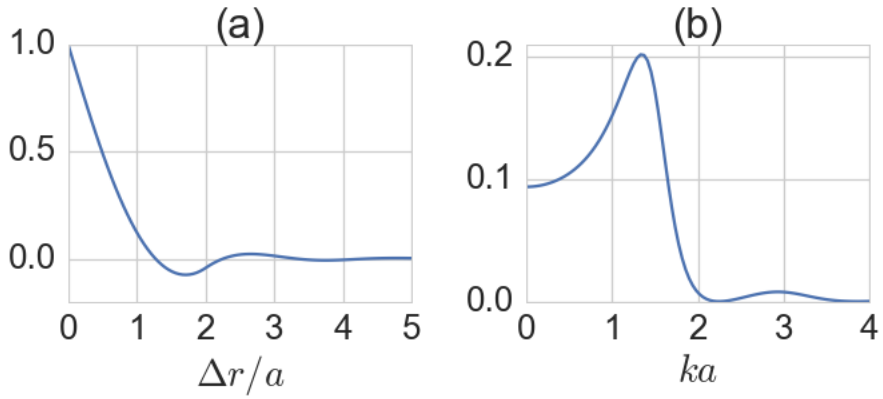

Figure 4.41: (a) Correlation coefficient and (b) power spectrum for a collection of dense monodisperse spheres with volume fraction 30%.

estimated correlation coefficient.

4.7.1 2DZM size

To study the bias in the estimated correlation coefficients and power spectra, the variance was eliminated by averaging large numbers of 2DZMs. Specifically, the correlation coefficient was estimated from all available 2DZMs in this study such that a total of $256 \times 50 = 12,800$ 2DZMs were used to estimate the correlation coefficient. Four different 2DZM sizes were studied, where the size of the 2DZM was specified by its side length L. The examined 2DZM sizes included $L = 0.0625$, $L = 0.125$, $L = 0.25$, and $L = 0.5$.

The estimated correlation coefficient and power spectrum for each of the studied 2DZM sizes are in Fig. 4.42. The RMSE between estimated and theoretical correlation coefficients and the RMSE between estimated and theoretical power spectra for the different sized 2DZMs are shown in Fig. 4.43.

The previous simulation results established that 2DZM analysis can capture information about the 3D size and shape of scatterers. The results in Fig. 4.42 are important because they demonstrate that 2DZMs can also capture information about the 3D location of the scatterers. Excellent agreement was observed between the 2DZM estimated and theoretical correlation coefficients (RMSE: 0.2%) in Fig. 4.42 when using 2DZMs with size $L = 0.5$. Good

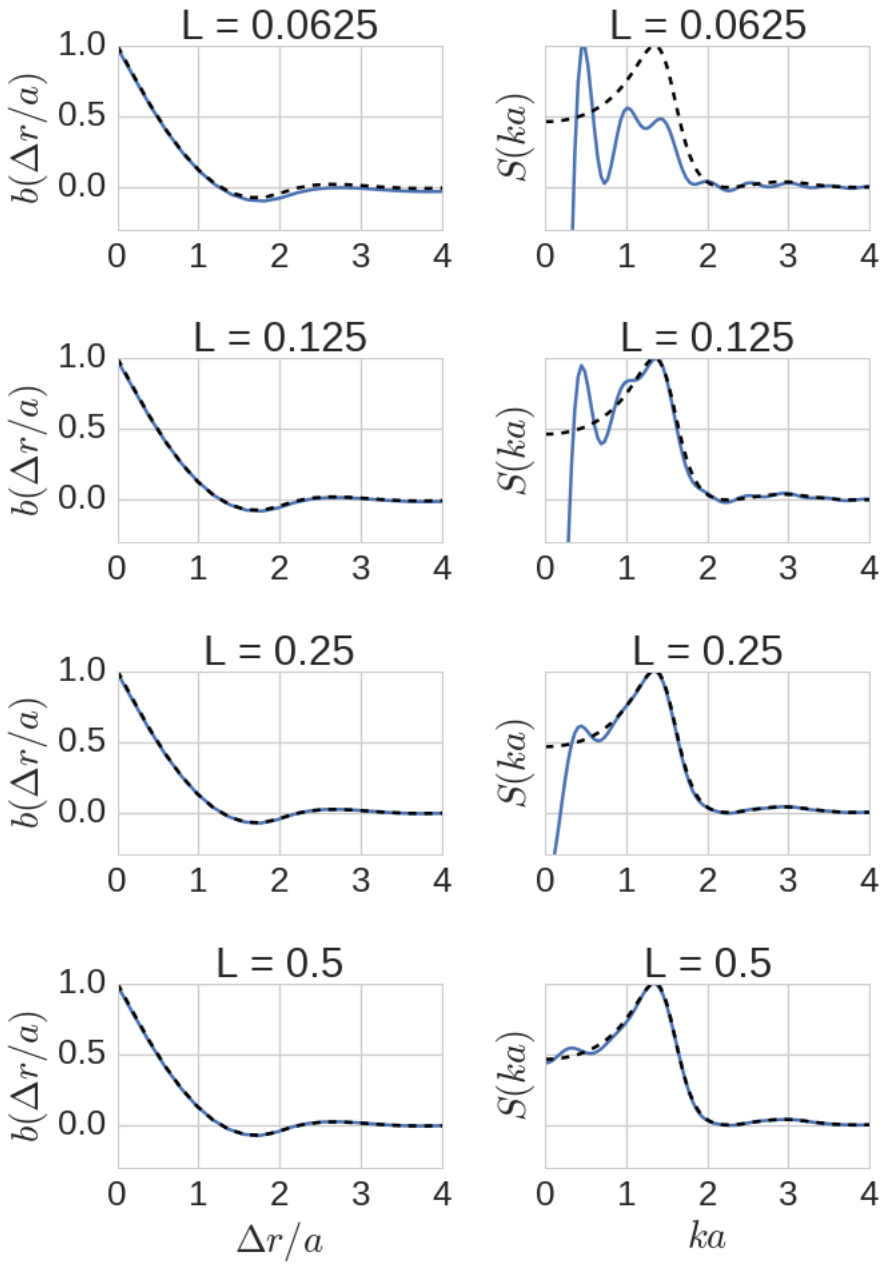

Figure 4.42: Estimated (left column) correlation coefficient and (right column) power spectrum for dense spheres with volume fraction 30% using 2DZMs with different sizes.

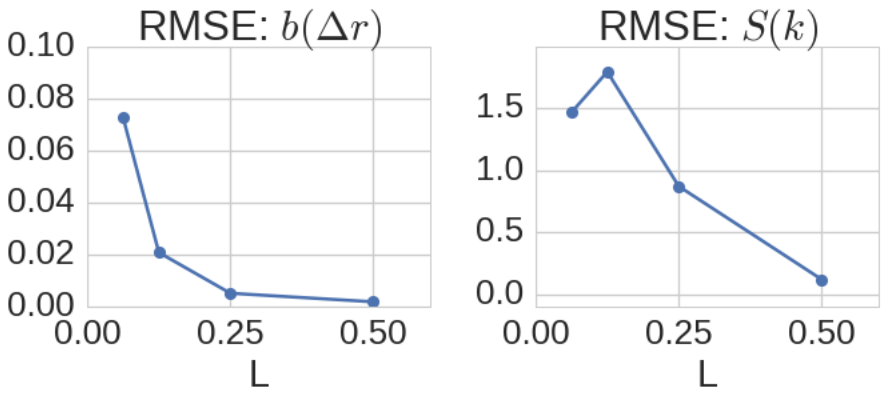

Figure 4.43: RMSE for estimated correlation coefficients and power spectra for dense spheres with volume fraction 30% using 2DZMs and different 2DZM sizes.

agreement was observed in the case of the power spectrum (RMSE: 11%). Good agreement was observed between estimated and theoretical correlation coefficients (RMSE: 7.0%) using 2DZM size $L = 0.0625$. Poor agreement was observed for the power spectrum (RMSE: 150%) using this size 2DZM.

The results in Fig. 4.42 demonstrate the importance of using a 2DZM having sufficient size relative to the scatterer size. When a 2DZM size that was too small was used, the correlation coefficient and power spectral estimates were biased. The correlation coefficient was underestimated when using 2DZM size that was too small. The power spectrum exhibited negative values for small values of ka when the 2DZM size was too small. When conducting 2DZM analysis, it is important to determine if a sufficiently sized 2DZM is being used.

The RMSE curves in Fig. 4.43 show that error decreased as the size of the 2DZM was increased. The error between the estimated and theoretical power spectra was larger than that between estimated and theoretical correlation coefficients. Because only small errors were observed in the estimated correlation coefficient, but larger errors were observed in the power spectrum, this result suggests that the power spectral estimate was sensitive to small errors in the correlation coefficient estimate. Similar to the spherical Gaussian sphere simulations, this finding suggests that when conducting 2DZM analysis, it may be better to analyze the correlation coefficient instead of the

power spectrum.

In conclusion, the simulation analysis in this section was important because it showed that the correlation coefficient and power spectrum could be estimated for a dense collection of spheres using 2DZMs in the case that correlation coefficient variance was eliminated. The finding is significant because it shows that 2DZMs can capture information about the 3D spatial positions of the scatterers in addition to information about the size and shape of the scatterers. The results indicated that increasing 2DZM size relative to the scatterer size reduced bias in the estimated correlation coefficient and power spectrum. The important quantity is the ratio L/a, where L is the 2DZM side length and a is the scatterer radius. The RMSE between estimated and theoretical correlation coefficients was 2.0% ($L/a = 6.25$), 0.5% ($L/a = 12.5$) , and 0.1% ($L/a = 25$). The RMSE between the estimated and theoretical power spectra was 180% ($L/a = 6.25$), 87% ($L/a = 12.5$), and 11% ($L/a = 25$).

4.7.2 Number of 2DZMs

To study the variance in the estimated correlation coefficients and power spectra, the bias was eliminated by using 2DZMs having size $L = 0.5$. The results from the previous section demonstrated that 2DZMs with this size exhibited minimal bias because excellent agreement was observed between the estimated and theoretical correlation coefficients. The analysis in this section consisted of changing the number of 2DZMs used to estimate the correlation coefficient in order to study correlation coefficient variance.

In order to study correlation coefficient variance, the process used to study variance in the spherical Gaussian simulations was used. First, one 2DZM was randomly selected from the collection of $256 \times 50 = 12,800$ dense sphere 2DZMs. This 2DZM was used to estimate the correlation coefficient. The RMSE between the estimated and theoretical correlation coefficients was computed. This process was repeated 100 times, that is for 100 different randomly selected 2DZMs. Second, ten 2DZMs were randomly selected from the collection of $12,800$ dense sphere 2DZMs. The correlation coefficient was estimated using these ten 2DZMs. RMSE values were computed for the estimated correlation coefficient. This process was repeated 100 times,

that is, for 100 different sets of ten randomly selected 2DZMs. Third, the described processing steps were repeated but using sets of $20, 30, ..., 100$ randomly selected 2DZMs from the $12,800$ dense sphere 2DZMs. In this way, the correlation coefficient RMSE could be studied as a function of the number of 2DZMs used to estimate the correlation coefficient. Because the 2DZMs were randomly selected from the set of 50 dense sphere 3DZMs, which each had 256 2DZMs, it was safe to assume that the 2DZMs were independent. In addition, because the size of the 2DZMs was $L = 0.5$, it was safe to assume that observed errors were due to variance in the estimates and not due to bias.

The process above was repeated to study power spectral variance. In this case, each examined correlation coefficient was used to estimate a power spectrum and the RMSE was computed for each power spectrum.

Examples of correlation coefficients and power spectra that were estimated using different numbers of 2DZMs are in Fig. 4.44. The RMSE between estimated and theoretical correlation coefficients and the RMSE between estimated and theoretical power spectra are shown in Fig. 4.45.

Previously, it was demonstrated that 2DZMs could be used to estimate the correlation coefficient for dense spheres when using large numbers of 2DZMs having sufficient size relative to the scatterer size. The results in Fig. 4.44 demonstrate that correlation coefficients could be estimated with low error using small numbers of 2DZMs. The findings are significant for 2DZM analysis because smaller numbers of 2DZMs were required to estimate the correlation coefficient than would be needed to conduct a 3DZM analysis.

The displayed correlation coefficients in Fig. 4.44 show the variance that resulted when using very small numbers of 2DZMs to estimate the correlation coefficient. The variance decreased as the number of 2DZMs used to estimate the correlation coefficient was increased. This fact is also visible in Fig. 4.45, which shows the RMSE for correlation coefficient as a function of the number of 2DZMs used to estimate the correlation coefficient. For the correlation coefficient, the RMSE was 1.3% (1 2DZM), 0.5% (10 2DZMs), and 0.5% (20 2DZMs). These results suggest that estimation of the correlation coefficient was possible using small numbers of 2DZMs.

The displayed power spectra in Fig. 4.44 show that the variance of the estimated power spectra decreased as the number of 2DZMs used to estimate the correlation coefficient was increased. However, the variance of the power

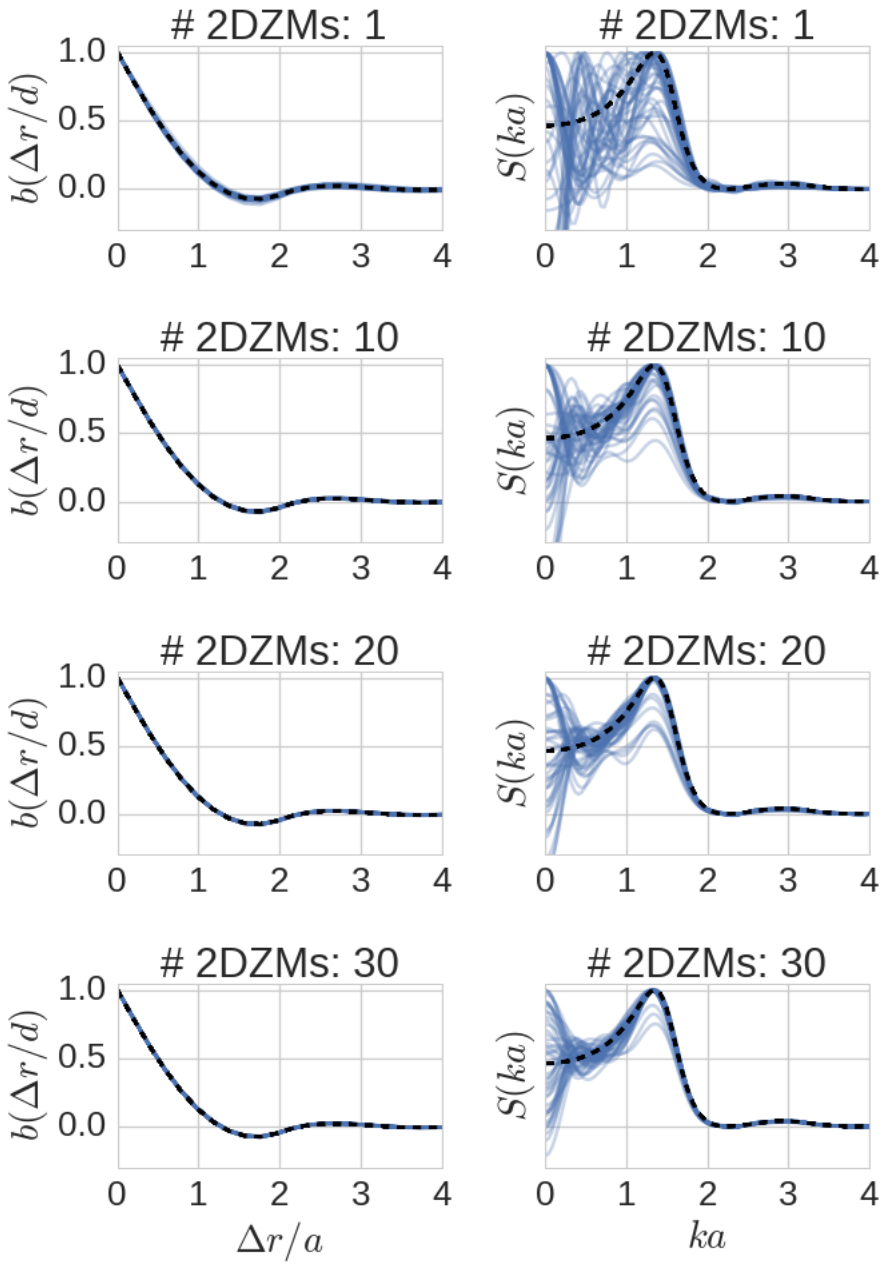

Figure 4.44: Estimated (left column) correlation coefficient and (right column) power spectrum for dense spheres with volume fraction 30% using different numbers of 2DZMs.

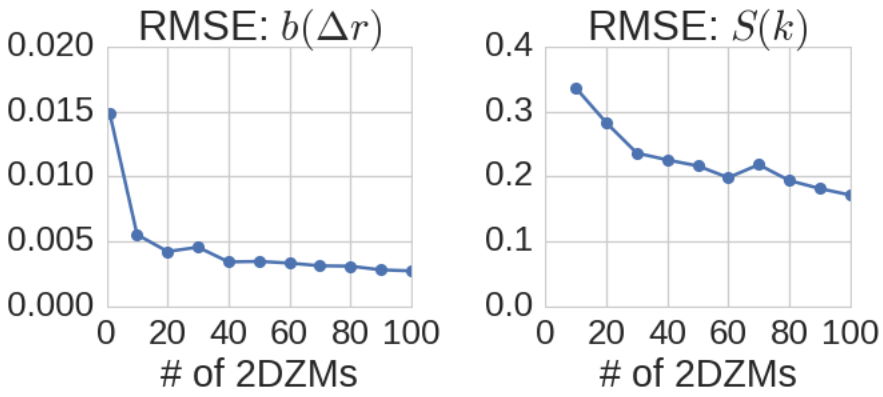

Figure 4.45: RMSE for estimated correlation coefficients and power spectra for dense spheres with volume fraction 30% using different numbers of 2DZMs.

spectral estimates was significantly larger than the variance observed for the correlation coefficients. These results suggest that the power spectrum was sensitive to small errors in the correlation coefficient estimate. Nonetheless, the RMSE in Fig. 4.45 was converging toward zero as the number of 2DZMs was increased. For the power spectrum, the RMSE was 59% (1 2DZM), 33% (10 2DZMs), and 25% (20 2DZMs).

In conclusion, the simulation analysis in this section was important because it showed that the correlation coefficient could be estimated using small numbers of 2DZMs relative to the number of 2DZMs needed to complete a 3DZM analysis. The variance for the estimated power spectra was significantly higher compared to the correlation coefficient variance. However, increasing the number of 2DZMs did decrease power spectral estimate variance. These findings provide further evidence that when working with 2DZMs, it may be better to analyze the correlation coefficient instead of the power spectrum.

4.8 Acoustic simulations

Acoustic theory for scattering by a fluid sphere predicts that the BSC for a collection of same sized spheres will be weighted by the sphere radius raised to a power [12]. If a medium is filled with spheres having different radii, larger

size spheres will have a greater contribution to the estimated backscatter coefficient compared to smaller sized spheres. When interpreting scatterer size estimates for a polydisperse collection of fluid spheres, the scatterer size will be biased toward the larger spheres. The goal of this section is to present analytic developments and simulation results demonstrating that the same weighting is present when conducting impedance map analysis. Simulations were conducted to relate analytic predictions, 3DZM analysis, 2DZM analysis, and pulse-echo simulations.

4.8.1 Ultrasonic backscatter coefficient for spheres having different sizes: Volume defined in terms of the region where echoes originate

The backscattering cross section for a single fluid spheres is [22]

$$\sigma_{BCS}(k,a) = \frac{4\pi}{9}(\gamma_\kappa - \gamma_\rho)^2 k^4 a^6 \left(\frac{3}{2ka} j_1(2ka)\right)^2. \tag{4.6}$$

For a scattering volume containing N spheres, the incoherent component of the BSC can be written as a summation of scattering cross sections

$$\sigma(k) = \frac{1}{4\pi}\frac{1}{V}\sum_{i=1}^{N} \sigma_{BCS}(k,a_i) \tag{4.7}$$

where in this approach the scattering volume is defined as

$$V = \sum_{i=1}^{N} \frac{4}{3}\pi a_i^3. \tag{4.8}$$

There are two random variables in Eqs. 4.7 and 4.8, including the sphere radius, A, and the number of scatterers in the ensemble of scatterers, N. Evaluating the ensemble average of the BSC in Eq. 4.7 is difficult, but several approximations can be made to derive a simple expression. First, note that

$$\lim_{N\to\infty} \frac{1}{N}\sum_{i=1}^{N} \sigma_{BCS}(k;a_i) = \int_0^\infty p(a)\sigma_{BCS}(k;a)\mathrm{d}a = E[\sigma_{BCS}(k;A)] \tag{4.9}$$

where $p(a)$ is the probability distribution for the random variable A, the sphere radius. Likewise, for the volume term in Eq. 4.8

$$\lim_{N\to\infty}\frac{1}{N}\sum_{i=1}^{N}\frac{4}{3}\pi a_i^3 = \frac{4}{3}\pi\int_0^\infty p(a)a^3\mathrm{d}a = \frac{4}{3}\pi E[A^3]. \tag{4.10}$$

Therefore, for large enough N, the following approximate expression for the BSC exists:

$$\sigma(k) \approx \frac{1}{4\pi}\frac{E[\sigma_{BCS}(k;A)}{\frac{4}{3}\pi E[A^3]} \tag{4.11}$$

$$= \frac{1}{4\pi}\frac{\int_0^\infty p(a)\sigma_{BCS}(k;a)\mathrm{d}a}{\frac{4}{3}\pi\int_0^\infty p(a)a^3\mathrm{d}a} \tag{4.12}$$

$$= \frac{1}{4\pi}\frac{1}{\frac{4}{3}\pi E[A^3]}\frac{1}{9}(\gamma_\kappa-\gamma_\rho)^2\left[k^4\int_0^\infty p(a)a^6\left(\frac{3}{2ka}j_1(2ka)\right)^2\mathrm{d}a\right] \tag{4.13}$$

Several observations can be made from Eq. 4.13. First, this equation does not depend on the number of spheres in the ensemble. For example, if the number of spheres is doubled, the same BSC results. Second, the fluid sphere form factor is weighted by the sphere radius raised to the sixth power. When estimating scatterer sizes, the shape of the BSC is controlled by the terms inside the square brackets in Eq. 4.13. The terms outside the bracket only affect the magnitude of the BSC and therefore have no effect when estimating scatterer sizes based on Eq. 4.13.

4.8.2 Ultrasonic backscatter coefficient for spheres having different sizes: Volume defined in terms of a measurement region

For a scattering volume containing N spheres, the incoherent component of the BSC can be written as a summation of scattering cross sections as in Eq. 4.7, except that the volume V is the volume associated with a measurement apparatus, e.g., the focal region of a transducer. In this case, assuming large enough N such that Eq. 4.9 applies, the BSC is

$$\sigma(k) \approx \frac{1}{4\pi}\frac{N}{V}E[\sigma_{BCS}(k;A)] \tag{4.14}$$

$$= \frac{1}{4\pi}\frac{N}{V}\int_0^\infty p(a)\sigma_{BCS}(k;a)\mathrm{d}a. \tag{4.15}$$

Taking an ensemble average of the BSC produces the following expression:

$$\langle\sigma(k)\rangle = \frac{1}{4\pi}\frac{E[N]}{V}\,E[\sigma_{BCS}(k;a)] \tag{4.16}$$

$$= \frac{\bar{n}}{4\pi}\int_0^\infty p(a)\sigma_{BCS}(k;a)\mathrm{d}a \tag{4.17}$$

$$= \frac{1}{9}\bar{n}(\gamma_\kappa-\gamma_\rho)^2\left[k^4\int_0^\infty p(a)a^6\left(\frac{3}{2ka}j_1(2ka)\right)^2\mathrm{d}a\right] \tag{4.18}$$

where $\bar{n}$ is the average number of spheres per unit measurement volume. Several observations can be made from Eq. 4.18. First, this equation does depend on the number of spheres in the ensemble. For example, if the number of spheres is doubled, the BSC doubles. Second, the fluid sphere form factor is weighted by the sphere radius raised to the sixth power. Finally, when estimating scatterer sizes, the shape of the BSC is controlled by the terms inside the square brackets in Eq. 4.18. The terms outside the bracket only affect the magnitude of the BSC and therefore have no effect when estimating scatterer sizes based on Eq. 4.18.

Irrespective of the definition of the volume term in Eq. 4.7, i.e., using Eq. 4.13 or 4.18, the fluid sphere form factor is weighted by the sphere radius raised to the sixth power. In other words, the terms that affect scatterer size estimates, i.e., the terms on the inside of the square brackets in Eqs. 4.13 and 4.18, are the same for Eqs. 4.13 and 4.18.

4.8.3 Impedance maps of spheres with different sizes

For a single sphere at the origin and having radius a, the function describing the relative changes in compressibility and density is given by

$$\gamma_{sphere}(r,a) = \begin{cases} \gamma_\kappa-\gamma_\rho, & r\le a \\ 0, & r>a \end{cases} \tag{4.19}$$

where γ_κ is the relative compressibility inside the sphere and γ_ρ is the relative density inside the sphere. The Fourier transform of this function is given by

$$\Gamma_{sphere}(k,a) = (\gamma_\kappa - \gamma_\rho)V_a \left(\frac{3}{ka} j_1(ka)\right) \tag{4.20}$$

where $V_a = 4/3\pi a^3$ and the magnitude squared of the Fourier transform is given by

$$|\Gamma_{sphere}(k,a)|^2 = (\gamma_\kappa - \gamma_\rho)^2 V_a^2 \left(\frac{3}{ka} j_1(ka)\right)^2. \tag{4.21}$$

For an ensemble of N spheres having different sizes, the spatial map describing the relative changes in density and compressibility and having unit volume can be written in terms of Eq. 4.19 as

$$\gamma(\mathbf{r}) = \sum_{i=1}^{N} \gamma_{sphere}(\mathbf{r} - \mathbf{r}_i, a_i) \tag{4.22}$$

where $\mathbf{r}_i$ is the center of the ith sphere and a_i is the radius of the ith sphere. The Fourier transform for this function is given by

$$\Gamma(\mathbf{k}) = \sum_{i=1}^{N} \Gamma_{sphere}(\mathbf{k}, a_i) e^{-j\mathbf{k}\cdot\mathbf{r}_i}. \tag{4.23}$$

By averaging over many realizations of $\gamma(\mathbf{r})$, the coherent component can be ignored and the average magnitude squared of the Fourier transform can be approximated as

$$\left\langle |\Gamma(k)|^2 \right\rangle \approx N \int_0^\infty p(a)\, |\Gamma_{sphere}(k,a)|^2 \mathrm{d}a \tag{4.24}$$

$$= N(\gamma_\kappa - \gamma_\rho)^2 \frac{16\pi^2}{9} \left[\int_0^\infty p(a) a^6 \left(\frac{3}{ka} j_1(ka)\right)^2 \mathrm{d}a\right] \tag{4.25}$$

and multiplying by k^4 and accounting for pulse echo propagation produces:

$$k^4 \left\langle |\Gamma(2k)|^2 \right\rangle = N(\gamma_\kappa - \gamma_\rho)^2 \frac{16\pi^2}{9} \left[k^4 \int_0^\infty p(a) a^6 \left(\frac{3}{2ka} j_1(2ka)\right)^2 \mathrm{d}a\right]. \tag{4.26}$$

When estimating scatterer sizes based on Eq. 4.26, the only terms affecting

the scatterer size estimates are on the inside of the square brackets in Eq. 4.26. Comparing the terms inside the square brackets for Eqs. 4.13, 4.18, and 4.26 shows that all of them are identical and include the fluid sphere form factor weighted by the sphere radius raised to the sixth power.

4.8.4 Simulations

Simulations were conducted to demonstrate the equivalence in the estimation of scatterer size between impedance map approaches and acoustic approaches when propagating a plane wave through a medium with spheres of polydisperse sizes. Specifically, analytic acoustic expressions and impedance map analysis predict an acoustic weighting of the radius to the sixth power.

Description

A cube having side length 300 μm was filled with spheres. The sphere diameters were random following a Gaussian distribution with mean 30 μm. The ratio between the standard deviation and the mean of the Gaussian distribution was varied as $\sigma/\mu = 0.1, 0.2, 0.3, 0.4$. The number density for the spheres was $3,000/\text{mm}^3$ for a volume fraction of approximately 4%. The spheres were placed randomly and independently of each other. A total of 500 collections of spheres were simulated for each σ/μ ratio. For each collection of spheres, a 3DZM and 2DZM analysis was conducted and pulse echo data was also generated from the volume by propagating an acoustic pulse into the media.

3DZM analysis

For each collection of spheres, a 3DZM was generated. The 3DZM spatial sampling rate was 0.46 μm by 0.46 μm by 3.0 μm, such that the number of grid points in the 3DZM was 650 by 650 by 100, which is the same as the rabbit liver 3DZMs discussed in the next chapter. The 3D power spectrum was computed for each 3DZM using the squared magnitude of the Fourier transform and radial averaging was used to reduce this function to a 1D function of spatial frequency. These power spectra were averaged across the 50 collections of spheres and scatterer sizes were estimated using this power

spectrum utilizing the range $0.5 < ka < 1.2$ and a fluid sphere model. The simulation was then repeated 10 times. This analysis was repeated for each σ/μ ratio and the results are shown in Fig. 4.46.

2DZM analysis

For each collection of spheres, a 2DZM was generated by extracting a single slice from the volume of spheres. The 2DZM spatial sampling rate was 0.46 μm by 0.46 μm. The slice was extracted from the x,y-plane and from the middle of a 3DZM volume along the z-axis and a 2D correlation function was computed for the extracted slice. For a particular ratio σ/μ, the correlation functions from each of the 50 volumes were averaged. A power spectrum was found from this correlation function and scatterer sizes were estimated using this power spectrum utilizing the range $0.5 < ka < 1.2$ and a fluid sphere model. The simulation was then repeated 10 times. The scatterer size estimates from the 2DZM analysis are shown in Fig. 4.46.

Pulse echo simulations

For a particular collection of spheres, a pulse was propagated through the collection of spheres and used to generate RF pulse echo data. The medium was lossless and the speed of sound was set to 1500 m/s. For these simulations, the spatial sampling rate was 0.46 μm by 0.46 μm by 0.46 μm, such that the number of grid points in the volume was 650 by 650 by 650. For each collection of spheres, a pulse was used to generate RF data for the medium. The pulse consisted of a Gaussian modulated sinusoid with center frequency 13.5 MHz and 80% fractional bandwidth. A pulse with these frequency characteristics corresponded to the range $0.5 < ka < 1.2$ based on the mean sphere size. A Gaussian beam with -6-dB beam width of 100 μm was applied to the medium orthogonal to the pulse propagation. The power spectrum was normalized by the frequency response of the pulse before estimating scatterer sizes. For each ratio σ/μ, 50 power spectra were averaged to reduce the effects of spatial variation noise. Scatterer size estimates were made using the averaged normalized power spectrum. The simulation was repeated 10 times and results are shown in Fig. 4.46.

Analytic predictions #1

For the examined ratios $\sigma/\mu = 0.1, 0.2, 0.3, 0.4$, an analytic BSC was computed using Eq. 4.18 and used to estimate the scatterer size utilizing the range $0.5 < ka < 1.2$. The scatterer size estimates based on this analytic expression for the BSC are shown in Fig. 4.46.

Analytic predictions #2

Let A be the random variable for the sphere radius which has probability distribution $p(a)$. The mean for the random variable A is μ and the standard deviation is σ. A new probability distribution is formed by multiplying $p(a)$ by the weighting term $(a/\mu)^n$

$$p_n(a) = (a/\mu)^n p(a)/C \tag{4.27}$$

where C is a normalization constant such that $p_n(a)$ integrates to one. Integrating $p_n(a)$ in this way gives

$$1 = \int_{-\infty}^{\infty} p_n(a)\mathrm{d}a = \int_{-\infty}^{\infty} (a/\mu)^n p(a)/C\mathrm{d}a \tag{4.28}$$

$$= \frac{1}{\mu^n C}\int_{-\infty}^{\infty} a^n p(a)\mathrm{d}a = \frac{1}{\mu^n C}E[A^n] \tag{4.29}$$

where

$$E[A^n] = \int_{-\infty}^{\infty} a^n p(a)\mathrm{d}a \tag{4.30}$$

and solving for C gives

$$C = E[A^n]/\mu^n. \tag{4.31}$$

Inserting Eq. 4.31 into Eq. 4.27 gives

$$p_n(a) = \frac{a^n}{E[A^n]}p(a). \tag{4.32}$$

Next, the expected (mean) value for the new probability distribution $p_n(a)$ is given by

$$\mu_n = \int_{-\infty}^{\infty} a \; p_n(a) \mathrm{d}a \tag{4.33}$$

$$= \int_{-\infty}^{\infty} a \; \frac{a^n}{E[A^n]} p(a) \mathrm{d}a \tag{4.34}$$

$$= \frac{1}{E[A^n]} \int_{-\infty}^{\infty} a^{n+1} p(a) \mathrm{d}a \tag{4.35}$$

$$= \frac{E[A^{n+1}]}{E[A^n]} \tag{4.36}$$

where the non-central moments in Eq. 4.36 are given by Eq. 4.30.

Discussion

Several observations can be made from Fig. 4.46 and Table 4.1. First, as the ratio σ/μ increased, the estimated scatterer size increased for both the 3DZM and 2DZM analysis, suggesting that the scatterer size estimates were being biased toward the large size scatterers. This finding has been described previously for acoustic experiments [22, 42] and for 3DZM analysis [17]. Second, scatterer sizes estimated using 3DZMs, 2DZMs, and pulse echo data agreed with the analytic predictions discussed in the analytic predictions #1 section above (which uses Eq. 4.18) to within 2%, 2%, and 3%, respectively. Third, the scatterer sizes estimated from BSCs generated using Eq. 4.18 (analytic predictions #1) produced lower RMSE values compared to the analytic predictions of Eq. 21 (analytic predictions #2). Fourth, when comparing the two predictions from the analytic predictions #2 section, the prediction using n=4 was more accurate for the 2DZM results and the 3DZM results compared to using the prediction when using n=3. For the pulse echo simulations, n=3 and 4 had the same RMSE.

4.9 Conclusions

In this chapter, simulated media having correlation coefficients and power spectra with different shapes were used to demonstrate that estimation of the correlation coefficient and power spectrum of a 3D random process was possible with low error using 2DZMs. The simulations in this section demon-

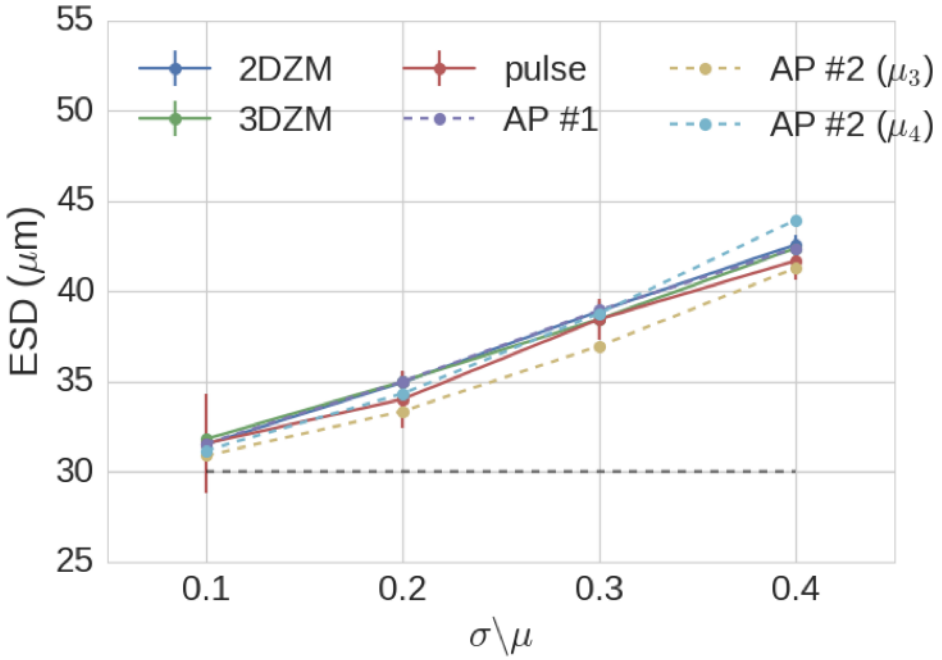

Figure 4.46: Estimated scatterer size as a function of the ratio σ/μ. The solid blue line represents scatterer sizes estimated from 2DZMs. The solid green line represents scatterer sizes estimated using 3DZMs. The solid red line represents scatterer sizes from the generated pulse echo data. The dashed red line represents scatterer sizes estimated from BSCs generated from the analytic expression in Eq. 4.18 and corresponds to the analytic predictions #1 section above. The dashed tan and dashed light blue lines represent scatterer sizes based on the analytic expression in Eq. 4.36 and with n=3 and 4, respectively. These lines correspond to the analytic predictions #2 section above.

Table 4.1: RMSE (μm) between scatterer size estimates based on simulations and AP (analytic predictions) #1 and AP #2.

	AP #1	AP #2 (μ_2 in Eq. 4.36)	AP #2 (μ_3 in Eq. 4.36)
3DZM	0.51	1.5	0.9
2DZM	0.46	1.4	1.0
pulse echo	1.9	2.0	2.0

strated that such analysis was possible using media having known correlation coefficients and power spectra. Such analysis is possible from a theoretical stand point; however, it was not known if the analysis would be possible at practical scales (i.e., massively sized 2DZMs were not needed relative to 3DZM size). In addition, previous work in this area did not validate that estimation of a correlation coefficient and power spectrum was possible using 2DZMs, except by using analytic expressions.

The sparse scatterer simulations demonstrated that 2DZMs were able to capture size and shape information about a 3D random process. Most importantly, the number of object cross sections needed to capture this information was small (i.e., less than 30). The results provide guidance when analyzing histology with sparse collections of objects such as cell nuclei. In this case, the number of nuclei in a 2DZM could be counted to determine if the 2DZM had sufficient size. The results from the sparse scatterer simulations also suggest that gains could be made by using regularly spaced slices, particularly in the case of spherical objects. However, when increasing slice thickness, the advantages of using regularly spaced slices largely disappeared.

The sparse anisotropic simulations demonstrated that in some cases it was possible to relax the isotropy assumption used to develop the 2DZM method. In this case, it was necessary for the 2DZM slice plane to be parallel to the ultrasound propagation direction. When this condition was satisfied, correlation coefficient and power spectral estimation was possible with low error using 2DZMs.

The spherical Gaussian simulations demonstrated that the 2DZM method worked for continuous media. These simulations examined the effect of 2DZM size on the estimated correlation coefficient and power spectrum. The results showed that biased correlation coefficient and power spectral estimates resulted when using 2DZMs that were too small. More importantly, the results showed that non-biased estimates resulted when using 2DZMs that were not excessively larger than the scatterer. For example, the results showed that when using a 2DZM that was 50 times larger than the scatterer, unbiased correlation coefficient and power spectral estimates were possible. Using a 2DZM that is this large compared to the scatterer is not a limitation of 2DZM analysis. Furthermore, the analysis showed that correlation coefficient and power spectrum could be estimated using small numbers of 2DZMs relative to the numbers of 2DZMs required to conduct 3DZM analysis. For example,

the coefficient of variation of scatterer size estimates based on the correlation coefficient was less than 2% when using 10 2DZMs. In addition, the results suggested that the correlation coefficient produced lower error scatterer size estimates, both in terms of bias and variance, compared to estimates based on the power spectrum. These findings suggest that modeling the correlation coefficient may be better than modeling the power spectrum when conducting ZM analysis.

The dense sphere simulations were significant because they demonstrated that 2DZMs could capture information about the 3D spatial positions of the scatterers in addition to information about the size and shape of the scatterers. Similar to the spherical Gaussian simulations, it was found that using too small a 2DZM resulted in biased correlation coefficient and power spectral estimates. However, using a 2DZM that was 25 times the size of the spheres resulted in unbiased estimates. While it was possible to estimate correlation coefficient and power spectrum in an unbiased manner, the analysis of variance results demonstrated that the power spectral estimates were sensitive to small errors in the correlation coefficient estimate. These findings add further support to the suggestion that the correlation coefficient should be modeled instead of the power spectrum when conducting 2DZM analysis, especially when conducting analysis of dense media.

In general, the simulations in this chapter provide substantial evidence that the 2DZM approach works in practice. The 2DZM method should work from a theoretical perspective, but the simulation results demonstrated that 2DZM analysis did not require additional constraints relative to 3DZM analysis. For example, it was not necessary to significantly increase 2DZM size relative to 3DZM size to obtain results with low error. Verification of the 2DZM method on media having known correlation coefficient and power spectrum has never been previously conducted. These simulation results show that the 2DZM method can be used to model scattering, that is it possible to estimate the correlation coefficient and power spectrum for different kinds of random media, and that one can have confidence in the 2DZM method when using it to analyze ZMs with unknown correlation coefficients and power spectra.

CHAPTER 5

ANALYSIS OF IMPEDANCE MAPS CREATED FROM HISTOLOGY

5.1 Rabbit liver

5.1.1 Description of ZM construction

The 2DZM analysis procedure was applied to a set of ZMs constructed from the livers of New Zealand white rabbits. The 3DZMs used in this study were constructed by Pawlicki et al. and used with their permission [20]. In that study, the 3DZM analysis suggested that the cell nucleus was a primary source of scattering in liver.

The process that Pawlicki et al. used to construct the ZMs used in this study can be found in [20, 36] and is reviewed here briefly. Lobes of normal liver from New Zealand white rabbits were excised, chemically fixed in formalin, sliced into 3 μm sections, stained with hematoxylin and eosin (H&E), and prepared as standard histology slides. Each slide was digitized using a NanoZoomer HT slide scanner (Hamamatsu, Hamamatsu City, Japan) at a pixel resolution of 0.46 μm. An example histology image from the rabbit liver is in Fig. 3.2 (a).

A total of 24 3DZMs were created at different spatial locations from the excised liver sample using the process described in Sec. 3.1. Impedance values were assigned according to Table 3.1. The created 3DZMs were cubes having side length 300 μm. The resolution along the x- and y-axes was 0.46 μm and the resolution along the z-axis was 3 μm. An example 2DZM created from the rabbit liver is in Fig. 3.2 (b).

In addition to the healthy rabbit liver, the above process was repeated using a fatty rabbit liver with a measured fat content of 14.6% [20]. A total of 24 3DZMs were created from the fatty liver.

In this study, analysis of bias and analysis of variance were conducted to

study error in the estimated correlation coefficient and power spectrum in the healthy rabbit liver. These studies were used to determine a minimum size 2DZM that was needed to reduce bias and the number of 2DZMS that were needed to reduce variance. In addition, a study was conducted to demonstrate that 2DZM analysis can be used in place of 3DZM analysis to detect differences between two rabbit livers, one healthy and one fatty, and to quantitatively characterize the agreement between scatterer sizes estimated using 2DZMs and 3DZMs for the examined rabbit livers.

5.1.2 2DZM size

The liver ZMs were used to complete an analysis of bias for correlation coefficients and power spectra estimated using 2DZMs. To study the bias in the estimated correlation coefficients, the variance was eliminated by averaging large numbers of 2DZMs. Specifically, the correlation coefficient was estimated from every 2DZM from every rabbit liver 3DZM in this study such that a total of $100 \times 24 = 2,400$ 2DZMs were used to estimate the correlation coefficient. Five different 2DZM sizes were studied. The 2DZM sizes were given in terms of the 2DZM side length L. The studied 2DZM sizes included $L = 300.0$ μm, $L = 150.0$ μm, $L = 75.0$ μm, $L = 37.5$ μm, and $L = 18.75$ μm. The correlation coefficient estimated using $L = 300.0$ μm served as the reference for the analysis. If the correlation coefficients estimated using 2DZM size $L = 150.0$ μm, $L = 75.0$ μm, $L = 37.5$ μm and $L = 18.75$ μm converged to the correlation coefficient estimated using 2DZM size $L = 300.0$ μm, this served as evidence that the 2DZM size $L = 300.0$ μm was sufficient to estimate the correlation coefficient without bias. In addition, if only small differences existed between 2DZMs with size $L = 300.0$ μm and smaller sized 2DZMs, these smaller sized 2DZMs could also be said to be unbiased. The same study was repeated, except that each correlation coefficient was used to estimate a power spectrum and a sufficient 2DZM size to estimate the power spectrum was determined.

The estimated correlation coefficients and power spectra for each of the studied 2DZM sizes are in Fig. 5.1. The RMSE between estimated and reference correlation coefficients for the different sized 2DZMs are shown in Fig. 5.2. The RMSE between estimated and reference power spectra is also

shown in Fig. 5.2. Scatterer sizes were estimated using the correlation coefficients from Fig. 5.1. The fluid-filled sphere model in Eq. 2.18, spherical Gaussian model in Eq. 2.20, and exponential model in Eq. 2.23 were used to model the correlation coefficients and it was determined that the exponential model provided the best fit. The reference scatterer size was estimated from the reference correlation coefficient (i.e., the correlation coefficient estimated using 2DZM with size $L = 300.0$ μm) and the estimated effective scatterer diameter was 8.8 μm. The percentage error between the estimated and reference scatterer sizes as a function of 2DZM size is shown in Fig. 5.3. Scatterer sizes were also estimated using the power spectra from Fig. 5.1 and the exponential model, the results of which are shown in Fig. 5.3. The estimated effective scatterer diameter based on the power spectrum was 7.6 μm.

The results in Fig. 5.1 show the effect of 2DZM size when estimating the correlation coefficient. The RMSE between the estimated and reference correlation coefficients was 0.4% (2DZM size: $L = 150.0$ μm), 1.0% (2DZM size: $L = 75.0$ μm), 2.8% (2DZM size: $L = 37.5$ μm), and 10% (2DZM size: $L = 18.75$ μm). These results suggest that the rabbit liver correlation coefficient estimates were unbiased when using a size of $L = 150.0$ μm and $L = 75.0$ μm and that they were biased when using a size of $L = 18.75$ μm. The RMSE curves in Fig. 5.2 show rapid convergence to zero, suggesting that increasing the 2DZM size would offer only minimal reductions in error due to bias.

The results in Fig. 5.1 show the effect of 2DZM size when estimating the power spectrum. The RMSE between the estimated and reference correlation coefficients was 1.2% (2DZM size: $L = 150.0$ μm), 1.4% (2DZM size: $L = 75.0$ μm), 4.4% (2DZM size: $L = 37.5$ μm), and 33% (2DZM size: $L = 18.75$ μm). These results suggest that the rabbit liver power spectral estimates were unbiased when using a size of $L = 150.0$ μm and $L = 75.0$ μm and that they were biased when using a size of $L = 18.75$ μm.

Similar to the spherical Gaussian simulations, the rabbit liver correlation coefficient was underestimated when using 2DZMs that were too small. The scatterer size based on the estimated correlation coefficient was also underestimated when using 2DZMs that were too small. The percent error in scatterer size estimate based on the correlation coefficient was -1.9% (2DZM size: $L = 150.0$ μm), -4.1% (2DZM size: $L = 75.0$ μm), -12% (2DZM size:

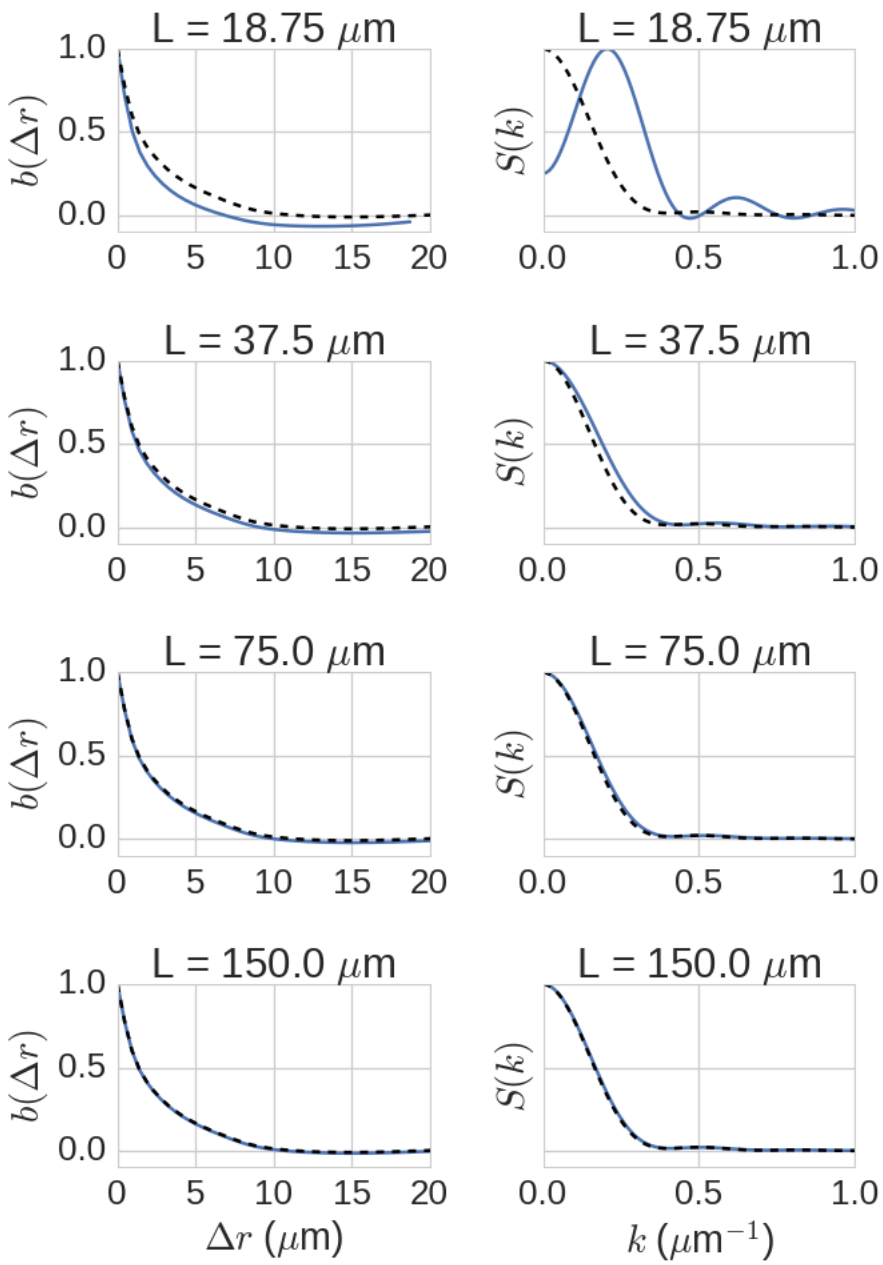

Figure 5.1: Examples of (left column) correlation coefficient and (right column) power spectrum estimated using different sized 2DZMs. The dashed black line represents the correlation coefficient or power spectrum estimated using $L = 300.0$ μm.

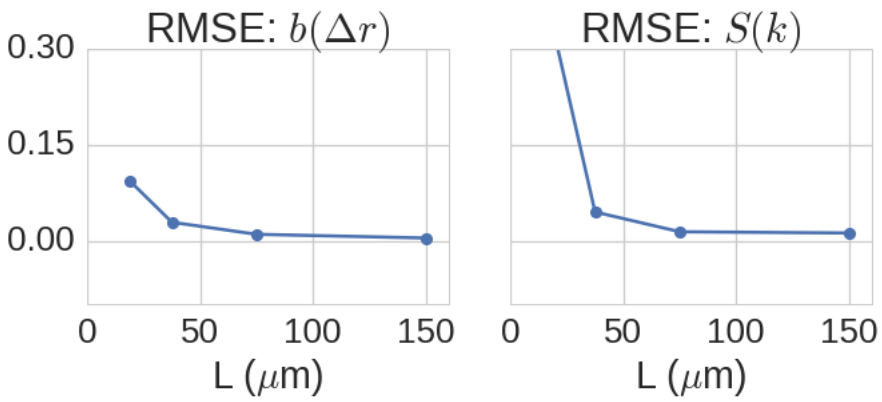

Figure 5.2: RMSE for estimated (left column) correlation coefficients and (right column) power spectrum as a function of 2DZM size.

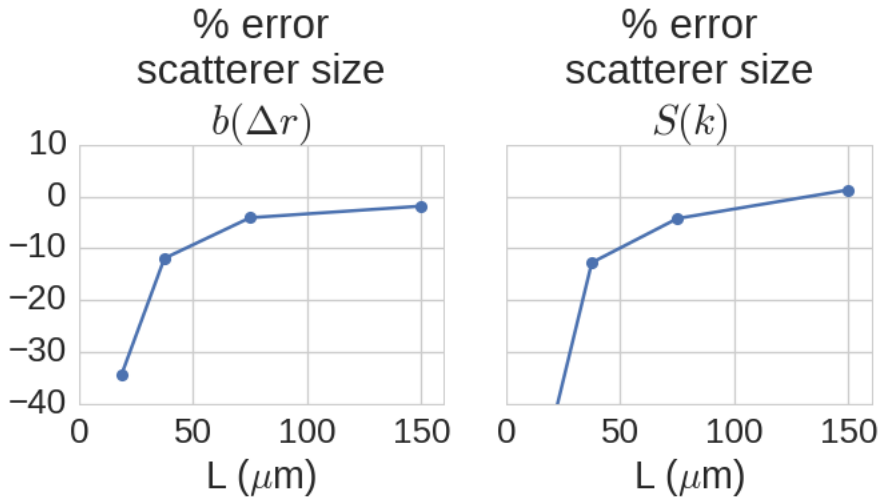

Figure 5.3: Percentage error in estimated scatterer size using the (left column) correlation coefficients and (right column) as a function of 2DZM size.

$L = 37.5$ μm), and -34% (2DZM size: $L = 18.75$ μm). The percent error in scatterer size estimate based on the power spectrum was 1.3% (2DZM size: $L = 150.0$ μm), -4.2% (2DZM size: $L = 75.0$ μm), -13% (2DZM size: $L = 37.5$ μm), and -47% (2DZM size: $L = 18.75$ μm).

In conclusion, this section demonstrated how to analyze bias for a collection of 2DZMs created from rabbit liver. The actual correlation coefficient and scatterer size were unknown for this medium. The results suggested that 2DZM with size $L = 150.0$ μm was sufficient to reduce or eliminate bias because the correlation coefficient and power spectrum RMSE were less than 1% and the percent error in scatterer size estimates was less than 3%.

5.1.3 Number of 2DZMs

To study the variance in the estimated correlation coefficient, the bias was eliminated by using 2DZMs having size $L = 300.0$ μm. The results from the previous section suggested that 2DZMs with this size exhibited minimal bias. The variance of an estimated correlation coefficient is controlled by the number of 2DZMs that are used to estimate the correlation coefficient. Using more 2DZMs to estimate the correlation coefficient results in decreased correlation coefficient variance. Therefore, the analysis in this section consisted of changing the number of 2DZMs used to estimate the correlation coefficient in order to study correlation coefficient variance.

In order to study correlation coefficient variance, the following process was used. First, one 2DZM was randomly selected from the collection of 24 rabbit liver 3DZMs. Each rabbit liver 3DZM had 100 2DZMs, so there were a total of $100 \times 24 = 2,400$ 2DZMs available for selection. This 2DZM was used to estimate the correlation coefficient. The RMSE between the estimated and reference correlation coefficients were computed. The reference correlation coefficient was found by estimating the correlation coefficient using all available $2,400$ 2DZMs and using 2DZM size $L = 300.0$ μm. The scatterer size was estimated from the estimated correlation coefficient using the exponential model. This scatterer size was compared to the reference scatterer size, which was estimated from the reference correlation coefficient. This process was repeated 100 times, that is, for 100 different randomly selected 2DZMs.

Next, ten 2DZMs were randomly selected from the available rabbit liver

2DZMs. The correlation coefficient was estimated using these ten 2DZMs. RMSE values were computed for the estimated correlation coefficient. Scatterer sizes were computed using the estimated correlation coefficient. This process was repeated 100 times, that is, for 100 different sets of ten randomly selected 2DZMs.

The above processing steps were repeated but using sets of $20, 30, ..., 100$ randomly selected 2DZMs from the available rabbit liver 2DZMs. In this way, the correlation coefficient RMSE and estimated scatterer size could be studied as a function of the number of 2DZMs used to estimate the correlation coefficient. Because the 2DZMs were randomly selected from the available $2,400$ 2DZMs, the 2DZMs were independent. In addition, because the size of the 2DZMs was $L = 300.0$ μm, it was assumed that observed errors were due to variance in the estimates and not due to bias. The same study was repeated except that the power spectrum was estimated from each studied correlation coefficient.

Examples of correlation coefficients and power spectra that were estimated using different numbers of 2DZMs are in Fig. 5.4. The RMSE between estimated and reference correlation coefficients are in Fig. 5.5. The RMSE between estimated and reference power spectra are in Fig. 5.5. Scatterer sizes were estimated from the correlation coefficients and power spectra in Fig. 5.4. The percent differences between the estimated and reference scatterer sizes as a function of the number of 2DZMs used to estimate the correlation coefficient are shown in Fig. 5.6. In addition, the coefficients of variation of the estimated scatterer sizes as a function of the number of 2DZMs used to estimate the correlation coefficient are shown in Fig. 5.6.

In the previous section, it was shown that 2DZMs having sufficient size could be used to estimate the correlation coefficient without bias. However, large numbers of 2DZMs were used to estimate that correlation coefficient. The results in Fig. 5.4 are important because they demonstrate that small numbers of 2DZMs could be used to estimate the same correlation coefficient that large numbers of 2DZMs were used to estimate.

From Fig. 5.5, the RMSE for the correlation coefficient decreased rapidly as the number of 2DZMs used to estimate the correlation coefficient was increased. For example, the RMSE between estimated and reference correlation coefficient was 3.7% (1 2DZM), 1.1% (10 2DZMS), 0.9% (20 2DZMs), and 0.8% (30 2DZMs). From Fig. 5.5, the RMSE for the power spectrum

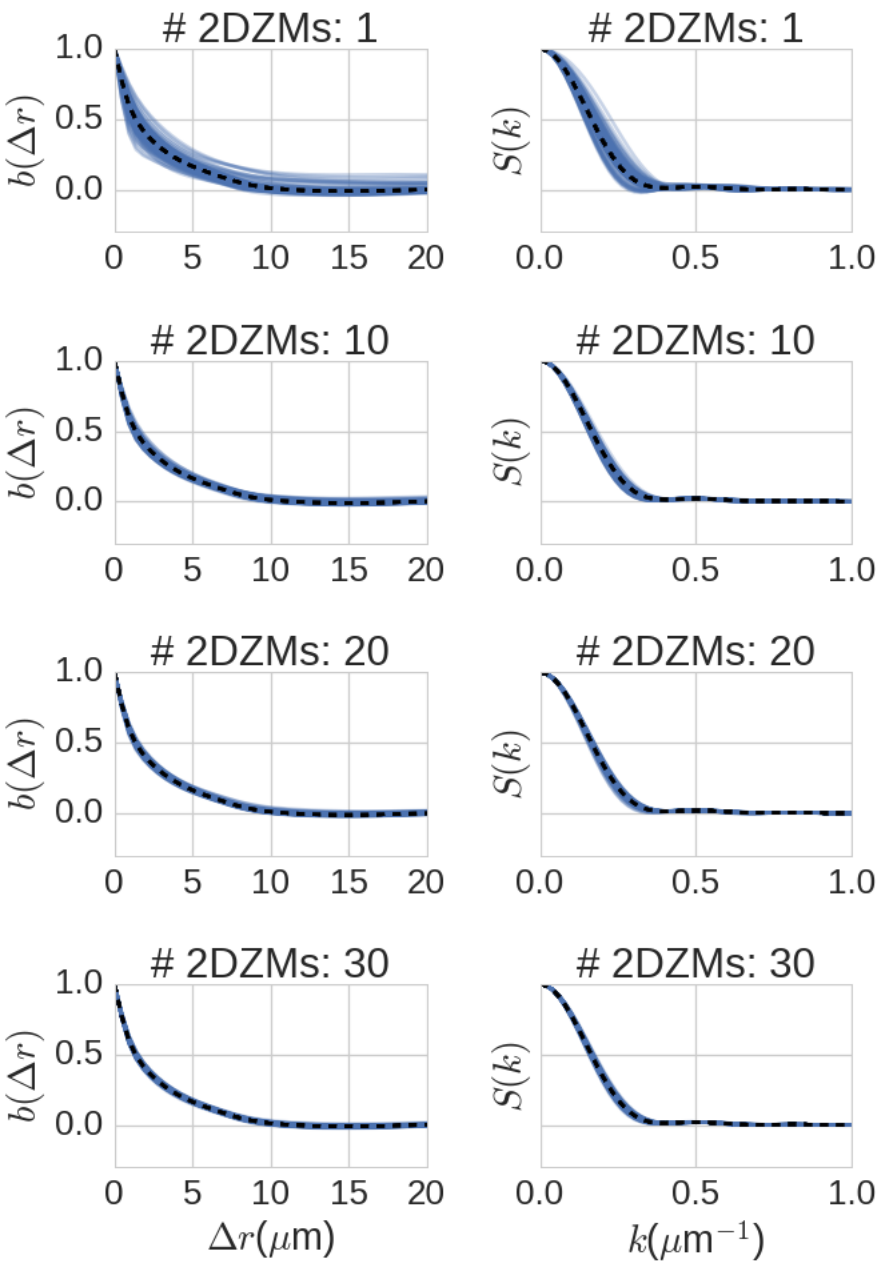

Figure 5.4: Examples of (left column) correlation coefficients and (right column) power spectra estimated using different numbers of 2DZMs. The dashed black line represents the correlation coefficient estimated using $L = 300.0$ μm and all available 2DZMs.

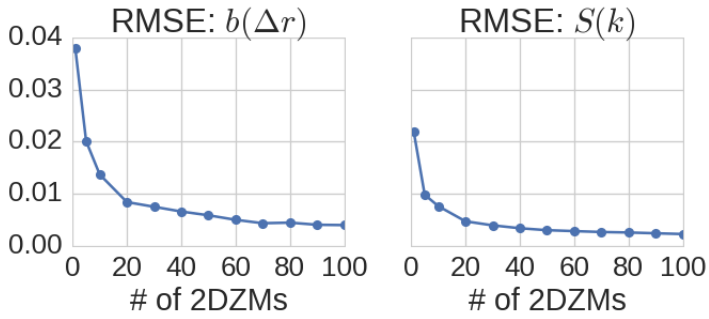

Figure 5.5: RMSE for estimated (left column) correlation coefficients and (right column) power spectra using different numbers of 2DZMs to estimate the correlation coefficient.

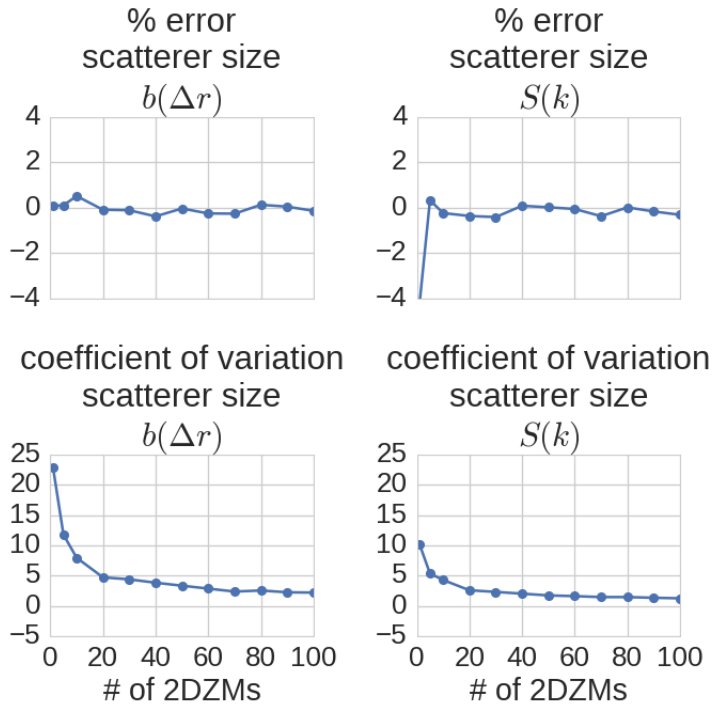

Figure 5.6: The top row is the average percent error in estimated scatterer size based on the (left column) correlation coefficient and (right column) power spectrum using different numbers of 2DZMs. The bottom row is the coefficient of variation for the scatterer size estimates using different numbers of 2DZMs.

decreased rapidly as the number of 2DZMs used to estimate the correlation coefficient was increased. The RMSE between estimated and reference power spectrum was 1.7% (1 2DZM), 0.6% (10 2DZMs), 0.5% (20 2DZMs), 0.4% (30 2DZMs). These results suggest that estimation of the correlation coefficient and power spectrum with low error was possible using a small subset of the 2DZMs that would be required to conduct a 3DZM analysis.

From Fig. 5.6, the mean percent difference in scatterer size estimates was close to zero and independent of the number of 2DZMs used to estimate the correlation coefficient, suggesting that the scatterer size estimates were unbiased. Furthermore, the coefficient of variation for the scatterer size estimates decreased as the number of 2DZMs used to estimate the correlation coefficient was increased. For example, the coefficient of variation for the scatterer size based on the correlation coefficient was 24% (1 2DZM), 5.9% (10 2DZMs), 5.5% (20 2DZMs), and 4.6% (30 2DZMs). The coefficient of variation for the scatterer size based on the power spectrum was 8.6% (1 2DZM), 3.5% (10 2DZMs), 2.8% (20 2DZMs), and 2.5% (30 2DZMs). A small coefficient of variation indicates that the estimated scatterer size will be close to the reference scatterer size irrespective of the set of 2DZMs used to estimate the correlation coefficient.

In conclusion, the rabbit liver results in this section were important because they demonstrated that the correlation coefficient could be estimated with low error using small numbers of 2DZMs. One of the main advantages of 2DZMs over 3DZMs is that fewer slices need to be used to estimate the correlation coefficient. The results in this section demonstrate that this advantage was realized for the rabbit liver ZMs. The rabbit liver 3DZMs required analysis of 100 2DZMs. The results in this section demonstrated that low error estimation of the correlation coefficient was possible using 30 2DZMs with size $L = 300.0$ μm because the RMSE for the correlation coefficient and power spectrum was less than 1% and the coefficient of variation for the scatterer size estimates was less than 5%.

5.1.4 3DZM and 2DZM scatterer size estimate comparison

The goal of this section was to demonstrate 1) that 2DZM analysis can be used in place of 3DZM analysis to detect differences between two rabbit livers,

one healthy and one fatty, and 2) to quantitatively characterize the agreement between scatterer sizes estimated using 2DZMs and 3DZMs for the examined rabbit livers. To accomplish the first goal, 3DZM analysis was carried out to demonstrate that differences were statistically significant between one normal and one fatty rabbit liver using scatterer size estimates. Next, 2DZM analysis was carried out to show that this difference was also statistically significant using 2DZMs. To accomplish the second goal, a Bland-Altman analysis was conducted to characterize the agreement between scatterer sizes estimated using 3DZMs and 2DZMs.

3DZM analysis

A total of 24 3DZMs for the healthy rabbit liver and 24 3DZMs for the fatty rabbit liver were examined. Correlation coefficients were estimated using the available 3DZMs and used to estimate a power spectrum and then a form factor for each 3DZM. The estimated form factors are in Fig. 5.7 and visual inspection of this figure suggests that a difference existed between normal and fatty liver form factors. The estimated effective scatterer diameter (ESD) using an exponential model was 7.7 ± 0.4 μm and 6.7 ± 0.5 μm for normal and fatty liver, respectively ($p < 10^{-7}$).

2DZM analysis

Using the same collection of 3DZMs, 2DZM analysis was conducted to see if differences between the normal and fatty liver samples were statistically significant. Each rabbit liver 3DZM consists of 100 2DZMs that have been registered and aligned. The 2DZM analysis in this section was performed by extracting a single 2DZM from each 3DZM. Figure 5.8 shows the form factors estimated using a single 2DZM from each 3DZM and visual inspections suggested that a difference existed between normal and fatty liver power spectra. When scatterer sizes were estimated from these form factors, the estimated ESDs using an exponential model were 7.4 ± 0.5 μm and 6.2 ± 0.5 μm for normal and fatty liver, respectively. The healthy and fatty liver scatterer size samples were found to be statistically different ($p < 10^{-7}$).

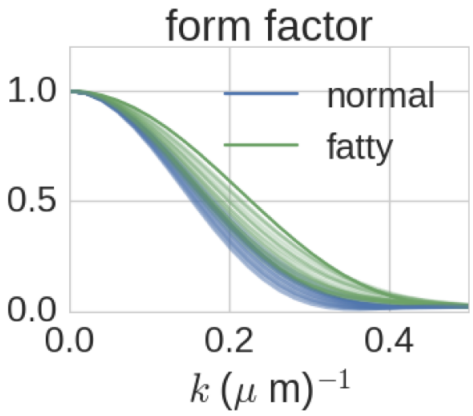

Figure 5.7: Estimated form factors from power spectra for normal (blue) and fatty (green) rabbit liver 3DZMs. Each line represents a single sample.

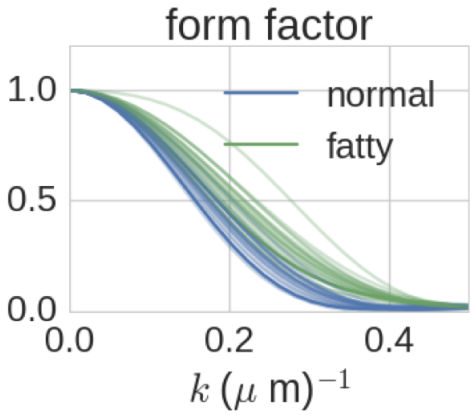

Figure 5.8: Estimated form factors from power spectra for normal (blue) and fatty (green) rabbit liver samples. A single 2DZM was used from each of the available 3DZMs. Each line represents a single sample.

Bland-Altman analysis

To show that there is perfect accuracy between the 2DZM and 3DZM methods would require an infinite amount of data, which is not practical. The goal of this section was to characterize the agreement between the 3DZM and 2DZM methods. This task was accomplished using a Bland-Altman plot with a finite data set, which is a common tool used in medical literature to examine the agreement between two different measurement techniques [43]. The horizontal axis of a Bland-Altman plot shows the mean value of the two measurement techniques and in the absence of a gold standard serves as a best estimate for the true value being measured. The vertical axis of a Bland-Altman plot shows the difference between the two measurement techniques. Presentation of the data in this way allows for identification of systematic differences between the measurement techniques.

A Bland-Altman plot showing the difference between the scatterer size estimated using a 3DZM and the scatterer size using a single 2DZM is in Fig. 5.9. The difference between scatterer sizes was 0.4 ± 0.8 μm, which includes 48 scatterer size estimates from the 48 liver sample impedance maps.

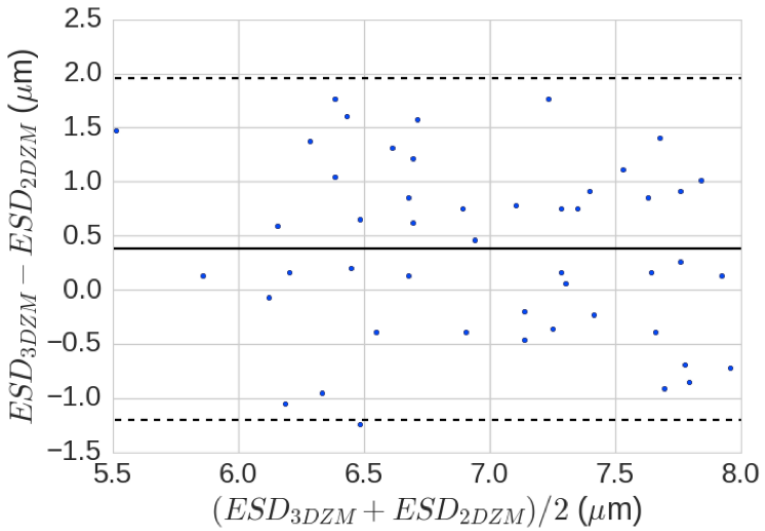

Figure 5.9: Bland-Altman plot showing agreement between scatterer sizes estimated using 3DZMs and scatterer sizes estimated using 2DZMs. The solid black line represents the mean of the differences and the dashed black lines represent 95% limits of agreement.

Discussion

Several observations can be made from the results section. First, statistically significant differences were observed for scatterer size estimates based on a 3DZM analysis for healthy and fatty liver samples. In addition, statistically significant differences were also observed for scatterer size estimates based on a 2DZM analysis. These results demonstrate that it was possible to detect a difference in scatterer size between the healthy liver and fatty livers using 3DZMs and that a 2DZM analysis was able to perform the same task. Second, a Bland-Altman plot was used to study the agreement between scatterer sizes estimated using 3DZMs and 2DZMs. A bias was observed between 3DZM and 2DZM with the finite data set, but the magnitude of the bias would be unlikely to hinder using ZMs to identify acoustic scattering sites.

5.2 Conclusion

The simulation results in Chap. 4 demonstrated that the 2DZM method can model ultrasonic scattering. The results of the 2DZM analysis could be verified because the studied media had known correlation coefficient and power spectrum.

In this chapter, the process for analyzing uncharacterized media was demonstrated. The first step of the 2DZM method was to analyze the bias of the estimated correlation coefficient in the case when the variance was eliminated. This step was completed by eliminating the variance of the correlation coefficient estimate by averaging the correlation coefficient estimates from many 2DZMs. In this way, the correlation coefficient was estimated using differently sized 2DZMs and found to converge to the reference correlation coefficient, which was estimated using 2DZMs with size $L = 300.0$ μm. The analysis suggested that a 2DZM with size $L = 150.0$ μm was sufficient to reduce or eliminate bias because the correlation coefficient and power spectrum RMSE were less than 1% and the percent error in scatterer size estimates was less than 3%.

The second step of the 2DZM method was to analyze the variance of the estimated correlation coefficient in the case when the bias was eliminated. For this step, the bias was eliminated by using 2DZMs with size $L = 300.0$ μm. Next, random sets of 2DZMs (where the number of 2DZMs was varied) were

selected and used to estimate the correlation coefficient. This analysis allowed the correlation coefficient variance to be studied as a function of the number of 2DZMs. The results suggested that small numbers of 2DZMs could be used to estimate the correlation coefficient with low error. The analysis demonstrated that estimation of the correlation coefficient and power spectrum was possible with low error using 30 2DZMs with size $L = 300.0$ μm because the RMSE for the correlation coefficient and power spectrum was less than 1% and the coefficient of variation for the scatterer size estimates was less than 5%. In comparison, a 3DZM analysis would have required 100 2DZMs.

In general, the results in this chapter demonstrated how to perform 2DZM analysis on uncharacterized media. The first step was to determine if an adequately sized ZM is being used to estimate the correlation coefficient. The second step was to determine how many 2DZMs were needed to estimate the correlation coefficient with low variance. The analysis showed that for the rabbit liver ZMs, a reasonable 2DZM size was needed to estimate the correlation coefficient size and small numbers of 2DZMs could be used to estimate the correlation coefficient with low error. This suggested method for analyzing ZMs has not been used previously and should be completed to avoid biased and high variance correlation coefficient estimates.

CHAPTER 6

CONCLUSIONS AND FUTURE WORK

6.1 Summary and contributions

This thesis proposed the 2DZM approach for studying weak acoustic scattering in biological media using stained histological tissue slides. Processing 2DZMs has numerous advantages compared to processing 3DZMs, including reduced computational and financial cost. For example, it is not necessary to register and align 2DZMs before analyzing them. Also, missing slides do not affect 2DZM analysis besides reducing the number of 2DZMs available for analysis.

The 2DZM approach is based on theoretical properties of multi-dimensional random processes. In particular, the correlation functions for an (n-k)-dimensional subspace of an n-dimensional isotropic random process are one and the same. In contrast, the power spectra for an (n-k)-dimensional subspace of an n-dimensional isotropic random process are not the same. Therefore, to estimate the 3D power spectrum from 2D sections of a random process, the following steps were used. First the correlation coefficient was estimated using 2D histology slides. Second, the correlation coefficient was used to estimate the 3D power spectrum.

Although the 2DZM approach is based on theoretical properties of multi-dimensional random processes, the approach has never been validated using media with known correlation coefficient and power spectrum. The sparse scatterer and spherical Gaussian simulations demonstrated that 2DZMs can capture 3D size and shape information about the scatterers in the medium. The dense scatterer simulations demonstrated that 2DZMs can also capture information about the 3D spatial arrangement of the scatterers.

The simulation studies were also designed to offer practical guidance for 2DZM analysis. For example, the simulations were used to determine how

large 2DZMs need to be to estimate correlation coefficients and power spectra with low error, to determine if regularly spaced slices offer any advantages when estimating the correlation coefficient and power spectrum, to determine the effect of appreciable histology section thickness, and to determine the number of 2DZMs that are necessary to achieve a certain reduction in correlation coefficient and power spectral variance. Future ZM analysis can use these results to assess expected bias and variance in the estimated correlation coefficient and power spectrum.

Specifically, the following guidelines can be suggested based on the simulation results. When analyzing 2DZMs where the suspected scatterer is sparse (e.g., cell nuclei), the 2DZM should be made large enough to include at least 30 of the scatterer cross sections. Including this many scatterer cross sections produced correlation coefficient estimates with RMSE less than 0.5% for monodisperse and polydisperse spheres and monodisperse ellipsoids. In addition, the power spectrum RMSE was less than 3 dB for monodisperse spheres and less than 1 dB for polydisperse spheres and monodisperse ellipsoids. When analyzing 2DZMs with continuous variation in acoustic properties, the spherical Gaussian simulations suggest that the 2DZM be at least 50 times larger than the suspected scatterer. For simulated spherical Gaussian media and using 2DZDs with this size, the RMSE of the estimated correlation coefficients and power spectra was less than 1%. When analyzing dense media with 2DZMs, the dense sphere simulations suggest that the 2DZM be at least 25 times larger than the suspected scatterer. For simulated dense spheres and using this 2DZM size, the RMSE of the estimated correlation coefficients and power spectra was less than 0.5% and 12%, respectively.

The rabbit liver study demonstrated that the 2DZM method performed well using real histology. An analysis of bias study was carried out to determine the smallest 2DZM that could be used without introducing bias. The RMSE for the correlation coefficients and power spectra when using 2DZMs with side length 150 μm was less than 1%, suggesting that 2DZMs with side length 150 μm were sufficient to estimate the correlation coefficient without bias. An analysis of variance study was carried out to determine the number of 2DZMs that were necessary to conduct 2DZM analysis. The RMSE for the correlation coefficient and power spectrum when using a single 2DZM with side length 300 μm was 3.7% and 1.7%, respectively. When using 10 2DZMs, the RMSE for correlation coefficient and power spectrum was less

than 1%.

2DZMs may be used to help identify anatomic scattering structures in tissues. For example, the spatial autocorrelation function estimated from a 2DZM could be modeled to estimate an ESD, which would represent a size associated with the impedance fluctuations in the ZM. Similarly, a form factor could be estimated from this correlation function and also modeled to estimate an ESD. Finally, the estimated form factor could be modeled over different frequency ranges to study the dominant scattering structure for each frequency range. When scanning tissues with ultrasound, the frequency range is limited by the bandwidth of the ultrasound system. ZMs might be used to identify the optimal frequency range that is most sensitive to a specific anatomic scattering structure.

6.2 Future work

Numerous directions of research are available for 2DZM analysis. For example, 2DZMs could be used to study whether tissues are isotropic. Determining if a tissue is not isotropic is important for QUS analysis because the parameter estimates would change depending on the incident ultrasound direction. In addition, knowledge of tissue anisotropy is important for studying QUS parameters using ZMs. If it is determined that a tissue is isotropic, 2DZM method #1 can be used to estimate the correlation coefficient and power spectrum. If it is determined that a tissue is transverse isotropic, the 2DZM method for transverse isotropic media could be used. If it is determined that a tissue is anisotropic, then it is necessary to complete the ZM analysis with knowledge of how the ZMs are aligned relative to the ultrasound wave propagation direction. However, it is important to note that when conducting ZM analysis for anisotropic media, having this knowledge of ultrasound wave propagation is necessary for both 3DZM analysis and 2DZM analysis.

2DZMs could be used to estimate tissue isotropy in the following manner. The correlation coefficient could be estimated for a 2DZM. The radial symmetry of this correlation could be assessed using different methods, either through direct comparison of radial lines from the correlation coefficient extracted at different angles or comparing scatterer size estimates based on radial lines from the correlation coefficient extracted at different angles. If

significant differences are observed as a function of angle, this would indicate that the tissue is anisotropic. Although this assessment of isotropy would be conducted in the plane in which the tissue was sliced, if the tissue is anisotropic, it is likely that this anisotropy would show up in a 2D analysis.

In addition, 2DZMs could be used to study the stationarity of acoustic tissue properties in a tissue, by analyzing 2DZMs created from different spatial locations. For example, the correlation coefficient could be estimated using 2DZMs from different spatial locations in the tissue. Similar correlation coefficients would be indicative of stationary tissue properties and dissimilar correlation coefficients would be indicative of non-stationary tissue properties.

A final area of development in ZM analysis is the assignment of impedance values. Currently, impedance values are assigned based on the color of the histology stain. A better method would be to directly measure tissue properties using a scanning acoustic microscope. 2DZMs created with a scanning acoustic microscope could offer significant improvements to the study of QUS methods using ZM analysis. This represents another advantage of 2DZMs over 3DZMs, which is the ability to extract parameters from a limited set of 2DZMs that might be provided by a scanning acoustic microscope technique.

REFERENCES

[1] S. Fields and F. Dunn, "Correlation of echographic visualizability of tissue with biological composition and physiological state," *The Journal of the Acoustical Society of America*, vol. 54, no. 3, pp. 809–812, 1973.

[2] E. J. Feleppa, F. L. Lizzi, D. J. Coleman, and M. M. Yaremko, "Diagnostic spectrum analysis in ophthalmology: A physical perspective," *Ultrasound Med. Biol.*, vol. 12, no. 8, pp. 623–631, 1986.

[3] E. Feleppa, A. Kalisz, J. Sokil-Melgar, F. Lizzi, T. Liu, A. Rosado, M. Shao, W. Fair, Y. Wang, M. Cookson et al., "Typing of prostate tissue by ultrasonic spectrum analysis," *IEEE Trans. Ultrason. Ferroelectr. Freq. Control*, vol. 43, no. 4, pp. 609–619, 1996.

[4] P. K. Tamirisa, M. R. Holland, J. G. Miller, and J. E. Pérez, "Ultrasonic tissue characterization: review of an approach to assess hypertrophic myocardium," *Echocardiography*, vol. 18, no. 7, pp. 593–597, 2001.

[5] M. F. Insana, "Modeling acoustic backscatter from kidney microstructure using an anisotropic correlation function," *J. Acoust. Soc. Am.*, vol. 97, no. 1, pp. 649–655, 1995.

[6] L. L. Fellingham and F. G. Sommer, "Ultrasonic characterization of tissue structure in the in vivo human liver and spleen," *IEEE Trans. Son. Ultrason.*, vol. 31, no. 4, pp. 418–428, 1984.

[7] M. L. Oelze, W. D. O'Brien Jr, J. P. Blue, and J. F. Zachary, "Differentiation and characterization of rat mammary fibroadenomas and 4t1 mouse carcinomas using quantitative ultrasound imaging," *IEEE Trans. Med. Imaging*, vol. 23, no. 6, pp. 764–771, 2004.

[8] J. Mamou, A. Coron, M. L. Oelze, E. Saegusa-Beecroft, M. Hata, P. Lee, J. Machi, E. Yanagihara, P. Laugier, and E. J. Feleppa, "Three-dimensional high-frequency backscatter and envelope quantification of cancerous human lymph nodes," *Ultrasound Med. Biol.*, vol. 37, no. 3, pp. 345–357, 2011.

[9] G. Czarnota, M. Kolios, J. Abraham, M. Portnoy, F. Ottensmeyer, J. Hunt, and M. Sherar, "Ultrasound imaging of apoptosis: high-resolution non-invasive monitoring of programmed cell death in vitro, in situ and in vivo," *Br. J. Cancer*, vol. 81, no. 3, p. 520, 1999.

[10] R. M. Vlad, S. Brand, A. Giles, M. C. Kolios, and G. J. Czarnota, "Quantitative ultrasound characterization of responses to radiotherapy in cancer mouse models," *Clinical Cancer Research*, vol. 15, no. 6, pp. 2067–2075, 2009.

[11] V. C. Anderson, "Sound scattering from a fluid sphere," *J. Acoust. Soc. Am.*, vol. 22, no. 4, pp. 426–431, 1950.

[12] M. F. Insana, R. F. Wagner, D. G. Brown, and T. J. Hall, "Describing small-scale structure in random media using pulse-echo ultrasound," *J. Acoust. Soc. Am.*, vol. 87, no. 1, pp. 179–92, January 1990.

[13] J. McNew, R. Lavarello, and W. D. O'Brien Jr, "Sound scattering from two concentric fluid spheres," *J. Acoust. Soc. Am.*, vol. 125, p. 1, 2009.

[14] S. I. Fields, "Ultrasound mammographic-histopathologic correlation," *Ultrason. Imaging*, vol. 2, no. 2, pp. 150–161, 1980.

[15] R. C. Waag, J. Nilsson, and J. Astheimer, "Characterization of volume scattering power spectra in isotropic media from power spectra of scattering by planes," *J. Acoust. Soc. Am.*, vol. 74, no. 5, pp. 1555–1571, November 1983.

[16] J. Mamou, M. L. Oelze, W. D. O'Brien Jr, and J. F. Zachary, "Identifying ultrasonic scattering sites from three-dimensional impedance maps," *J. Acoust. Soc. Am.*, vol. 117, no. 1, pp. 413–23, January 2005.

[17] J. Mamou, M. L. Oelze, W. D. O'Brien Jr, and J. F. Zachary, "Extended three-dimensional impedance map methods for identifying ultrasonic scattering sites," *J. Acoust. Soc. Am.*, vol. 123, no. 2, pp. 1195–1208, February 2008.

[18] A. J. Dapore, M. R. King, J. Harter, S. Sarwate, M. L. Oelze, J. A. Zagzebski, M. N. Do, T. J. Hall, and W. D. O'Brien, "Analysis of human fibroadenomas using three-dimensional impedance maps," *IEEE Trans. Med. Imaging*, vol. 30, no. 6, pp. 1206–13, June 2011.

[19] M. Gyöngy, L. Balogh, K. Szalai, and I. Kalló, "Histology-based simulations of ultrasound imaging: Methodology," *Ultrasound Med. Biol.*, vol. 39, no. 10, pp. 1925–1929, 2013.

[20] A. D. Pawlicki, A. J. Dapore, S. Sarwate, and W. D. O'Brien, "Three-dimensional impedance map analysis of rabbit liver," *Ultrasound Med. Biol.*, vol. 130, no. 5, pp. 334–338, 2011.

[21] F. T. Yu, É. Franceschini, B. Chayer, J. K. Armstrong, H. J. Meiselman, and G. Cloutier, "Ultrasonic parametric imaging of erythrocyte aggregation using the structure factor size estimator," *Biorheology*, vol. 46, no. 4, pp. 343–363, 2009.

[22] R. Lavarello and M. Oelze, "Quantitative ultrasound estimates from populations of scatterers with continuous size distributions," *IEEE Trans. Ultrason. Ferroelectr. Freq. Control*, vol. 58, no. 4, pp. 744–753, 2011.

[23] A. Han and W. D. O'Brien Jr, "Structure function for high-concentration biophantoms of polydisperse scatterer sizes," *IEEE Trans. Ultrason. Ferroelectr. Freq. Control*, vol. 62, no. 2, pp. 303–318, 2015.

[24] P. M. Morse and K. U. Ingard, *Theoretical Acoustics*. McGraw-Hill, 1968.

[25] M. Ueda and Y. Ozawa, "Spectral analysis of echoes for backscattering coefficient measurement," *J. Acoust. Soc. Am.*, vol. 77, no. 1, pp. 38–47, 1985.

[26] X. Chen, D. Phillips, K. Q. Schwarz, J. G. Mottley, and K. J. Parker, "The measurement of backscatter coefficient from a broadband pulse-echo system: a new formulation," *IEEE Trans. Ultrason. Ferroelectr. Freq. Control*, vol. 44, no. 2, pp. 515–525, 1997.

[27] R. J. Lavarello, G. Ghoshal, and M. L. Oelze, "On the estimation of backscatter coefficients using single-element focused transducers," *J. Acoust. Soc. Am.*, vol. 129, p. 2903, 2011.

[28] M. F. Insana and D. G. Brown, "Acoustic scattering theory applied to soft biological tissues," in *Ultrasonic Scattering in Biological Tissues*, K. K. Shung and G. A. Thieme, Eds. Boca Raton, Florida: CRC Press, 1992, pp. 75–124.

[29] S. F. Levinson, "Ultrasound propagation in anisotropic soft tissues: The application of linear elastic theory," *J. Biomech.*, vol. 20, no. 3, pp. 251–260, 1987.

[30] I. Fontaine, M. Bertrand, and G. Cloutier, "A system-based approach to modeling the ultrasound signal backscattered by red blood cells," *Biophysical Journal*, vol. 77, no. 5, pp. 2387–2399, 1999.

[31] E. Franceschini, T. François, F. Destrempes, and G. Cloutier, "Ultrasound characterization of red blood cell aggregation with intervening attenuating tissue-mimicking phantoms," *The Journal of the Acoustical Society of America*, vol. 127, no. 2, pp. 1104–1115, 2010.

[32] E. Franceschini, B. Metzger, and G. Cloutier, "Forward problem study of an effective medium model for ultrasound blood characterization," *Ultrasonics, Ferroelectrics, and Frequency Control, IEEE Transactions on*, vol. 58, no. 12, pp. 2668–2679, 2011.

[33] L. Tsang, J. A. Kong, K.-H. Ding, and C. O. Ao, *Scattering of Electromagnetic Waves: Numerical Simulations*. Wiley, 2001.

[34] J. M. Mamou, "Ultrasonic characterization of three animal mammary tumors from three-dimensional acoustic tissue models," Ph.D. dissertation, University of Illinois at Urbana-Champaign, 2005.

[35] A. J. Dapore, "Three-dimensional acoustic impedance map analysis of soft tissue," M.S. thesis, University of Illinois at Urbana-Champaign, 2010.

[36] A. D. Pawlicki, "Three-dimensional impedance map analysis of biological tissue to elucidate small-scale acoustic scattering behavior," M.S. thesis, University of Illinois at Urbana-Champaign, 2011.

[37] J. G. Proakis and D. G. Manolakis, *Digital Signal Processing*. Prentice Hall, 1996.

[38] A. M. Yaglom, *Correlation Theory of Stationary and Related Random Functions*. Springer, 1987.

[39] S. Torquato, *Random Heterogeneous Materials: Microstructure and Macroscopic Properties*. Springer, 2013.

[40] B. Widom, "Random sequential addition of hard spheres to a volume," *The Journal of Chemical Physics*, vol. 44, no. 10, pp. 3888–3894, 1966.

[41] G. James, D. Witten, T. Hastie, and R. Tibshirani, *An Introduction to Statistical Learning*. Springer, 2013.

[42] M. F. Insana and T. J. Hall, "Parametric ultrasound imaging from backscatter coefficient measurements: Image formation and interpretation," *Ultrasonic Imaging*, vol. 12, no. 4, pp. 245–267, 1990.

[43] D. G. Altman and J. M. Bland, "Measurement in medicine: the analysis of method comparison studies," *The statistician*, pp. 307–317, 1983.